The Pennsylvania State University

The Graduate School

TAILORING THERMAL EXPANSION IN ADDITIVELY MANUFACTURED TITANIUM ALLOYS TO ENABLE FUNCTIONAL GRADING

A Dissertation in

Materials Science and Engineering

by

Skyler R. Hilburn

Submitted in Partial Fulfillment
of the Requirements
for the Degree of

Doctor of Philosophy

December 2020

The dissertation of Skyler R. Hilburn was reviewed and approved by the following:

Todd A. Palmer
Professor of Materials Science and Engineering
Professor of Engineering Science and Mechanics
Dissertation Co-Chair
Co-Chair of Committee

Timothy W. Simpson
Paul Morrow Professor of Engineering Design and Manufacturing
Dissertation Co-Chair
Co-Chair of Committee

Allison M. Beese
Associate Professor of Materials Science and Engineering
Associate Professor of Mechanical Engineering

Edward W. Reutzel
Graduate Faculty Department of Engineering Science & Mechanics

John C. Mauro
Chair, Intercollege Graduate Degree Program in Materials Science and Engineering

ABSTRACT

Dissimilar material combinations are common in complex engineered systems. While these material combinations can contribute to improved performance, they can also lead to a range of interfacial failures, such as those caused by differences in their thermal expansion. Non-uniform stresses generated with changes in temperature can be large enough to lead to distortion and even failure. Given the ability of additive manufacturing (AM) to create novel materials, these interfaces can be replaced by a functionally graded material (FGM) designed to minimize the coefficient of thermal expansion (CTE) mismatch between dissimilar materials and produce more robust and higher performing engineered structure.

The design of FGMs using AM processes presents a unique set of challenges, primarily driven by the mixing and solidification of dissimilar materials which have different levels of compatibility. Typical failure mechanisms which must be addressed through design and AM processing include solidification cracking, chemical incompatibilities, such as immiscibility of alloying elements, and CTE mismatch. While most of the failure mechanisms have some mitigation strategies, the current techniques for mitigating the CTE mismatch are largely undeveloped. One potential route, however, can involve the controlled manipulation of CTE through changes in alloying element composition.

Since thermal expansion, particularly in hexagonally close packed systems, is anisotropic, wrought commercially pure (CP) titanium and AM CP titanium processed through laser based directed energy deposition were as investigated. While the processing route can alter grain orientation or provide a grain texture, the significant difference in observed CTE was correlated with sample orientation, with the vertically oriented samples displaying lower CTEs for both processing routes. The observed sample orientation CTE differences were determined to be a result of crystallographic texture.

Copper and silver were chosen as candidate alloying elements to increase the CTE of titanium beyond that of the wrought material. At 15 at.% copper alloy content, the CTE of commercially pure titanium was increased from 9.45 ppm/^{o}C to 10.5 ppm/^{o}C. The measured CTE values exceeded those predicted by an elemental rule of mixtures (ROM_E) procedure, which predicted a CTE of 11.9 ppm/^{o}C, which is 12% higher than the 10.6 ppm/^{o}C experimentally measured value. This discrepancy can be tied, in part, to the traditional rule of mixtures (ROM) approach applying to the phases present and not simply alloying element fraction. Additionally, the rapid solidification experienced in AM generated microstructures that were different than what was predicted by the equilibrium phase diagram, further complicating the prediction. Hot isostatic pressing (HIP) was used to reduce build porosity and to homogenize the microstructure, driving the phase fractions closer to equilibrium. HIP reduced the CTE of the 15 at.% copper alloy content from 10.5 ppm/^{o}C to 10.0 ppm/^{o}C.

The ability to tailor the CTE value depends on obtaining accurate values for each of the intermetallics or phases in the microstructure. Density Functional Theory (DFT) was utilized to estimate the unknown intermetallic phase CTEs. For the $CuTi_2$ intermetallic, DFT overpredicted the CTE by 7.5%. While this is a reasonable result, to design a final gradient using 0.5 ppm/^{o}C steps, experiments are required. Knowing the CTE of $CuTi_2$, a traditional phased-based ROM was utilized and accurately predicted the CTE within ~1% of the HIPed AM material. Using the phase-based ROM and the equilibrium phase fractions, a route to design functional materials that grade the CTE was demonstrated using a designed gradient from the experimentally measured value of 9.45 ppm/^{o}C of pure titanium to the DFT predicted CuTi intermetallic with a CTE of 11.6 ppm/^{o}C in 5 layers stepping in 0.5 ppm/^{o}C steps. A linear gradient in CTE requires a nonlinear change in composition based upon the intermetallic CTEs and the phase fractions.

TABLE OF CONTENTS

LIST OF FIGURES

LIST OF TABLES

ACKNOWLEDGEMENTS

This material is based upon work supported by the United States Air Force through the Air Force Institute of Technology Civilian Institute Program and the L3 Harris Corporation. Any views, opinions, results, findings, and/or conclusions expressed in this dissertation are those of the author and do not reflect the official policy or position of the United States Air Force, Department of Defense, the U.S. Government, or the L3 Harris Corporation.

This dissertation would not have been possible without the extra advice, help, and encouragement received during this experience. First, I would like to thank my advisors Dr. Todd Palmer and Dr. Tim Simpson for their invaluable guidance and mentorship. Additionally, my committee members, Dr. Allison Beese and Dr. Ted Reutzel, guided my research with excellent feedback and recommendations. Furthermore, I greatly appreciate the United States Air Force, U.S. Air Force Academy, Col. Tom Yoder, and Lt. Col. Don Rhymer for providing me this unique opportunity and for grooming me as an officer and professor. I would not be here without the guidance from Dr. Mike Lindsay who identified my potential early on and guided me toward the instructor role at the Academy.

During the course of my research at the Pennsylvania State University, I received help from many professors, staff members, and students. First, I would like to recognize the contributions Weinan Chen who ran the computational materials science simulations under the guidance of Dr. Ismaila Dabo. Additionally, as my research assistant, John O'Brien prepared and ran SEM characterization of countless samples. The Materials Characterization Lab Staff not only provided in-depth training, but also helped run characterization experiments and develop new equipment setups. Specifically, I would like to thank Julie Anderson, Nichole Wonderling, and Beth Last for all of their help and support. At CIMP-3D the staff of Dr. Jay Keist, Dr. Abdalla

Nassar, Dr. Ken Meinert, Peter Coutts, Cory Jamieson, Griffin Jones, and Ryan Overdorff all assisted with creating the additively manufactured samples and parts.

Dr. Palmer's Group and Dr. Simpson's group provided invaluable support and assistance during the course of my program. Andy Iams and Karan Doss devoted endless support as a colleagues and friends, always available to discuss ideas and help out. Dr. Selda Nayir developed my understanding of MTEX and contributed MATLAB code. Separately, I was able to develop a strong materials science and engineering foundation through the outstanding instruction of Dr. Susan Trolier-McKinstry, Dr. John Mauro, and Dr. Dabo. The crystal chemistry course taught by Dr. Trolier-Mckinstry fundamentally changed the entire way that I look at materials.

My ability to attend a civilian university would not have been available without the sponsorship offered by Dr. Simpson. Additionally, this research was only made possible through the funding from L3 Harris Corporation and the oversight of Eric Falk.

Finally, I would like to thank my family for their enduring support through the endless hours and the fast pace associated with my career. I am grateful to my amazing wife, who has encouraged and supported me through this challenging experience and to my son, for the fun and excitement that we have had together while still allowing me to get some work done. My parents and grandparents have always supported me, providing countless prayers and inspiring me to always do my best. I am grateful for God, who continues to bless me and guide my life.

Chapter 1

INTRODUCTION

The primary focus of this research is to solve a thermal expansion mismatch through the use of functionally graded materials (FGMs) by tailoring the CTE in a controlled manor through alloying element compositional changes. However, using AM compositional FGMs introduces another set of issues that must be avoided for material success. Currently, a method to mitigate CTE mismatch in AM FGMs has yet to be determined. Other possible AM FGM routes are presented as an alternate to AM compositional FGMs, but these alternatives have their own separate set of issues that compel pursuing the compositional route. This chapter serves to introduce the thermal stress issues created by a thermal expansion mismatch of materials and outline the research.

1.1 Role of Thermal Expansion in Generating Thermal Stresses

The expansion or contraction of a material with changes in temperature is quantified by the coefficient of thermal expansion (CTE). Many applications require an assembly of dissimilar materials which have different CTEs [1]–[6]. This assembly of dissimilar materials creates a CTE mismatch, generating stress at the interface due to temperature change, which can lead to part distortion or cracking [3], [7]–[9]. Some prevalent techniques employed to reduce the stress at the interface attempt to match CTEs between materials or accommodate the thermal stress generated through deformation of a filler material [3]. Adhesives can provide strong bonds between different materials, but they are limited through environmental degradation and catastrophic failure [6]. Brazing provides an avenue to join a variety of dissimilar materials together, but it has

limited strength due to soft fillers and can experience significant stresses on cooling depending on the CTEs of the materials used [3], [10], [11]. Figure 1.1 displays the consequences of not appropriately designing the interface for dissimilar metals with mismatched CTEs in a brazed joint.

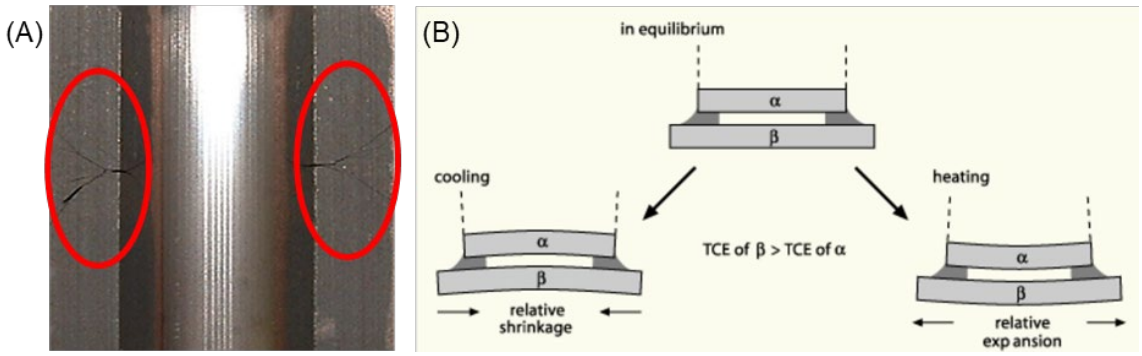

Figure 1.1. (A) Cracks are created from the brazing process due to a mismatch of thermal expansion coefficients [10]. (B) Distortion of α and β plates brazed together due to the CTE of β being higher than that of α [8].

Multi-material structural applications require interfacial integrity and the ability to withstand wide temperature service conditions. A primary example lies in the design of optical systems for space applications. These systems not only require dimensional stability and stiffness but also need to match CTEs to reduce the thermal strain that could create misalignment of the system [12]. Frame alloys are chosen for stiff and lightweight properties, but have relatively high CTEs. Common satellite structural materials are aluminum and titanium [13], [14], which differ in CTE by more than 15 ppm/K [15] and, if paired together in a frame and a bracket, require significant CTE mismatch mitigation. Additionally, these relatively high CTE materials are undesirable for holding relatively low CTE optics, as mitigation techniques are required to account for the thermal stress that can cause distortion of the optical system. An example of an optical bracket assembly for a satellite that is comprised of mismatched CTE materials is shown in Figure 1.2.

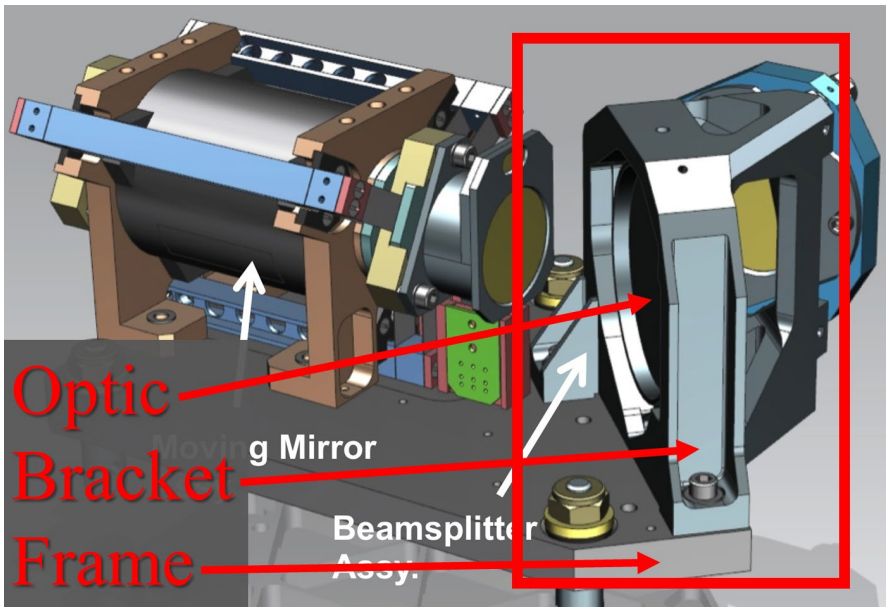

Figure 1.2. The red box highlights an example optical bracket assembly on a satellite. The optic is a different material from the bracket and the bracket is a different material from the frame, all with significantly different CTEs Image adapted from [16].

To reduce the CTE mismatch at the interface between the optic and the bracket, a different alloy is chosen for the optical bracket, and adhesives, flexures, or clamps are used to account for CTE mismatch between the optic and the bracket [17]. Accommodating thermal stress is also required [12] at the frame-bracket interface, as a potential 15 ppm/K [15] CTE mismatch can shift or distort the bracket, altering the optical system alignment even if the CTE mismatch was accounted for at the bracket-optic interface. Often adhesives or layered materials are used to accommodate the thermal stresses generated due to the CTE mismatch at the bracket-frame interface, but better performance is desired. Ideally, the best performance for this interface could be achieved through CTE matching the bracket with the frame, providing the lowest distortion in the optical system while maintaining the required structural rigidity.

1.2 Additive Manufacturing Functional Graded Materials

One potential route to achieve CTE matching among dissimilar materials is through the use of functional graded materials (FGMs). FGMs precisely tailor properties across a component to achieve the desired performance [18]. The layer-by-layer nature of additive manufacturing (AM) facilitates FGM production, allowing for the material to change with location during fabrication—a capability that is not available through conventional techniques [19]. However, the AM process can present new challenges in design and could create anisotropic material properties that would need to be factored into the final design.

Directed Energy Deposition (DED), shown in Figure 1.3, is currently the primary metal AM process used to generate compositional FGMs, where the composition of the powder feedstock is altered as a function of position during deposition [20]. Employing a compositional FGM has the potential to provide a graded CTE structure to match the component at the interface, enabling increased optical bracket performance by reducing distortion with temperature change.

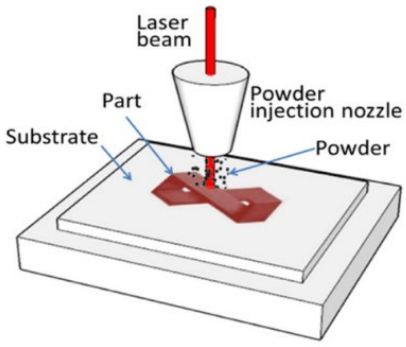

Figure 1.3. A schematic representation of the Directed Energy Deposition process [21].

The focus of current functional grading in AM attempts to combine two different alloy systems, each possessing distinct yet different desirable properties [18]–[20], [22]–[29].

Successfully deposited alloy systems include: Ti-6Al-4V to Pure V [22]; Ti to TiMo, TiV, and TiC [24], [30]; IN 36 to SS [23]; Fe to FeAl [31]; IN 625 to 316 SS [32], and 316L to Stellite 6 [33]. Multiple other attempted FGM systems experienced build failures including: Ti-6Al-4V to IN 718 [18], to INVAR 36 [19], and to γ-TiAl [34]; IN 625 to 304L SS [20]; and IN 82 to 316 SS [27]. Many of the compositional FGMs listed above can be attributed to using known metallurgically compatible systems.

1.3 Design Challenges for Functional Graded Materials

Three key issues that have been shown to lead to failure [18]–[20], [27], [34] are presented in Figure 1.4. The first issue is solidification cracking, which occurs as a result of large solidification ranges in the constituent material systems [27]. As the liquid metal solidifies, shrinkage can create cracks at grain boundaries and is often seen in the intergranular or interdendritic regions [35]. The second issue is chemical incompatibilities like immiscibility or intermetallics created when depositing the FGM [23]. Material immiscibility will prevent good mixing of the alloying element, and for miscible elements, the resulting intermetallics that form may be brittle and have a different CTE that the other phases [23]. Moreover, compositional partitioning can drive intermetallic formation. The third and final issue is high internal stresses generated from CTE mismatch during deposition, which can lead to the build cracking macroscopically or on a microscopic level. The CTE mismatch experienced in AM of FGMs is similar to the CTE mismatch issue for assemblies, but in this case, it occurs on a microscopic scale.

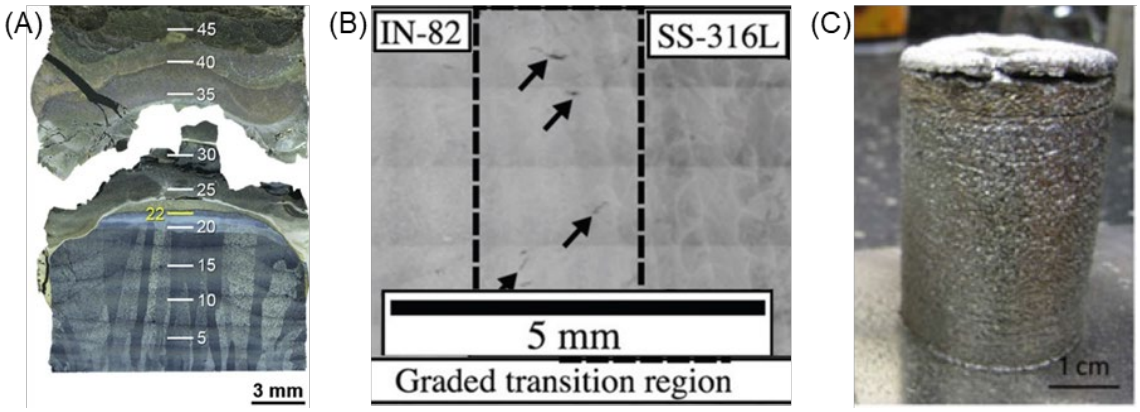

Figure 1.4. (A) The FGM wall transitioning from Ti-6Al-4V to Invar 36 cracked during machining due to a combination of CTE mismatch and intermetallic formation [19]. (B) Solidification cracking in the intergranular regions, highlighted with black arrows, occurred in this FGM due to a large solidification range [27]. (C) A failed FGM from titanium to 304 L due to intermetallic formation [23].

A few analysis tools used for material design are currently employed to address these three key issues in FGM design, but these approaches have significant limitations. The primary analysis tool is the use of computational thermodynamics to investigate multi-component phase diagrams, known as CALculation-of-PHase-Diagrams (CALPHAD). This tool is used to determine which equilibrium phases will exist and which compositional path should be taken in the phase diagram to avoid undesirable phases [19], [23], [36]. Problems arise with this approach due to the non-equilibrium nature of AM processes [27] and the lack of thermodynamic material data for new combinations of elements. The rapid solidification event can also create phase fractions significantly different than predicted by the phase diagram.

Another computational thermodynamics analysis tool investigates the changes in solidification and cooling rate effects which take into account the nonequilibrium conditions in order to investigate phases and segregation of the candidate material systems [27], [29], [37], [38]. Scheil equilibrium partitioning calculations assume no diffusion in the solid and infinite diffusion in the liquid and are thus used to predict compositional changes due to differences in the solidification range of elements in the alloy system [35]. This tool provides the expected

compositions during solidification, other techniques are still required to determine which phases might form [27], [29]. However, the greatest barrier with these CALPHAD approaches are the lack of kinetic and thermodynamic models on nonstandard alloy systems that may be investigated with the newfound capabilities to additively manufacture FGMs.

1.4 Alternative Functional Grading Approaches

Diffusion grading is an approach to generate a compositional gradient by depositing one material directly on top of another and letting the concentration difference drive diffusion during the re-melting of the previous layer [39]. This approach creates a compositional gradient over a short distance, but it is significantly limited by material systems that form undesirable phases such as the aluminum steel system [39], [40]. The AM process facilitates a gradient between two deposited compositions at their interface, making it difficult to achieve discrete compositions. Diffusion grading is susceptible to the same three identified issues experienced in compositional grading as it is essentially a compositional gradient over a short distance.

Finally, FGMs can also be generated with designed geometry instead of composition. The most prevalent example is the incorporation of geometric lattice-like structures to tailor the desired material property [4]. These structures would require coarse lattices built across small volumes or a switch in processing methods from DED to powder bed fusion (PBF) to achieve the required resolution. One example is the use of diamond-like structures to control the CTE of an optical mount (see Figure 1.5). In this example, the angle of the lattice diamonds and the materials can be altered to obtain a change from the original aluminum optical mount with a CTE of 24 ppm/K to an aluminum-titanium mount with a CTE of -1.5 ppm/K.

Figure 1.5. An optical mount designed with two materials to control the thermal expansion at the optic interface. The diamond lattice structure is tunable to achieve the desired CTE. Taken from [4].

Advantages to this approach are circumventing complications from varying the chemical composition, but it can lead to significant tradeoffs in other properties that are not considered during optimization. For thermal expansion, this method appears to be highly tunable, including the ability to generate a negative expansion upon heating [4]. This design strictly controls thermal expansion without considering material requirements like strength, stiffness, or geometrical constraints. Using geometry to create FGMs creates some distinct disadvantages as the design removes material volume, changing the impact of defects due to the AM process, reducing the strength and safety factor [41]. It could also create non-uniform deformation in the structure which is undesirable for the intended satellite application.

1.5 Research Objectives

Numerous applications utilize assemblies of materials with different thermal expansion coefficients, which can lead to distortion or even failure during a change in temperature. Current available solutions employ filler materials to reduce the CTE mismatch to mitigate the stress. Improved performance and reduced weight are sought in satellite systems and space applications

that experience significant temperature changes while requiring precise optical alignment. Additionally, to successfully deposit FGMs, intelligent novel material design is required to control the CTE. It is hypothesized that compositional changes can be used to tailor the CTE, enabling the design of an AM FGM that can mitigate thermal stresses due to CTE mismatch.

The overall goal of the work is to determine the impact of changes in composition, created with grading, on the resulting CTE. Elemental blending was employed to simplify the system, allowing a better understanding of what is occurring scientifically, while still achieving the desired thermal properties. Titanium was chosen as the system of interest due to its current use in satellite systems and its complexity—the hexagonal close packed crystal system has an inherently anisotropic thermal expansion coefficient. The research provides the foundation for innovative solutions to both the CTE mismatch issue in FGMs and for engineered assemblies involving multiple materials. The objectives for this dissertation are:

1. Characterize the thermal expansion coefficient of additively manufactured titanium. Perform direct thermal expansion measurements to compare the CTE behavior of wrought and additively manufactured titanium and quantify anisotropy.
2. Fabricate a binary titanium alloy to alter the CTE of titanium and investigate processing issues that lead to failure by building different alloy compositions to characterize the effect of alloy content on the CTE.
3. Determine the role of microstructure on the thermal expansion coefficient, specifically examining how intermetallics, crystal anisotropy and hot isostatic pressing alter the CTE.
4. Establish the significance of the inherent thermal expansion anisotropy in the hexagonal close packed crystal and determine its influence on the overall bulk CTE of alpha titanium.
5. Formulate and validate a method to predict the CTE for a given alloy system in order to tailor the CTE for FGMs and engineering applications.

The scope of the research encompasses characterizing the CTE, understanding the factors that influence it, and determining a method to predict CTE for novel FGMs. The research effort involves intelligent design and fabrication of multiple pre-blended elemental alloy compositions through laser-based DED. Bulk thermal expansion measurements were taken with push-rod dilatometry and lattice thermal expansion was measured through x-ray diffraction. Key aspects of the microstructure and crystal orientation were identified through the use of scanning electron microscopy (SEM) in conjunction with energy dispersive x-ray (XRD) spectroscopy and electron backscattered diffraction (EBSD). Particle-reinforced composites models in conjunction with computational materials science calculations were developed to predict thermal expansion coefficients. The new knowledge gained from these scientific efforts contributes unique insights into the body of knowledge needed to design tailored CTEs for FGMs and engineered multi-material applications.

1.6 Overview of Dissertation

The dissertation commenced in Chapter 1 with an introduction to thermal stress and the effect on engineered systems, prompting the research focus of tailoring the CTE for multi-material systems. Motivation for the research is drawn from both real-world satellite engineering challenges and current problems with FGM design. The hypothesis that compositional changes can be used to tailor the CTE to generate a buildable FGM is presented. Finally, a list of research objectives along with the method needed to achieve the objectives is given.

In order to properly understand the research challenge presented in the first chapter, Chapter 2 reviews the fundamental science behind thermal expansion as well as related research. The origins of thermal expansion are discussed along with how CTE can be measured. Specific focus is given to metals, and the current gaps in the ability to predict CTE are presented.

With the fundamental science well understood, direct thermal expansion measurements are explained in Chapter 3. Relevant ASTM standards are presented to understand the specifics of this analysis technique. An investigation into the thermal expansion behavior of AM grade 1 titanium is performed and compared with wrought titanium values. The thermal expansion impact of hot isostatic pressing both AM and wrought titanium are discussed.

Given the findings in Chapter 3, Chapter 4 presents a method for the selection of candidate elemental alloys in the design of an FGM. Titanium is chosen as an example base metal and both copper and silver are chosen as candidate alloying elements. Thermal expansion performance of the candidate titanium alloys is presented along with the effect of hot isostatic pressing them.

Impact of key microstructural features, with a focus on intermetallic phases and crystal orientation, is explored in Chapter 5. Experimental results are presented on the thermal expansion of the $CuTi_2$ intermetallic and its effect on the overall CTE of the system. The significance of the CTE tensor is explored in detail, studying the anisotropic hexagonal titanium crystal to determine the impact of crystallographic texture on CTE. The microstructural CTE is linked to the bulk CTE through a combination of the EBSD and XRD data.

Utilizing the knowledge gained from Chapters 2-5, Chapter 6 provides a method to predict the CTE for an alloy system. Density Functional Theory (DFT) is used to determine unknown intermetallic compound CTEs. These computational CTEs are then used with models from particle-reinforced composites research to create a functional graded material, where the CTE gradient is created from compositional changes.

Finally, in Chapter 7, a summary of the key results from this research is presented. The conclusions in this dissertation are drawn from fundamental materials science and engineering. Contributions to the field are discussed along with limitations of the work and areas of future research.

Chapter 2

LITERATURE REVIEW

The thermal expansion coefficient (CTE) is an intrinsic material property that can be described at the microscopic and macroscopic scales. From a design and engineering perspective, the macroscopic or bulk CTE is often used during design of complex systems for aerospace components. Macroscopic thermal expansion behavior in polycrystalline materials is a direct result of what is occurring microscopically, within a single grain, averaged across the whole material. Consequently, the fundamentals of thermal expansion on the single grain scale may hold key insights into the thermal expansion behavior at the bulk scale.

From a historical perspective, the concept that fire caused other elements to change dimensions has been around since the first century B.C.; however, more attention was focused on thermal expansion with the invention of a thermometer in the late 1500s to early 1600s [42]. It was not until the discovery of Invar, Einstein's harmonic oscillators, and Grüneisen's Rule that thermal expansion was given serious scientific thought in the early 1900s [42]–[44]. Once the theories were well established, most of the current body of thermal expansion knowledge was generated between 1950 and 1980, and it has significantly slowed down afterwards [42], [43].

Thus far, investigations into the CTE behavior of AM materials have been focused on trying to compositionally grade between traditional alloys with known CTEs or tuning cellular structures to get a desired CTE as seen in Figure 1.5 [4], [22]. Consequently, in order to tailor CTEs compositionally, the fundamentals of thermal expansion are explored in this chapter. First the microscopic and macroscopic understanding of CTE is presented for pure materials. Since alloy systems have a higher degree of complexity than pure materials, the change in CTE due to

dilute alloying is investigated. With thermal expansion fundamentals understood, both microscopic and macroscopic measurement techniques are discussed. Finally, an investigation into how CTE is estimated in multicomponent systems is presented along with how thermal expansion mismatch is handled in systems where it is prevalent.

2.1 Microscopic Thermal Expansion Fundamentals

Microscopically, crystalline solids are comprised of periodically ordered networks of atoms arranged in a lattice or repeating structure [45]. The atoms within are not stationary; rather, they are constantly vibrating or oscillating around an average position [45], [46]. The system of atoms can be modeled through a Boltzmann energy distribution and was initially developed around Einstein's theory of vibratory harmonic oscillators, employing Plank's energy quantization [45], [47], [48]. While the harmonic term of the energy function can be used to estimate many crystalline properties, it does not predict thermal expansion [45]. If only harmonic oscillations are allowed, then the amplitude of the vibrations would increase with temperature while the average position of the atoms would remain the same [43], [45]. In the simplest case, the anharmonicity of the energy well between two atoms provides a rudimentary mechanism for describing thermal expansion as seen in Figure 2.1 [42], [45], [48], [49].

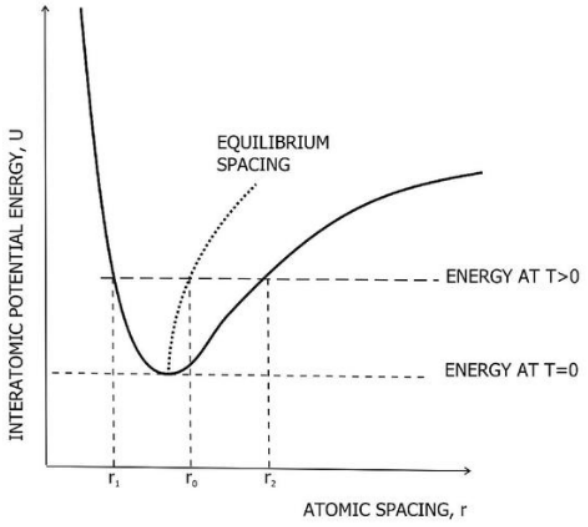

[49]

Figure 2.1. The asymmetric potential energy well for the interatomic separation of two atoms which rudimentarily describes the fundamental mechanism of thermal expansion [49].

This asymmetric potential energy well model can be expanded to a simple one dimensional model for vibratory motion using a ball and spring representation of atoms in the lattice as shown in Figure 2.2. However, atoms in the lattice not only move in line with the springs, but also perpendicular to the springs in a wave like three dimensional motion [42], [50]. The energy of these lattice vibrations can be quantized as phonons, which are one of the primary mechanisms of thermal transport [45], [48]. The bond characteristics of the atoms in the lattice have an effect on the atomic spacing and therefore the thermal expansion behavior [45].

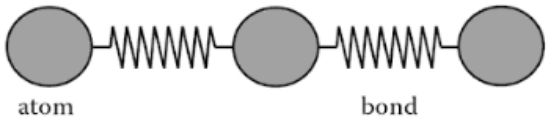

Figure 2.2. The ball and spring model of atoms and bonds, respectively, describing the nature of atoms in a lattice [50].

Microscopically, thermal expansion theories are often represented using thermodynamic quantities [42], [43]. Mie [42], initially predicted that the ratio of the volumetric CTE to the isothermal compressibility was constant. Grüneisen noticed that the ratio of the volumetric CTE over the heat capacity was constant for many metals, which led to his rule [42], [43], given by Equation 2.1 [43]:

$$\frac{3\alpha}{\chi_T} = \gamma \frac{C_V}{V} \tag{2.1}$$

where α is the linear CTE, χ_T is the isothermal compressibility, C_V is the specific heat, V is the volume, and γ is the Grüneisen constant [43]. His parameter remains constant with temperature change across many crystalline solids and takes into account the anharmonicity of the potential energy well for a pair of atoms [42]. Grüneisen's rule does not describe phase transitions or anisotropic materials, but it serves as a basis for many subsequent theories [42].

More thermodynamic details and equations for microscopic thermal expansion are available in references [5] and [6], including the contributions to the CTE due to electronic or magnetic effects. It is important to note that any change to the crystal lattice can create significant changes to the thermal expansion coefficient. For example, a discontinuity exists in the CTE as the temperature approaches a phase change where the crystal lattice rearranges crystal structure or at a ferromagnetic transition when the attraction or repulsion of atoms changes, thus changing the equilibrium positions of the atoms [42].

Estimates of the CTE can be determined from the microscopic understanding of thermal expansion. The melting point of a solid on a microscopic scale occurs when the thermal vibrations are severe enough to break the bonds in the lattice [45]. The volumetric expansion of the crystal lattice from 0 K to the melting point for many metals is approximately 8% [45]. Therefore, as a general rule of thumb, the higher the melting point, the smaller the expansion is over each temperature segment, lowering the thermal expansion [45]. Stronger bonds shorten the bond length and make the potential energy well deeper and more symmetric, lowering a

material's CTE [45]. Similarly, an increase in bond valence causes a decrease in the thermal expansion coefficient [45].

While these generalizations work well for pure metals, most engineered systems use structural materials that are alloys that create more complexities. One of the most notable examples is Invar, the 36 wt.% nickel 64 wt.% iron alloy [44], [45]. At temperatures below the Curie point, Invar is ferromagnetic, and it experiences a volumetric magnetostriction that limits the thermal expansion due to the magnetic field [44]. Separately, at temperatures below the Debye temperature, not all of the vibrational phonon modes are active, causing the expansion behavior of Invar to become nonlinear at cold temperatures [49].

2.2 Macroscopic Thermal Expansion Fundamentals for Pure Materials

Thermal expansion is most commonly evaluated and reported through the macroscopic coefficient of linear thermal expansion, α_{ij}, which is a second-rank symmetric tensor property [43], [45]. This coefficient relates the strain, change in length per original length, to a change in temperature, as given in Equation 2.2 [45].

$$\varepsilon_{ij} = \alpha_{ij}\Delta T \tag{2.2}$$

The strain is represented by ε_{ij} which is created by the linear coefficient of thermal expansion, α_{ij} due to a change in temperature, ΔT. As the linear coefficient of thermal expansion is a second-rank tensor property, it can behave anisotropically, resulting in different expansions along different directions with a maximum of 6 independent directions based on the minimum symmetry [43], [45]. Each crystal system describes the characteristic symmetry of atoms in the material describing the spatial relationship of inherent material properties. The number of

independent thermal expansion constants needed to describe the CTE for each crystal system is summarized in Table 2.1.

Table 2.1. Bravais lattice crystal systems and the corresponding coefficient of thermal expansion tensor. Taken from *[43]*.

Crystal System	Axial relations	No. of constants	Thermal expansion tensor referred to axes in the conventional orientation
1. Triclinic	$a \neq b \neq c$ $\alpha \neq \beta \neq \gamma$	6	$\begin{bmatrix} \alpha_{11} & \alpha_{21} & \alpha_{31} \\ \alpha_{21} & \alpha_{22} & \alpha_{32} \\ \alpha_{31} & \alpha_{32} & \alpha_{33} \end{bmatrix}$
2. Monoclinic	$a \neq b \neq c$ $\alpha = \beta = 90°$ $\gamma \neq 90°$	4	$\begin{bmatrix} \alpha_{11} & 0 & \alpha_{31} \\ 0 & \alpha_{22} & 0 \\ \alpha_{31} & 0 & \alpha_{33} \end{bmatrix}$
3. Orthorhombic	$a \neq b \neq c$ $\alpha = \beta = \gamma = 90°$	3	$\begin{bmatrix} \alpha_{11} = \alpha_1 & 0 & 0 \\ 0 & \alpha_{22} = \alpha_2 & 0 \\ 0 & 0 & \alpha_{33} = \alpha_3 \end{bmatrix}$
4. Tetragonal	$a = b \neq c$ $\alpha = \beta = \gamma = 90°$	2	$\begin{bmatrix} \alpha_{11} = \alpha_1 & 0 & 0 \\ 0 & \alpha_{22} = \alpha_1 & 0 \\ 0 & 0 & \alpha_{33} = \alpha_3 \end{bmatrix}$
5a. Hexagonal (*Trigonal*)	$a = b = c$ $\alpha = \beta = \gamma \neq 90°, < 120°$		
5b. Hexagonal	$a = b \neq c$ $\alpha = \beta = 90°,$ $\gamma = 120°$		
6. Cubic and Isotropic	$a = b = c$ $\alpha = \beta = \gamma = 90°$	1	$\begin{bmatrix} \alpha_{11} = \alpha & 0 & 0 \\ 0 & \alpha_{22} = \alpha & 0 \\ 0 & 0 & \alpha_{33} = \alpha \end{bmatrix}$

Another method for reporting a material's thermal expansion is through the volumetric thermal expansion coefficient, β, which is taken relative to a reference volume as given in Equation 2.3 [42], [45]:

$$\beta = \frac{1}{V}\left(\frac{\delta V}{\delta T}\right)_P \tag{2.3}$$

where V represents the volume and T the temperature, taken at constant pressure, P. The volumetric thermal expansion for isotropic materials is simply three times the linear CTE and is the sum of the principle axes of the linear CTE for anisotropic materials [42], [45]. Even though the CTE is clearly a tensor property, it is often reduced to a scalar quantity, ignoring the anisotropy, for most materials [45]. This is evident through textbooks and handbooks which list the nominal CTE values for different materials as scalars. This simplification may not be true in AM materials and needs to be investigated.

2.3 Thermal Expansion Fundamentals for Dilute Binary Alloys

Thus far, all of the information provided applies to pure or ordered materials. With the primary focus of this work being on metals, which contain a complex combination of different pure elements, the effect of alloy content on the CTE needs to be understood. Generally, alloying with higher CTE metals will increase the thermal expansion, while alloying with lower CTE metals will decrease it [42], [45]. This trend is evident in the alloying of aluminum as seen in Figure 2.3. Note that magnesium was the only element with a higher CTE than aluminum, subsequently raising the CTE with increased alloy content [42]. Additionally, titanium has the lowest CTE of the alloying elements presented in this figure and drastically reduced the CTE with only a small alloy content [42].

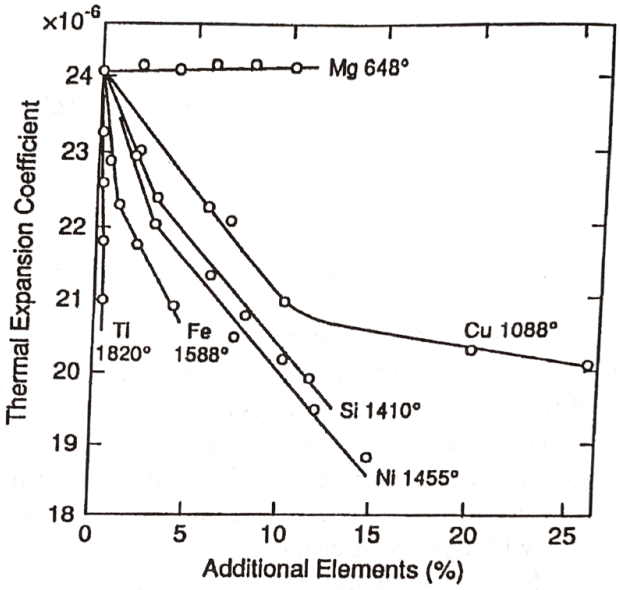

Figure 2.3. The resulting thermal expansion coefficient due to additions of alloying elements to aluminum. Magenesium is the only element having a higher thermal expansion than aluminum. Taken from [42].

Transition metals may not always follow this trend, as nickel and manganese lower the CTE of iron, even though they have higher thermal expansions [42]. For these elements, a magnetostriction effect drives the thermal expansion behavior below the Curie point and is the principle used for the low CTE iron-nickel alloy, Invar [44], [51]. Another example is shown for titanium, where the addition of chromium increases the CTE of titanium even though chromium has a lower expansion coefficient, as seen in Figure 2.4 [42]. This anomaly is theorized to occur due to the formation of $TiCr_2$, an intermetallic phase due to the alloy content; current thinking asserts that the $TiCr_2$ intermetallic is raising the CTE, but no further investigation has been performed [42].

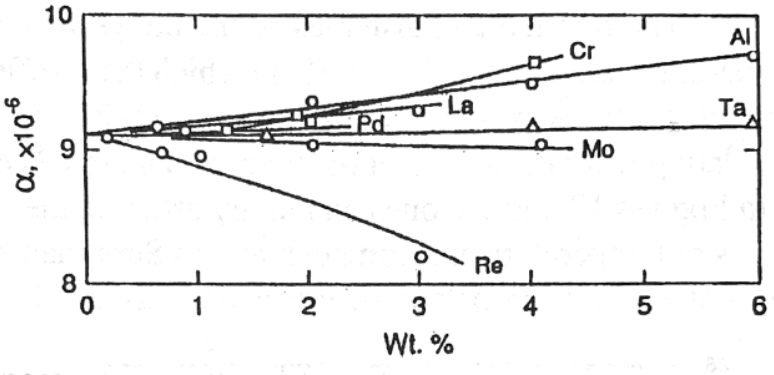

Figure 2.4. Titanium's CTE is plotted from 0-400 oC with different alloying elements. All of these alloying elements follow the guidelines with the exception of chromium, which raises the CTE of titanium when it expected to lower it. Taken from [42].

For alloys created with low solute content such that a single phase solid solution is maintained, the CTE can be estimated empirically, given experimentally found lattice constants and the solid solubility [42]. As many alloys are dilute solid solutions, this may be a reasonable approach as the general rule of thumb is to stay within the solid solubility region. However, the fundamental understanding of thermal expansion of alloys is underdeveloped, making the thermal performance of functional alloys with high solute content as can now be made with AM hard to predict.

2.4 Microscopic Thermal Expansion Measurement Techniques

Two categories exist for the measurement techniques as determining the CTE: (1) microscopic and (2) macroscopic [43]. Microscopic measurement has less accuracy than macroscopic measurement, but it provides additional insight into what is occurring in the crystal structure [42]. X-ray diffraction (XRD) is the technique used to determine microscopic CTEs [42], [43]. The radiation produced in XRD experiments is on the order of an angstrom, providing

the ability to probe the crystal lattice [52]. Diffraction patterns are created from constructive interference from parallel planes of atoms, while all other scattered rays become eliminated through destructive interference [52]. Figure 2.5 shows x-rays that would have constructive scattering and provide a signal, while all other ray directions for this example would be eliminated [52]. The ability to determine the spacing between these planes is given by Bragg's Law, which is defined by Equation 2.4 [42], [43], [45], [52].

$$n\lambda = 2d \sin\theta \tag{2.4}$$

where n is 1 since only first-order reflections are used, λ is the wavelength of the x-ray, d is the spacing between planes, and θ is the diffracting angle from the plane of atoms [52]. Since the only unknown is the lattice spacing, it can be calculated from the diffraction pattern.

In order to calculate thermal expansion, a heat source that can work with the equipment is required [42]. Two measurements are then taken across the range of temperatures of interest and lattice planes, allowing the lattice parameters to be calculated [42]. Using Equation 2.2, a strain can be calculated using the lattice parameters from each data set and with the change in temperature, and a lattice CTE can be extracted [42].

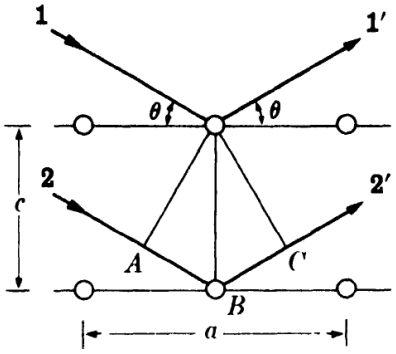

Figure 2.5. A demonstration of Bragg's Law. The incident x-rays enter the crystal lattice and scatter off of atoms. Parallel planes of atoms provide constructive interference, increasing the amplitude of the wave and register a signal, while all other scattering events are destructive. Image from [53].

The real benefit of performing a microscopic CTE experiment is being able to determine the CTE for each phase in the material as well as identify any anisotropy in the measurement [42], [43]. This anisotropy is typically not seen in bulk measurements, unless multiple samples in different orientations are sampled. Even then, if the material underlying crystal structure is completely random, then the anisotropy would average out across all the grains. For the microscopic CTE of a unit cell, thermal expansion coefficients can be calculated for a, b, and c sides for each phase in the material. Other advantages include no thermal errors in the supporting equipment, only a small quantity of sample is needed to acquire the measurement, and internal strains could be investigated using different XRD techniques [42], [43]. The key disadvantage of microscopic measurement is the lack of accuracy since the calculation of strain involves lattice parameters that are almost the same with a larger thermal expansion providing a more accurate measurement than a small thermal expansion [42]. Some other disadvantages that were not readily discussed in the literature include difficulties in isolating individual phase peaks in a multiphase material or isolating the scan peaks from any additional peaks that are generated from the x-rays interacting with the sample holder.

2.4 Macroscopic Thermal Expansion Measurement Techniques

Many methods exist for determining the macroscopic CTE of a material as there are numerous ways to measure temperature and length [43]. All measurements depend on the ability to accurately measure these values and eliminate the sources of error [42], [43]. Instrumentation designed to study the effects of temperature on the dimensions of a sample is called a dilatometer [54]. For a standard evaluation of the CTE, the two predominant techniques are pushrod dilatometry and interferometry as shown in Figure 2.6 [42], [43].

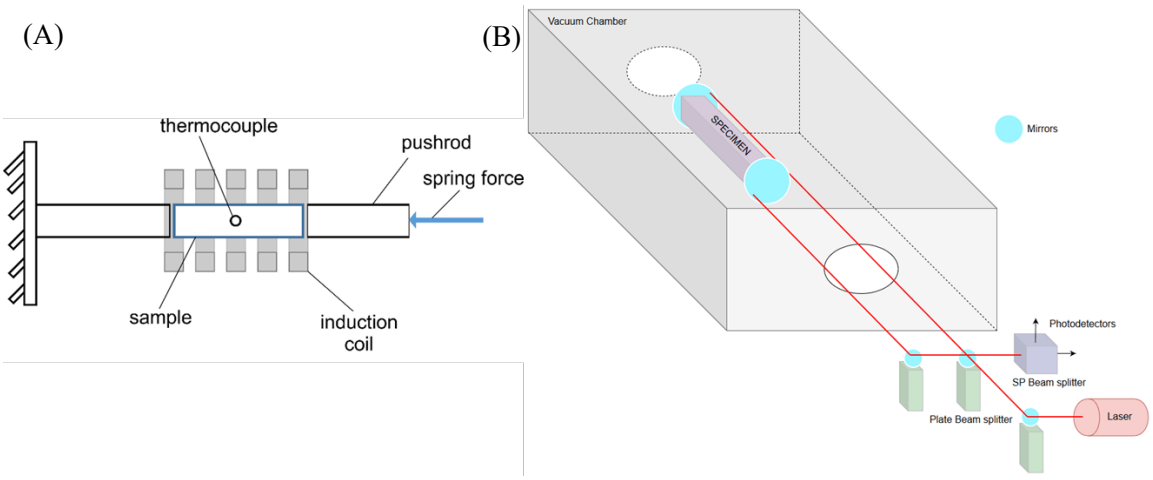

Figure 2.6. (A) A schematic for a typical push rod dilatometer, taken from [55]. (B) A Michelson interferometer schematic is shown as an example of one type of interferometry dilatometers, taken from [56].

In pushrod dilatometry, a sample is pinched between two rods, heat is applied, and as the sample expands, the displacement is recorded using a transducer [42]. This technique is straightforward, but it requires calibration as the push-rods expand with temperature as well as the sample. When performing interferometric techniques, a light or laser is used with optics to generate interference fringes [42], [57]. These fringes can then be used to calculate the change in length of the sample by relating the order of interference with the specimen length using Equation 2.5 [43]:

$$\Delta L = \frac{\lambda}{2}\Delta N \tag{2.5}$$

where the order of interference is N, the wavelength of light is λ, and L is the change in length [43].

These techniques along with others are described in great detail in [42], [43]. The key differences in the techniques lies in the size of the sample needed and the accuracy of the measurement. The push rod dilatometers require larger samples, and error is introduced due to nonhomogeneous temperatures and the expansion of the rods [43]. The system is calibrated with a reference standard to reduce the sources of error [42]. Interferometric techniques have a higher

degree of accuracy as the measurements are absolute and can be taken without contacting the sample, while the uncertainty resides in the actual wavelength output of the source [58]. These methods will work with any sample that meets the size and shape requirements for the designed system.

The measurement techniques for thermal expansion are well known and have been thoroughly developed [42], [43]. From a metal perspective, typically thermal expansion has been studied for monolithic pure elements and common wrought or cast engineering alloys. Microscopic XRD inspection of multiphase materials can provide the thermal expansion of each phase, but the bulk macroscopic techniques can only provide the net expansion of all the phases and orientations. Additionally, anisotropy in metals has been largely discounted due to the assumption of a randomly oriented polycrystalline nature of these materials. If they are truly random in crystal orientation, then the net linear thermal expansion averages out any anisotropy in the system. This is an oversimplification as not all structural metals are cubic, like titanium, and due to material processing, the structure is complex with some crystallographic texture present. With the recent ability to generate new functional materials through additive manufacturing, the question remains as to whether the simplifications and underlying assumptions will hold true for these more complex materials, which consist of multiple phases with some crystallographic texture. Titanium has been shown to be a difficult alloy system with basal plane crystal orientations that provide 50% higher hardness values than that of prism orientations [59]. The next section discusses how the CTE is estimated for other complex multicomponent materials.

2.5 Thermal Expansion Estimation in Multicomponent Material Design

Determining the CTE for solids comprised of multiple materials is not a new problem. The composites, ceramics, and coatings communities have attempted to predict the thermal expansion of multicomponent materials. Thermal expansion has been studied for ceramics, particle- and fiber-reinforced composites, as well as metal and ceramic matrix composites, and hybrid materials [60]–[70]. Five main theories are discussed: (1) Rule of Mixtures (ROM) [60]–[66], (2) Turner [67], [71], (3) Kerner [60], [61], [65], [66], [72], (4) Thomas [73], [74], and (5) Hashin-Shtrikman [75], [76].

Of these five models, the CTE has been shown to generally be governed by ROM and can be generalized by Equation 2.6 [60]–[66] (adapted from [66]):

$$\alpha_{bulk} = \alpha_1 V_1 + \alpha_2 V_2 + \cdots \tag{2.6}$$

where α is the CTE and V is the volume fraction, with the subscripts indicating each of the phases in the multicomponent material. In this case, two phases or materials are given, but it could be adapted for as many as required. It is important to note that the ROM typically describes particles suspended in a matrix where it assumes a combination of independent phases that do not alter the behavior of each other [62]. For the traditional ROM, Voigt assumed uniform strain and developed a formula based on the CTE, volume, and elastic modulus of each constituent. This has been further reduced to the Voigt approximation, where the elastic moduli are dropped and reverts to the generalized case in Equation 2.6 [71]. The ROM is considered to define the CTE upper bound [65], [71].

Turner developed a model by replacing the elastic modulus of Voigt's original formula with the bulk modulus, K [71]. Equation 2.7 shows Tuner's formula [67], and it is considered to be the CTE lower bound [71].

$$\alpha_c = \frac{\alpha_m V_m K_m + \alpha_p V_p K_p}{V_m K_m + V_p K_p} \quad (2.7)$$

In Equation 2.7, α is the CTE; V is the volume fraction; and K is the bulk; p and m are indexes of particles and matrix respectively [67]. While considered the lower bound, the Turner model is usually significantly lower than actual CTE measurements.

In the metal-ceramic, metal matrix composite, and ceramic-ceramic systems, the consensus is that ROM provides a close approximation while Kerner's equation (see Equation 2.8) can provide a more accurate approximation when bulk moduli are substantially different for the material phases [60], [61], [65], [66], [72]. Many of these are also comprised of particles in a matrix which could behave differently than metals. Kerner's equation is given by:

$$\alpha_c = \left[\alpha_m V_m + \alpha_p V_p\right] + \left[\frac{V_p V_m (\alpha_p - \alpha_m)(K_p - K_m)}{V_m K_m + V_p K_p + \left(\frac{3 K_p K_m}{4 G_m}\right)}\right] \quad (2.8)$$

where α is the CTE, V is the volume fraction, K is the bulk modulus, and G is the shear modulus, p and m are indexes of particles and matrix respectively [66]. Kerner's model considers both bulk and shear moduli and is considered one of the more accurate models in use today. In practice, the Kerner prediction is not significantly different than the ROM when the bulk moduli have the same order of magnitude [60].

When considering dual phase stainless steel welds, the Thomas model was found to be the most accurate by Elmer [73]. The Thomas model was created semi-empirically based on results from particle-reinforced composites and is seen in Equation 2.9, modified from [74]:

$$\ln(\alpha_s) = V_p \ln(\alpha_p) + V_f \ln(\alpha_f) \quad (2.9)$$

where α is the linear CTE and V is the volume fraction, with the subscript s for the system, p for the polymer and f is for the filler [74]. This equation is basically a logarithmic form of ROM and was developed based on data obtained from particle-reinforced composite measurements.

Finally, the Hashin-Shritkman model developed bounds for magnetic permeability of two-phase materials and was adapted to thermal conductivity and CTE [75], [76]. The upper bound is given by Equation 2.10, modified from [75]:

$$\alpha_u = \alpha_2 - \frac{K_1 V_1 (\alpha_2 - \alpha_1)(3K_2 + 4G_2)}{K_2(3K_1 + 4G_2) + 4G_2 V_1 (K_1 - K_2)} \tag{2.10}$$

where α_u is the upper CTE bound, K is the bulk modulus, G is the shear modulus, and V is the volume fraction. The Subscripts 1 and 2 represent the property of phase one (or material one) and phase two (or material two), respectively. To calculate the lower bound, the subscripts are swapped, changing all the twos to ones and vice versa [75]. Overall, these five models reasonably provide a range of predictions for multicomponent material systems.

While the ROM model provides a good estimation and reasonable starting point, the other models have been developed in an effort to better describe the CTE of multicomponent systems. Miyamoto et al. [65] has shown that the ROM and Kerner models reasonably predict CTE across a wide range of material systems including metallic/ceramic, and ceramic systems, seen in Figure 2.7. The advantage of the Kerner model is that an attempt has been made to account for the other differences of the phases beyond just their CTEs at a specific temperature range. The disadvantage is that additional material properties like bulk and shear moduli are required to compute it. While these properties may be easy to obtain for composite structures with a well-characterized matrix and reinforcements, when looking at combining metallic elements, the phases created may not have data available.

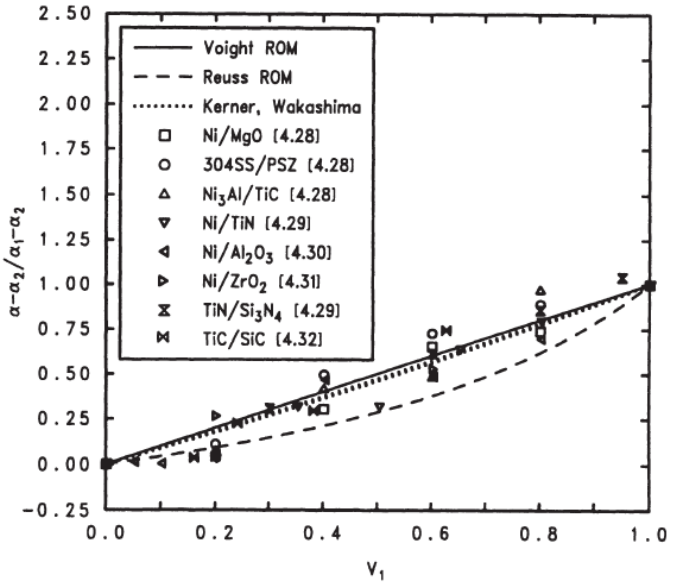

Figure 2.7. The CTE prediction models are shown against many metal-ceramic and ceramic-ceramic materials. Taken from [65].

Clearly these models work well with composite and even metallic hybrid systems, but an overall lack of understanding in alloys exist. Metal alloys are different than composites as the properties of the phase created may not be close to the pure elemental phase of each constituent. The Thomas model, which has been shown to work for stainless steel welds that are comprised of both austenitic and ferritic phases, starts to address the difficulty of these systems, although the semi-empirical method may not prove to work for functionally graded materials—and would need to be experimentally recomputed for each new FGM. Other models, like the bounds in the Hashin-Shtrikman model, have been developed to try and address binary alloys and eutectic systems, but they suffer from the same limitations as the Kerner model where other material properties are required [75]. Now that the predominate CTE estimation methods in multicomponent materials have been explored, investigation into the mitigation techniques for systems that address high CTE mismatch could provide additional insight into FGM alloy design.

2.6 Thermal Expansion Mismatch

In order to better understand the challenges associated with attempting to tailor CTE, literature was reviewed in systems where a CTE mismatch exists. The composites field utilizes the prediction methods discussed in Section 2.5 to address the CTE mismatch. In brazing applications, CTE matching is the preferred technique, and when it cannot be accomplished, the filler metals are designed to be ductile enough to accommodate the internal stress without failure [3], [10], [11]. Thermal barrier coatings and FGMs offer insights into other mitigation techniques. In coatings, a large CTE mismatch between the base material and the coating often exists, which can cause delamination [77]. In thermal barrier systems that can experience a change in temperature above 1,000ºC, a difference in CTE difference of only 1 ppm/ ºC can cause internal stresses in the hundreds of megapascals at elevated temperatures [78]. When possible, a multi-component phase diagram approach is taken [78], but with complicated multielement systems, the data is often not available or readily understandable. Prediction of phase structure in interdiffusion has also been studied, but is restricted by lack of interdiffusion data [78]. Monte Carlo simulations are then required to be able to determine the needed diffusion coefficients and in the end experimental approaches are used to determine the final coating, attempting to match CTEs closely [78]. When the CTEs cannot be matched, a graded interlayer can be employed to mitigate the internal stresses [61].

FGMs often use materials where a CTE mismatch occurs. One of the most prevalent techniques used today is compositional grading, in an attempt to move from Composition A to Composition B during component fabrication [19], [23], [30], [39]. When designing these FGMs, the main approach currently used is the CALculation of PHAse Diagrams (CALPHAD) method [19], [22], [23], [27], [36]. While this method attempts to address the possibility of forming undesirable phases within the metallic compositional gradient, it does not address issues due to

thermal expansion. Hofmann et al. [22] successfully deposited a FGM of 304 L stainless steel to INVAR 36 by compositionally increasing the nickel while decreasing the chromium, achieving a significant difference of roughly 16 ppm/K in the CTE from one side to the other. By analyzing the individual compositions in the gradient, it was reported that the CTE was a ROM average across the stepwise compositional gradient as shown in Figure 2.8 [22]; however, this gradient was designed to be compositional in nature and not a true gradient of the thermal expansion coefficient.

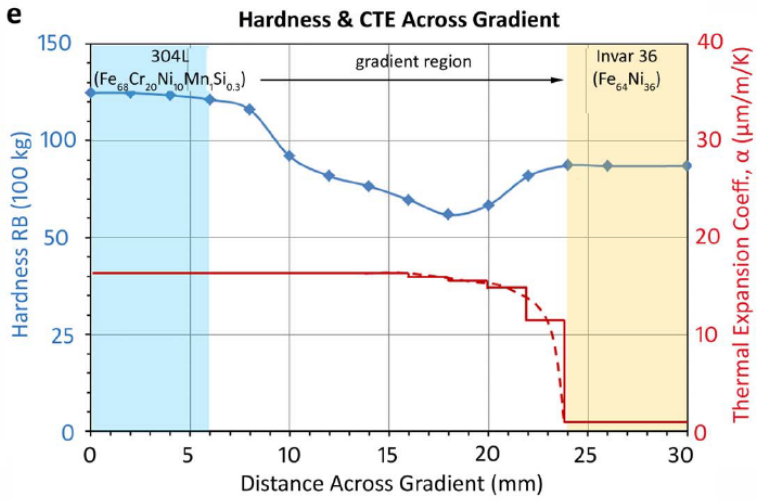

Figure 2.8. The CTE change due to compositional grading from 304L to Invar 36 can be seen by the red curve. Note each step indicates a different composition used for that distance, and the dashed lined represents the ROM average across the build. Taken from [22].

What is evident from thermal expansion mismatch literature is that in systems where a concern exists in the CTE mismatch, the approach is to minimize that mismatch as much as possible. For FGMs, the CALPHAD approach does not factor in CTE, and the impact of thermal expansion on the gradient is an afterthought. Other FGM methods looking at intermetallic formation and solidification cracking do not consider CTE mismatch. Even for the stainless steel to INVAR FGM, the goal was to grade the composition to known CTE materials, not to alter the

CTE in a designed gradient. Even when other approaches are used to design these materials, experimental methods are ultimately required to test the feasibility of a dissimilar material joint. Overall, these materials do not have a consistent approach to their design and fabrication other than trying to compositionally grade from one desired material to another; therefore, the design of advanced FGMs by tailoring the material properties has largely been unexplored and is the focus in this research.

2.7 Summary

Thermal expansion is an inherent material property that has been shown to be a direct result of interactions on the atomic scale due to thermal excitation. The arrangement of atoms in the lattice and their bonding properties determine how much a material will expand up to its melting point. Macroscopically, the CTE relates a change in temperature to the material's strain response. The CTE is a second-rank tensor, having anisotropy based on the crystal system of the material. This anisotropy has been relatively ignored for metallic materials, even in the handbooks used for engineering design, due to their polycrystalline nature where many have cubic crystal systems. While multiple methods exist to measure thermal expansion, push-rod and interferometric techniques are predominately used. For microscopic evaluation of the CTE, XRD techniques are employed allowing for individual lattice parameter measurements and unit cell expansion.

Significant thermal expansion experimentation and reporting has not occurred since the 1980s, and our instrumentation has improved considerably in the last 40 years. The tables that engineers use to design systems not only should be updated with more recent thermal expansion data, but also are lacking in the anisotropy and orientation data needed to design or understand and tailor the thermal expansion. For example, the standard references only lists mean CTE from

typically one source at different temperature ranges [79]. Also, some thermal expansion references provide empirical best fit models that help predict what the CTE would be across a wider temperature range; however, the models do not account for the error or spread of the data [80]. Additionally, many other reference handbooks [15], [81] ignore the fact that the thermal expansion coefficient is a tensor not just a scalar quantity since it can be approximated as scalar for many metals. Another issue is the lack of the variance or error reported in the reference handbooks. Finally, when discussing alloy content on the ability to alter thermal expansion, it was suggested that intermetallic compounds would always increase the thermal expansion; however, no explanation was given to provide a scientific basis for this argument.

Many CTE prediction methods have been proposed for a wide array of materials. Of these methods, ROM is the most widely used, and it provides a reasonable prediction in certain cases. Metal alloys provide a more complex case than well-characterized composites due to the differences in bonding and the crystal structure of the phases involved, potentially limiting the accuracy of the prediction models. The Thomas model has shown some promise in stainless steel welds, but it is based on a semi-empirical fit of measurements from particle-reinforced composites. In other multicomponent materials, the primary technique in mitigating thermal expansion mismatch is to match CTEs as closely as possible. When matching cannot be accomplished, either a ductile layer is used to accommodate the stress or an intermediate CTE layer is used. Currently, none of the methods used to design FGMs accounts for the variation in CTE and mismatch across materials. Ultimately, the CTE mismatch in many attempted FGMs will cause build failure. Due to the lack of understanding of the thermal expansion behavior in metal alloys, more knowledge is needed to be able to tailor it in metallic FGMs.

In the next chapter the experimental method for direct thermal expansion measurements is provided along with experimental factors that could affect the measurement results.

Experimental results from both wrought and AM commercially pure titanium are presented to determine any additional challenges that may exist due to the processing technique.

Chapter 3

THE EFFECT OF PROCESSING ROUTE ON THE MACROSCOPIC THERMAL EXPANSION OF TITANIUM

In this chapter, the AM titanium process is described and the details of bulk thermal expansion measurements are discussed. Then the conversion of dilatometry data to the bulk CTE is presented along with different ways of viewing the data. Finally, the thermal expansion of AM titanium is compared with wrought values and the effect of hot isostatic pressing on the CTE is presented.

3.1 Additively Manufactured Titanium

A grade 1 titanium block was additively manufactured on a grade 2 titanium substrate. The 1.4 in long by 0.65 in wide by 0.72 in tall block was additively manufactured on an Optomec LENS MR-7 DED system at 425W and 25 inches per minute. The hatches only run in the y-axis with a 0.040 in hatch spacing and was built in 3 sets of 20 layers, with 0.010 in, 0.012 in, and 0.014 in layer heights respectively. An outer contour was run followed by an inner contour at the end of each layer. The titanium powder had a powder size distribution of 45 μm – 106 μm and was sourced from LPW (Imperial, PA). Tracks were deposited only in the y-axis, and the build direction is in the z-axis. From this block, samples were extracted using wire electrical discharge machining (EDM) in the longitudinal (blue), transverse (green), and vertical (red) orientations as seen in Figure 3.1. The blue and green samples are considered to be ‘in-plane’ with the deposition (in the x-y plane) while the red vertical samples are perpendicular to the ‘in-plane’ samples as they align with the vertical build direction.

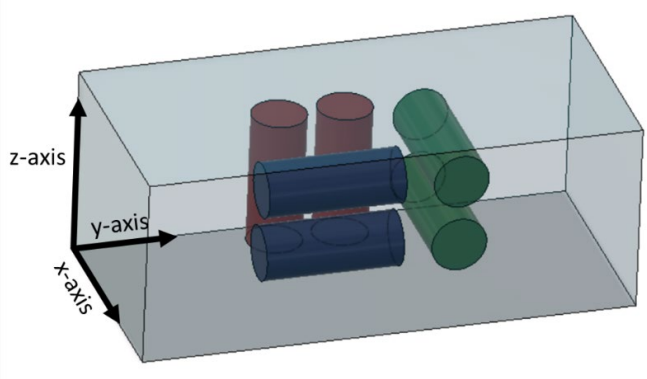

Figure 3.1. Sample orientations taken from a 36 mm long by 17 mm wide by 14 mm high block of additively manufactured grade 1 titanium.The blue and green samples are considered in-plane and the red samples are in the vertical orientation.

3.2 Macroscopic Dilatometry Measurements

One of the prevalent techniques for measuring the CTE is push-rod dilatometry. All macroscopic CTE measurements in this research effort were performed using a push-rod TA Instruments DIL805A Quenching Dilatometer with an alpha sled, shown in Figure 3.2. The alpha sled was designed for thermal expansion measurements offering a single push-rod setup with greater accuracy over the dual rod setup of the standard displacement sled. An induction heater is used to control the sample temperature on the DIL805A, requiring 4 mm diameter by 10 mm long cylindrical samples. Standard procedures exist for performing these measurements in order to ensure quality measurements and are defined by ASTM E228-17 [82]. Reliable and accurate acquisition of this data requires special care beyond what is provided in the ASTM.

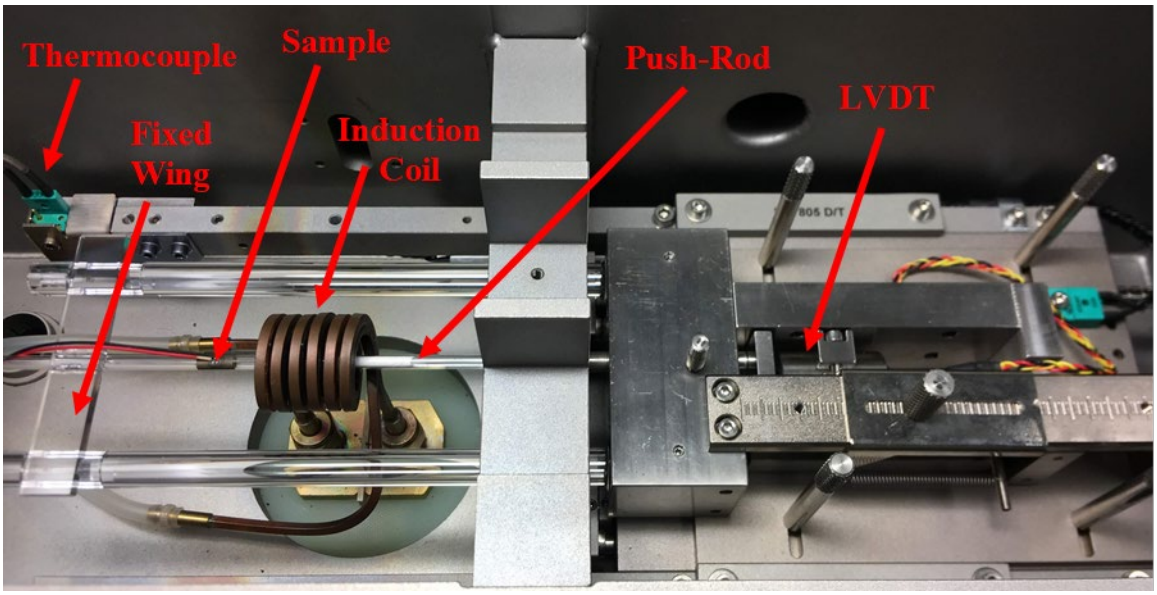

Figure 3.2. TA Instruments DIL805 Alpha experimental setup. The entire sled is moved to the right before starting the test, positioning the sample directly in the center of the induction coil.

Sample preparation is critical to obtaining a good measurement. Specimens were extracted from AM samples using wire EDM into 4 mm diameter by 10 mm long cylinders. Initially, the sample ends were carefully sanded to remove any scale and after a fit-check against the push-rods, were re-sanded until even contact between the sample and both push-rods was maintained. In the end, it was determined that surface grinding the sample ends provided an orthogonal sample with the best finish and is recommended for future measurements. Even with surfacing grinding the ends, sanding was still required on the sample sides to remove the EDM scale, stepping up from 320 to 400 to 800 grits. The sample was then placed between the push-rods and gently rotated to ensure good contact between the ends of the sample and the push-rods. A ‘K-type’ thermocouple was used to measure the temperature in the specimen, and the sample wires were welded to the middle of the sample lengthwise. The ends of the thermocouple wires do not touch, making the current flow through the sample, achieving a more accurate temperature measurement. The sample geometry and thermocouple setup are shown in Figure 3.3. Finally,

each sample was measured with a micrometer prior to test start to obtain the room temperature initial length value, L_0.

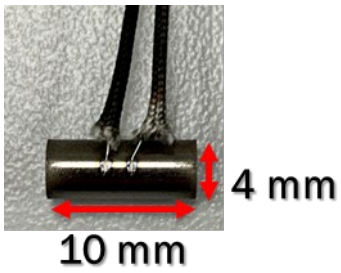

Figure 3.3. Sample geometry and thermocouple placement. The cylindrical samples are 4 mm in diameter and 10 mm long. The K-type thermocouple wires are welded to the sample forcing the current to flow through the sample give a more accurate reading.

When setting up the experiment, the highest precision is achieved through heating to the desired temperature of interest and holding until the displacement is within ± 2 µm [82]. However, a dynamic displacement measurement can be collected if the heating rate is less than 5ºC/min, which allows for more evenly distributed heating [82]. When using this method, the measured temperature will be different from the average sample temperature, but it can be accurate when calibrated with a reference standard [82]. The temperature program for all CTE experiments is run from room temperature to 500ºC at approximately 4ºC/min to heat slowly enough to use the dynamic measurement data. Once the temperature was raised to 500ºC, it was held for an hour to ensure the displacement at 500ºC was constant and to report a more accurate CTE value. Afterwards, the sample was cooled at the same rate to ensure that thermal shock was not introduced to observe the cooling CTE.

The starting room temperature for each test fell between 20ºC and 25ºC. Initially, the LVDT is set to 0 µm at the test start and measures the net displacement at each incremental data point. The experimental profile can be seen in Figure 3.4 with representative data given. A slight

curve at the beginning of the test occurs due to the slower initial heating ramp needed for the program to catch up with the sample, as the test starts at room temperature, and the program starts at 0ºC. Instrument precision with the alpha sled is 0.05 µm for the LVDT length change and is 0.05ºC for the K-type thermocouple temperature change.

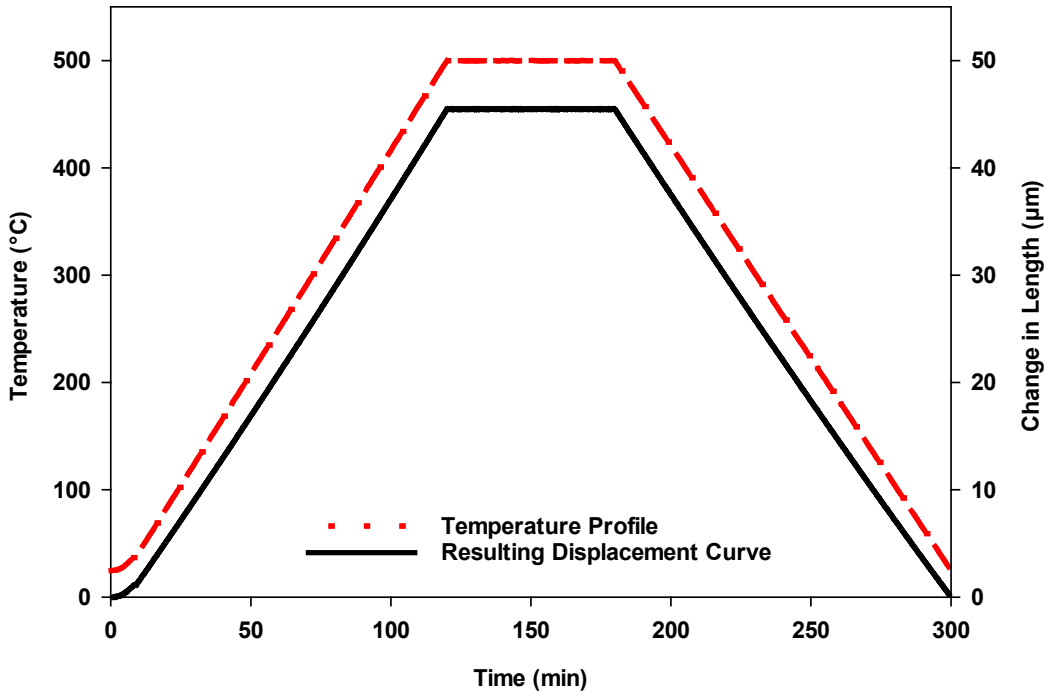

Figure 3.4. An example data set showing the experimental temperature profile and the resulting displacement curve. The sample is heated at approximately 4 ºC/min until a temperature of 500 ºC and then it is held for an hour before cooling at the same rate.

The fused silica push-rods are in contact with the sample during the test, and they heat up due to heat transfer from the sample. In order to compensate for the push-rod expansion, a platinum reference standard is run using the same temperature program that is used for the sample. A correction is calculated from subtracting the known reference values for platinum from platinum sample data set, obtaining a system correction for each data point collected. This correction is subsequently applied point by point to the sample data set, compensating for any

additional expansion of the dilatometry equipment and push-rods. As the equipment was shared amongst researchers, platinum reference data sets were taken any time the configuration of the machine was changed and then returned to the thermal expansion measurement configuration, providing a new correction for that exact setup.

3.3 Conversion from Dilatometry Data to the CTE

The displacement curve is then converted to a CTE at each data point using Equation 2.2, which can be automatically performed by the software, and an example dynamic CTE curve can be seen in Figure 3.5. Note that the temperature and length shown in Figure 3.4 are consistently smooth lines, while the dynamic CTE curve in Figure 3.5 has some fluctuations. Although the instrument has extremely high precision in temperature and displacement measurement, the heating process control creates small fluctuations in the actual temperature and even though the data reported is accurate, it is a limitation of this particular instrument.

For this research effort, the focus was on the heating portion of the dynamic curves and the 500^{o}C CTE values are reported as the average after the one-hour hold at that temperature. To account for the individual temperature fluctuations, dynamic CTE values are taken every 100^{o}C for multiple samples of the same composition and are plotted using error bars. For the test to be considered valid, the measurement should not change due to thermal cycling; however, for the purpose of this research, the non-equilibrium as-deposited material is investigated and compared against published heat treated data [82]. All tested samples fell well below the ± 20 μm requirement between the starting and ending length required by the ASTM standard even though the as-deposited material was clearly changing during the test [82]. From the ASTM, all data is reported to three significant figures [82]. The results are discussed next.

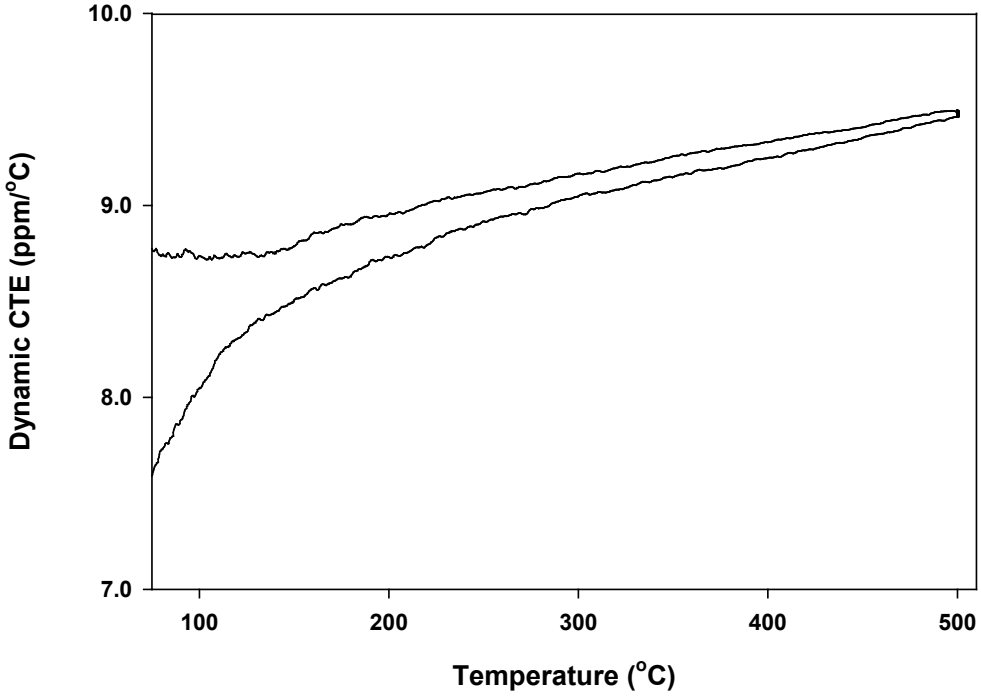

Figure 3.5. Example of a representative dynamic CTE curve converted from the displacement data.

3.4 Thermal Expansion Results of Additively Manufactured Titanium

The samples were tested in the dilatometer and the initial results are plotted in Figure 3.6. As seen in the figure, a notable difference exists in the dynamic CTE behavior for the in-plane transverse or longitudinal samples and the vertical samples for this AM material. The experimental data for AM titanium is observed to be less than that of the reference values [79] at higher temperatures indicating a processing effect on the CTE values. This discrepancy could be either due to track and layer interfaces, grain effects within the material, residual stresses, or some combination of all three.

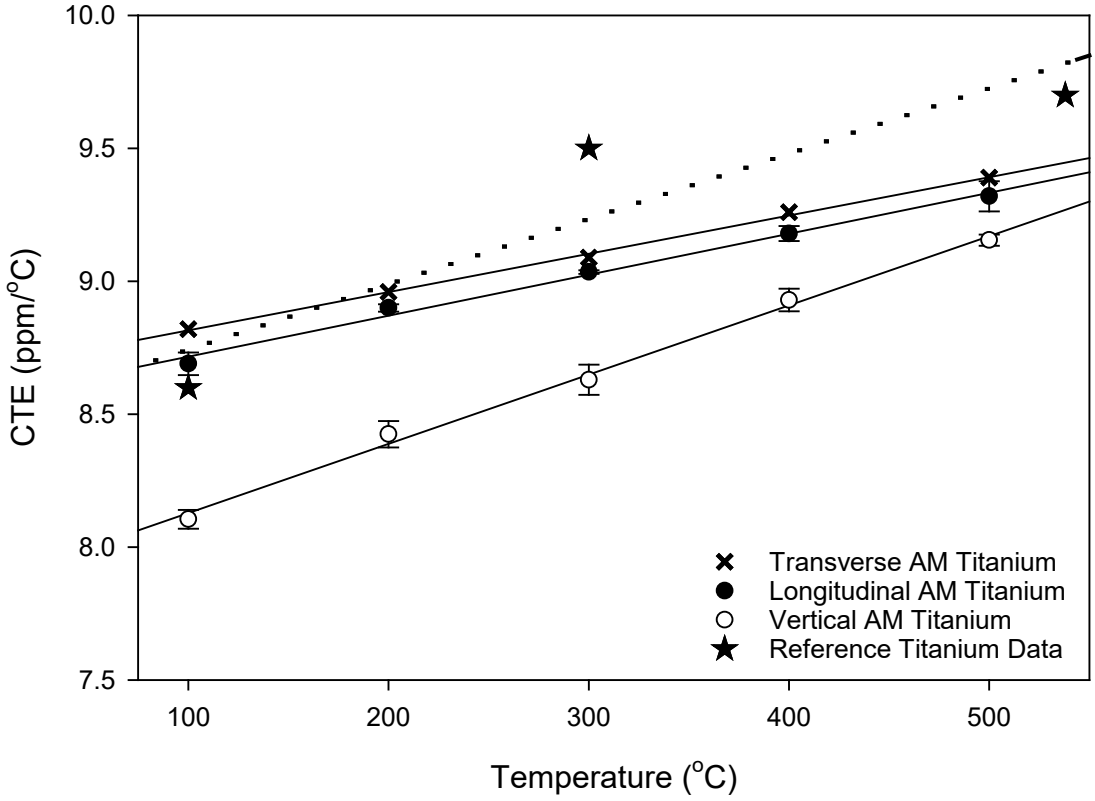

Figure 3.6 The dynamic CTE for additively manufactured grade 1 titanium. Note the observed anisotropy between the samples taken in-plane (longitudinal and transverse) and those that were vertical. The reference data is taken from [79]. The key observation is that additively manufactured titanium behaves differently than the reference values.

Accurate reference data that reflects a particular temperature range of interest is difficult to obtain due to different starting and ending temperatures used. Note that the first two CTE reference values are reported from 20°C while the final value started at 0°C. Based on the data values for other unalloyed grades of titanium (grade 1 – grade 4), the starting point change does not appear to alter the reported value. Furthermore, small chemistry differences in the impurity elements do not appear to have a significant impact on CTE, as the 0-538°C and 20-540°C values falls within 0.2 ppm/°C for all four commercially pure grades of titanium [79]. Based on these data, it is assumed that any small impurity chemistry change due to the AM process has little

effect on the measured CTE. The non-linear appearance of the plotted reference data may indicate that deficiencies exist in the reported literature. Not only are the data values reported from different starting temperatures, but the data is taken from limited sources and does not provide any indication of the error associated with the measurements in the provided table.

In order to further evaluate the difference between the AM titanium specimens and the reference values, two samples were taken from the grade 2 titanium substrate, both in-plane to the plate, to establish a baseline of how much the thermal expansion changed between the processes. The results are shown in Figure 3.7. The first observation is the significantly lower CTE performance of the AM material. Initially, it was believed that something inherent in the AM process was creating lower thermal expansions; however, this is not the case, and it is an important contribution from the research as explained in Chapter 5.

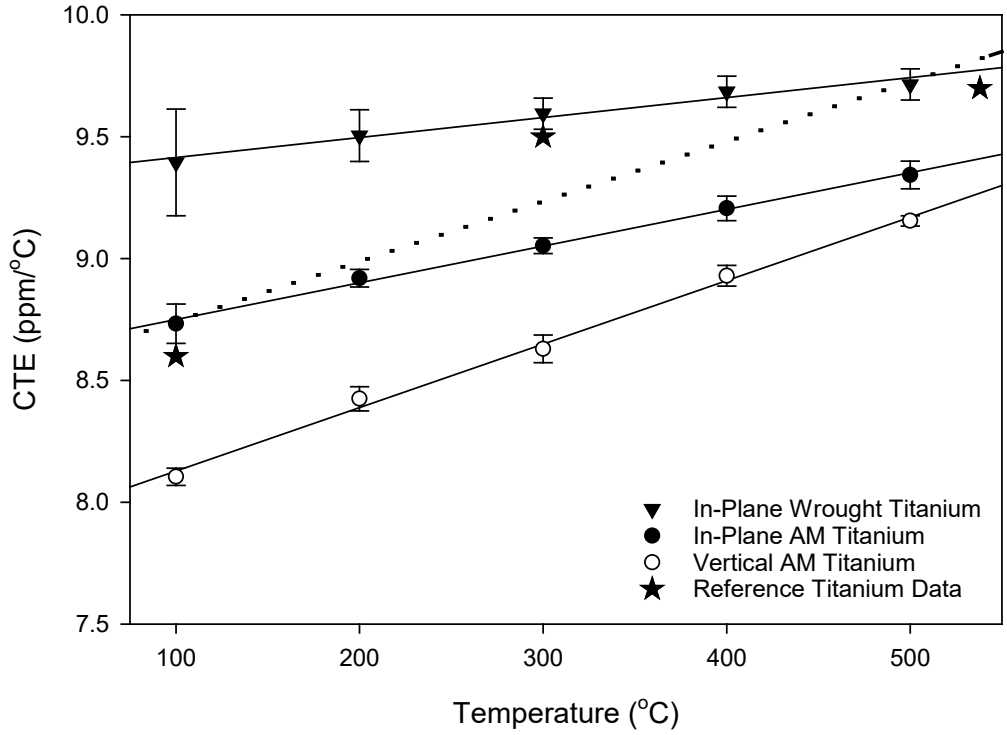

Figure 3.7. The dynamic CTE for additively manufactured grade 1 titanium (circles) compared to in-plane grade 2 wrought titanium plate (upside-down triangles). The reference data is taken from [79] and is the same data for both grade 1 and grade 2. The key observation is that additively manufactured titanium appears to have a lower CTE than wrought titanium, but it will be further explored in Chapter 5.

3.5 Hot Isostatic Pressed Titanium

AM components are typically not used in the as-deposited state as concerns exist surrounding the mechanical performance due to potential build defects. Hot isostatic pressing (HIP) is a common post-processing heat and pressure treatment to close any porosity that may be present and improves ductility, tensile, and fatigue performance if defects are present in the build [83]; however, HIPing naturally coarsens the microstructure, leading to reduced dislocation densities and lower strengths [83]. In theory, the reduction of internal stresses due to any heat treatment should increase the CTE based on the understanding of lattice thermal expansion developed in Chapter 2.

Even though the depositions of AM titanium appeared to have few defects from a thresholding microscopic image analysis, a HIP cycle was performed at 200 MPa and 800°C for 3 hours, to investigate any CTE changes and to compare with the titanium alloy builds in Chapter 4. A lower temperature than what is typically run for Ti-6Al-4V was selected to not cross the alpha to beta transus. The cycle time was selected to match the other titanium alloy systems for comparison. X-ray computed tomography (xCT) was not performed on the AM commercially pure titanium due to a lower apparent defect content from SEM images when compared to the titanium alloys presented in Chapter 4.

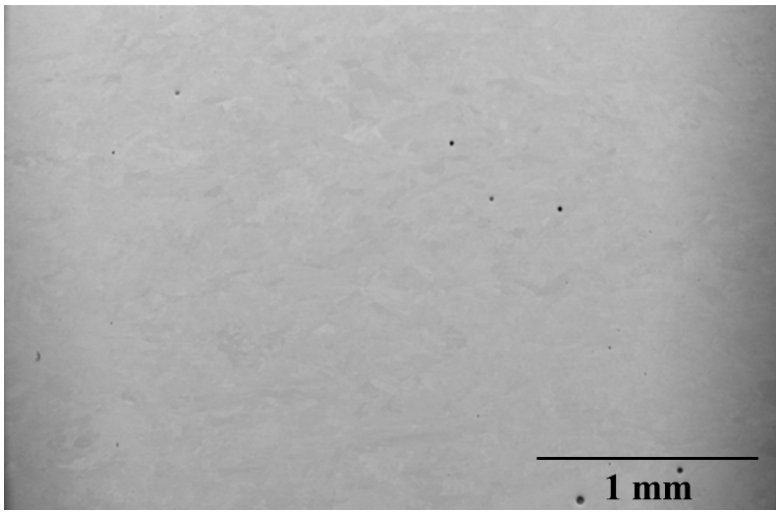

Figure 3.8. AM grade 2 titanium SEM image of the 'as-deposited' state illustrating the small amount of gas porosity that is present in the build.

In the commercially pure titanium CTE experiments (see Figure 3.9), the vertically oriented HIP wrought titanium case shows that the observed anisotropy and lower values from Figure 3.7 were not due to the nature of AM material. The AM and wrought values for the vertical oriented titanium indicate that it is an orientation effect between the in-plane and vertical directions and is further discussed in Chapter 5. Overall, there is significantly less anisotropy between HIP components, and anisotropy appears to decrease with temperature. Additionally, the

in-plane values for the HIP wrought titanium now align closely with the in-plane AM titanium values, but are still less than the reference value of 9.7 ppm/°C. Note that the specimens for both pre- and post-HIP were taken from the same grade 2 wrought titanium substrate. The changes in the material from the HIP process are due to a combination of both temperature and pressure effects.

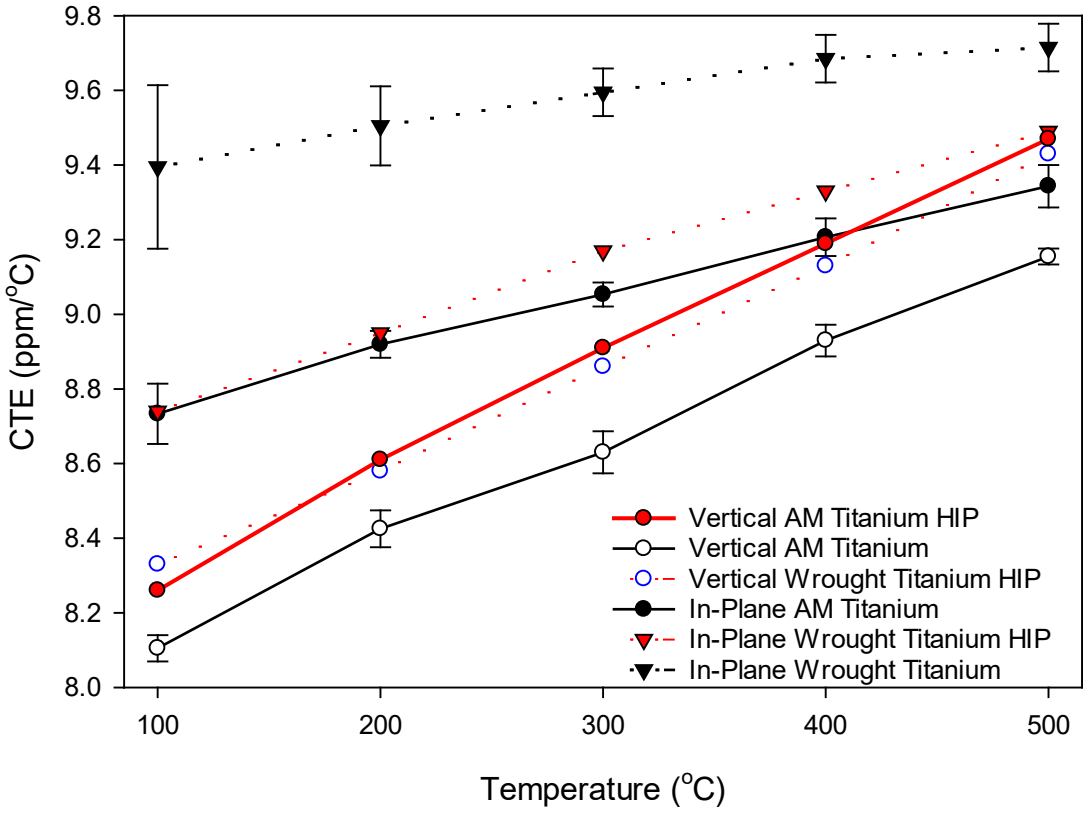

Figure 3.9. A comparison of HIPed condition commercially pure titanium from additively manufactured and wrought processing in both the vertical and in-plane orientations. Note the significant drop in the in-plane wrought value, aligning closely with the in-plane as-deposited AM material. Additionally, the amount of anisotropy observed between orientations is less, almost converging at 500 °C.

3.6 Summary

Push-rod dilatometry was chosen as the test method to evaluate the CTEs of AM materials, specifically titanium, and ASTM E228-17 was consulted to ensure consistent and accurate results. Dynamic CTE testing can be performed accurately given slow enough heating rates when calibrated with a reference standard. Additively manufactured commercially pure titanium was tested and was determined to have lower values than the reference standards published in the literature at higher temperatures, indicating that the AM process yields a different microstructure. Anisotropy was observed in the dynamic measurement curves, showing that if only the 500ºC holds were evaluated, the CTE would appear to be within 0.3 ppm/K of each other.

The manner in which CTE is reported in reference standards and published literature is deficient in the knowledge needed to properly design systems using new manufacturing processes like AM. Historically, the CTE is observed to be linear for most materials, and by plotting some of the reference values, it is possible that some error exists in the reported measurements. Some older thermal expansion handbooks provide an empirical model to predict the CTE at any given temperature which may be the more useful technique for AM metals. For polycrystalline metals with equiaxed grains, any anisotropy should be averaged out due to the random grain orientations. However, anisotropy was observed in titanium system and is explored in depth in Chapter 5. Now that advanced processing techniques like AM are being employed, the way that CTE is reported needs to be reassessed, as current methods are insufficient for designing and controlling the CTE in AM materials.

Chapter 4

ROLE OF ALLOYING ELEMENTS ON ALTERING THE THERMAL EXPANSION COEFFICIENT

With the results from Chapter 3, the difference in properties of AM materials makes FGM design even more important. A new FGM design method is presented in this chapter to assist in selection of candidate alloying elements to produce tailored material properties using AM. The case study used to validate the proposed method involves tailoring thermal expansion in titanium, continuing the work in the previous chapter. Once alloying elements are selected, feasibility testing is need, and a second method is presented to guide this effort. The results of the initial candidate alloys to increase the thermal expansion of titanium using the two new methods are discussed, focusing on alloy composition, thermal expansion results, and the effect of HIP.

4.1 Design Method for Candidate Alloy Selection

Currently, the trend in the FGM design literature is to attempt a compositional gradient between two alloys instead of focusing on actually changing the property of interest. The new design method presented in Figure 4.1 is proposed to determine what elemental blends could potentially be used to create an additively manufactured FGM. The novel aspect of the method is utilizing pure binary elemental blends to achieve the desired function instead of attempting to grade from Alloy A to Alloy B, which has a different desired property of interest. The advantage of working with binary alloy systems is the ability to rapidly evaluate multiple compositions while minimizing the complexity to study the mechanisms involved. As shown in the figure, the method is embodied in a three-step flowchart to select candidate materials for creating a functional gradient.

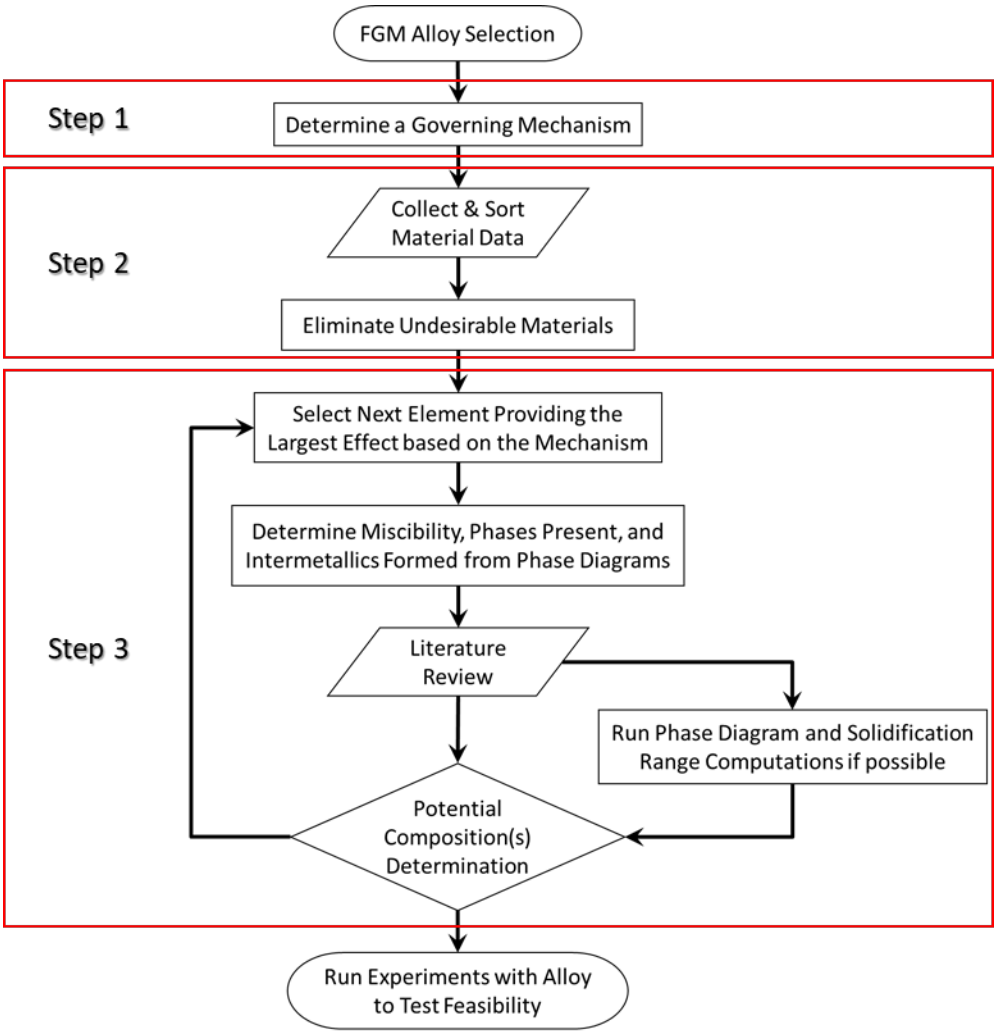

Figure 4.1. A newly designed methodology used to identify and select candidate alloying elements for elementally blended functionally graded materials.

A case study was used to validate and further refine the new FGM design method while providing a demonstration of how it could be employed. For this study, the objective is to increase the CTE of titanium in an attempt to minimize thermal stresses generated due to a mismatch of CTEs at the part interface with another component, the overall focus of this research effort. Using the proposed design method, the first step is to determine the governing mechanism for the intended function or desired performance. For the chosen application, it was predicted that

a ROM would govern the effect of alloying elements on the CTE based on the literature reviewed in Chapter 2.

The second step was to collect relevant data from the literature. Based on the ROM, if the desired performance is an increase in CTE to meet the component at an interface, then the highest CTE elements should provide the largest effect with the smallest elemental volume. Using [79], a table was compiled of elements ranking CTE from low to high. Then undesirable elements were eliminated—elements that were unsafe to handle or process using DED, i.e., radioactive materials, those with high vapor pressure due to volatilization, or those that could react with the laser or environment. In fact, many radioactive elements topped the list, and they were immediately eliminated. Candidates like magnesium and zinc were eliminated due to reactivity and high vapor pressure, respectively. Since the vapor pressure is temperature dependent, the boiling point is used as an indication of the vapor pressure since the liquid and vapor are in equilibrium at that point [84]. Elements with higher vapor pressures will have lower boiling points. A list of some of the highest CTE elements that remain can be seen in Table 4.1.

Table 4.1. Metal elements that were considered in the determination of potential candidates to raise the CTE of titanium in a designed FGM. All data was taken from *[15]* except for [1] which is from *[85]* and [2] which is from *[86]*.

CTE (0-100 °C) (ppm/K)	Element	Symbol	Density g/cm^3	Melting Point °C	Boiling Point °C	Electronegativity[1]	Atomic Radius Angstroms	Young's Modulus GPa	Bulk Modulus GPa	Shear Modulus[2] GPa
26.0	Magnesium	Mg	1.7	649	1090	1.31	1.6	44.7	35.6	17
23.0	Manganese	Mn	7.4	1244	2060	1.83	1.15	191	-	76.4
19.1	Silver	Ag	10.5	962	2200	2.2	1.44	82.7	103.6	30
17.0	Copper	Cu	9.0	1085	2560	1.65	1.28	129.8	137.8	48
14.1	Gold	Au	19.3	1064	2860	2.2	-	78.5	171	27
13.3	Nickel	Ni	8.9	1455	2910	1.9	1.25	199.5	177.3	76
12.5	Cobalt	Co	8.9	1495	2930	1.91	1.25	211	181.5	76
8.9	Titanium	Ti	4.5	1667	3285	1.63	1.47	120.2	108.4	44

In step three, a few elements were selected for investigation of element miscibility, phases formed, and intermetallics formed according to the phase diagrams. A good example is magnesium, which is immiscible with titanium. The phase separation created during processing

could lead to catastrophic build failures as the CTEs are vastly different. Manganese is a strong beta titanium stabilizer and has a significant eutectoid depression, which could lead to beta phase in the final microstructure due to the high cooling rates seen in AM. An additional literature review is required to understand phase and intermetallic formation, along with intermetallic brittleness. For the DED process, brittle intermetallics and large solidification ranges can lead to build failures [18]–[20], [27], [34]. As such, another iteration through elemental selection may be required depending on the result of the miscibility, phases present, intermetallics formed and the solidification range.

In this case study, two candidates—silver and copper—were selected to investigate further. The phase diagrams, seen in Figure 4.2, showed solid solutions at high temperatures along with significant formation of intermetallic phases for both systems. Unfortunately, the CALPHAD data was not available for either system; therefore, welding, brazing, and bonding literature was examined. The literature suggested that the titanium-copper and titanium-silver intermetallics were not brittle, but it did not give much indication of the solidification range other than it was short enough to enable titanium brazing [87]–[93]. Given this result, both candidate systems proceeded to feasibility tests.

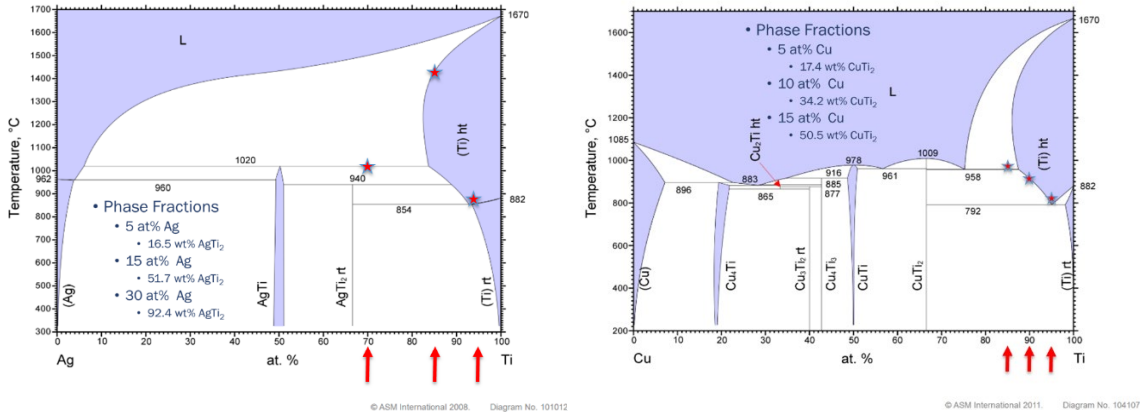

Figure 4.2. The phase diagrams for titanium silver and titanium copper. The arrows and stars indicate compositions chosen for feasibility testing and the phase fractions for those compositions are listed. Adapted from [94] for silver and [95] for copper.

4.2 Method for Feasibility Testing of Candidate Alloy

Once alloy systems have been selected, feasibility tests are conducted to evaluate material performance and a second method was created to guide the process as shown in Figure 4.3. Different compositions were selected from the phase diagrams to test the overall feasibility for alloying titanium. In the titanium-silver system seen in Figure 4.2, 5 at.% silver was selected as a near eutectoid composition; meanwhile, a 15 at.% silver system was selected as the upper solubility of silver in beta titanium. The hope was that solidification rates during AM processing would be quick enough to trap excess silver in solution. A 30 at.% silver composition was selected to test how far the CTE could be increased and study the effect of an approximate 90 wt.% intermetallic phase on system performance. For the titanium-copper system seen in Figure 4.2, 5 at.% copper was chosen as a near eutectoid composition, 10 at.% copper as a hypoeutectoid composition, and 15 at.% copper as it lies just past the solubility limit of copper in beta titanium and is roughly 50 wt.% intermetallic phase at room temperature.

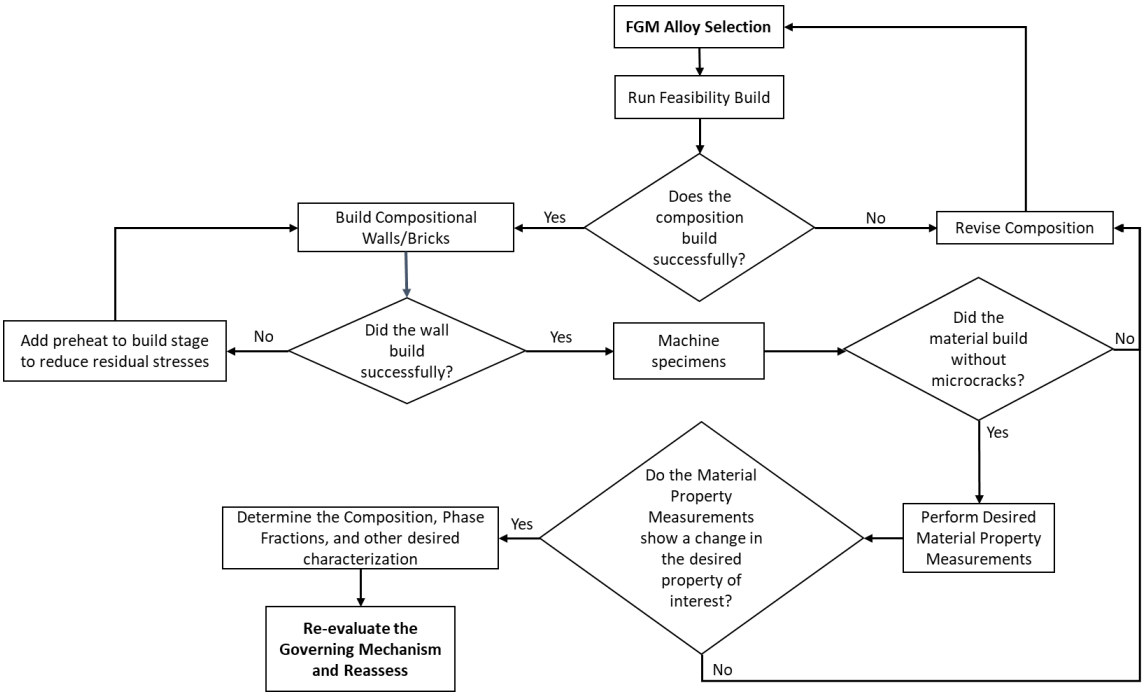

Figure 4.3. Feasibility testing methodology developed for evaluating the performance of selected material systems for the use in a FGM.

4.2.1 Additive Manufacturing of Candidate Systems

Elemental blends for each of the compositions were weighed out and placed into separate containers. The titanium used is the same grade 1 titanium discussed in Section 3.3. The commercially pure copper was also sourced from LPW (Imperial, PA) with a PSD of 53-150 µm while the commercially pure silver was acquired from American Elements (Los Angeles, CA) with a PSD of 43-140 µm. A Turbula shaker-mixer was used to blend the powders of each composition for 30 minutes. The same Optomec MR-7 LENS system was used as discussed in Section 3.2.

As these alloy compositions have not been used before, parameters for Ti-6Al-4V were used as a starting point. Initially, single tracks were deposited on a titanium substrate, followed by 5-track, 7-layer blocks, to refine the processing parameters for each alloy. In the end, the

titanium-silver system was deposited at 400 watts and 20 inches per minute while the titanium-copper system was deposited at 450 watts and 20 inches per minute. All 6 compositions were successfully deposited with no signs of cracking. From each wall, 4mm diameter by 10 mm long cylinders were extracted in the vertical 'z-axis' orientation also known as the build direction (see Figure 4.4) to evaluate microstructures and run CTE testing along with additional analysis as needed. While orientation effects could provide a different CTE in the in-plane direction, this orientation was chosen as the final CTE gradient will be tailored in this direction.

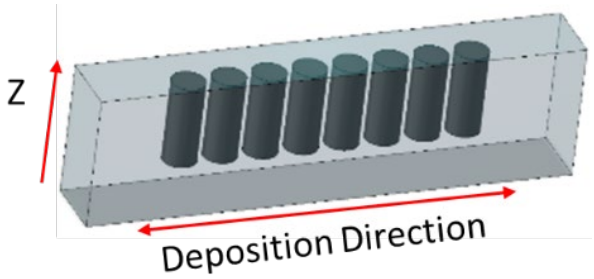

Figure 4.4. Location and orientation of the samples extracted from each alloy system additively manufactured wall.

4.2.2 Build Compositions

Elemental analysis was performed to verify that the composition of each build was approximately what had been mixed as there was a concern that some of the alloying elements were vaporizing during the deposition event. Direct current plasma emission spectroscopy was performed by an outside vendor to analyze the alloy content, following ASTM E 1097-12. Table 4.1 shows the prepared composition versus actual compositions of the builds. The test results indicate excellent agreement between the designed and actual composition with a minor deviation in the 30 at.% silver mixture, which could be a combination of the sample location, settling, and vaporization. Since the two are largely in agreement, vaporization of alloying elements is minimal and ruled out as a factor for consideration when designing future builds in these systems.

Table 4.2. Prepared versus as-built compositions for the elemental alloy blends. The results show that vaporization of alloying elements was not a significant issue and that the blending procedure worked. The final column shows the results in weight percent as that is the more common way to think about alloys.

Alloying Element	Starting Composition (at. %)	Starting Composition (wt. %)	As-Built Composition (at.%)	As-Build Composition (wt. %)
Copper	5.00	6.5	4.93	6.44
Copper	10.0	12.9	10.2	13.1
Copper	15.0	19.0	15.0	19.0
Silver	5.00	10.6	4.96	10.5
Silver	15.0	28.5	14.1	26.9
Silver	30.0	49.1	26.8	45.1

4.2.3 Candidate Alloy Thermal Expansion Results

Since the FGM is created layer-by-layer and is graded vertically, knowing the CTE in the vertical orientation is critical for both the final design and the application; therefore, only the vertical orientations were studied and in-plane alloyed samples were not investigated. The results for the titanium-copper system can be seen in Figure 4.5, and the results for the titanium-silver system can be seen in Figure 4.6. In the titanium-copper system (see Figure 4.5), alloying with 5 at.% copper increased the CTE of AM titanium to be equivalent with an in-plane wrought value. Further alloying provided additional increases that exceed the wrought and reference values while significantly improving the vertical CTE value. The increase indicates that elemental alloying is an effective method to increase the CTE which is desirable due to the materials used in the application, and a functional gradient can be designed using this method. Additionally, the inflection at 350^{o}C was noted and further explored. After careful examination of the heating and cooling curves, the evidence suggested that a material change was occurring; this is investigated in detail in Chapter 5.

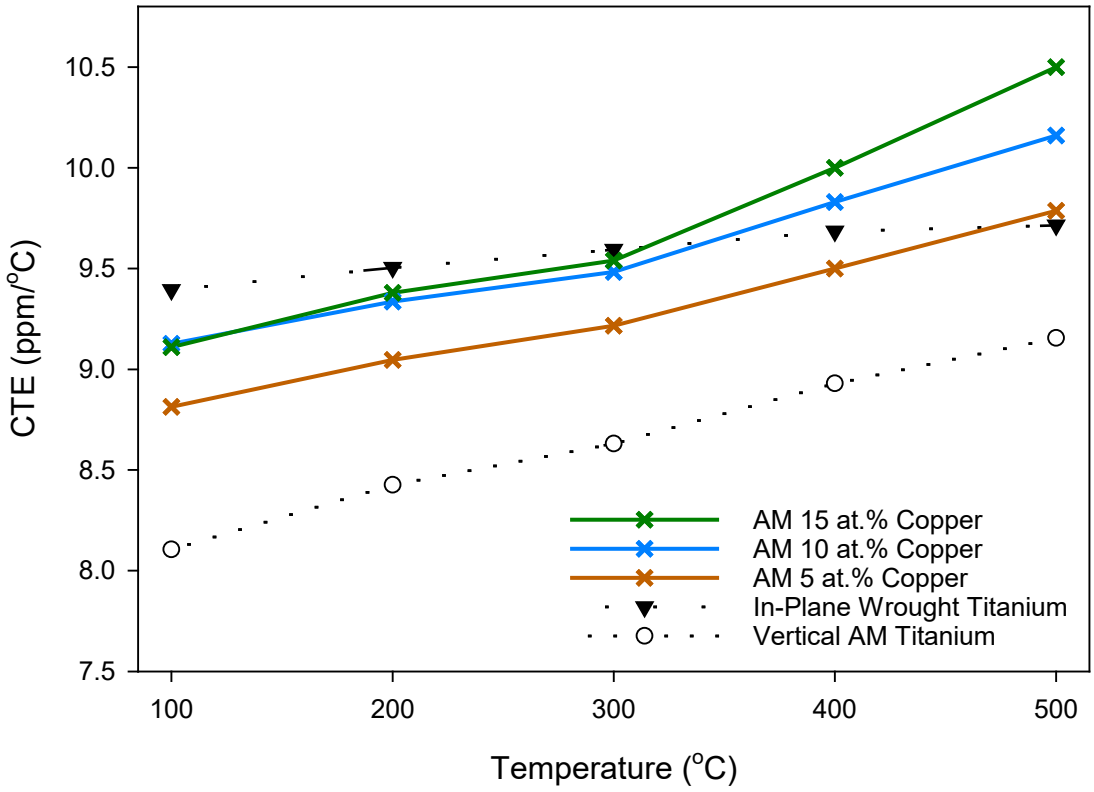

Figure 4.5. The averaged dynamic CTE curves for the additively manufactured titanium-copper system. Each curve represents multiple samples of the same composition with outliers removed. All titanium-copper samples are tested in the vertical direction. At just 5 at.% copper, the CTE of additively manufactured titanium has been increased back to the value of in-plane wrought titanium and significantly improves upon the vertical additively manufactured value. Any additional copper content continues to raise the CTE of titanium.

In the titanium-silver system (see Figure 4.6), alloying with 5 at.% silver decreased the CTE of AM titanium. After further investigation, it was determined that significant interlayer defects existed within the material, providing open space within the sample for the material to expand without increasing the length as measured by the dilatometer. These defects were due to limited parameter development using the highest alloy case, not tailoring it for each individual composition. At higher alloy content, the titanium-silver system had less defects, but it still had some issues. Similar to the copper system, further alloying allowed additional increases that

substantially exceeds the wrought and reported values for titanium. Both the 15 at.% and 30 at.% silver alloys resulted in higher CTEs than the 10 at.% or 15 at.% copper, as expected. This increase confirms that elemental alloying works in multiple material systems and that both methods work. Note that all of these tests were performed on as-deposited material, with no additional heat treatment steps. None of the tests performed violated the ASTM 20 µm deviation between test start and finish, even though the material was changing at 500°C.

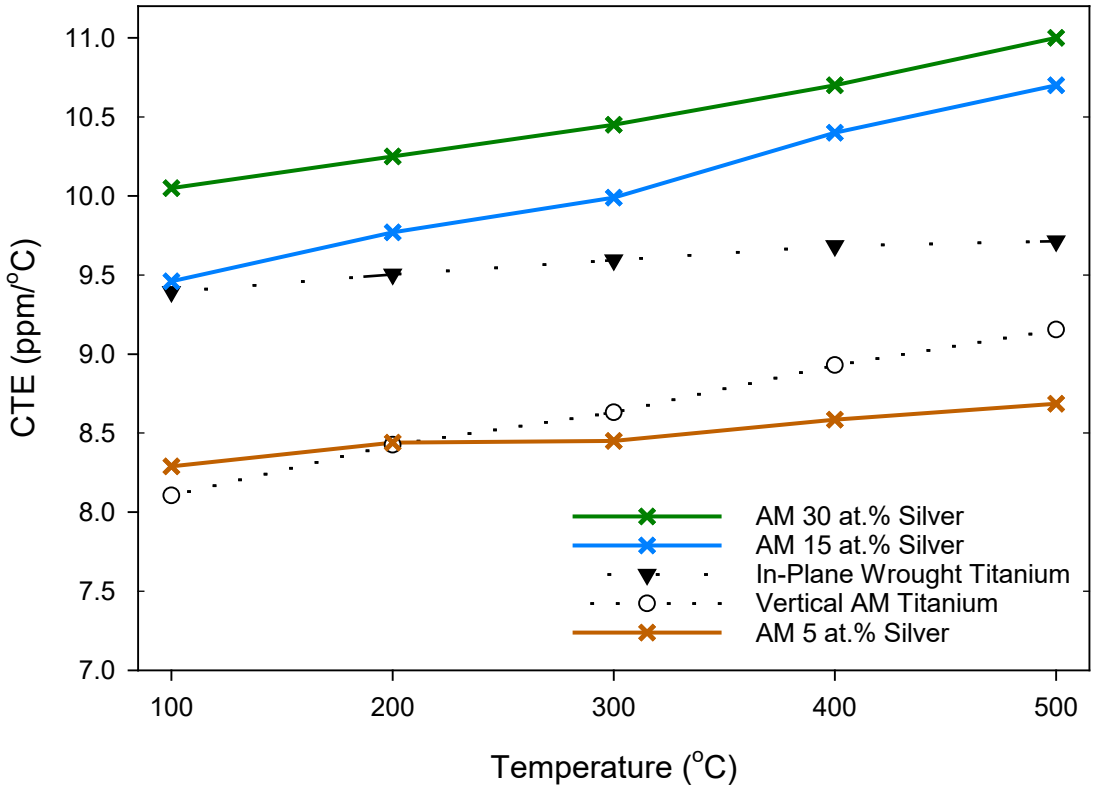

Figure 4.6. The dynamic average CTE curves for the additively manufactured titanium-silver system. In this graph, the average of multiple samples is used and the outliers are thrown out. All the titanium-silver system samples are tested in the vertical orientation. Note the performance of the 5 at.% silver is less than the commercially pure additively manufactured titanium, most likely due to build defects. The 15 at.% performance is close to that of the 30 at.%, both of which significantly increase the CTE of titanium.

4.2.4 Role of Defects

Build inhomogeneities or defects generated from the AM process can further complicate the evaluation of material properties. In all the elemental alloy initial builds, interpass/interlayer defects were present (Figure 4.7), along with unmelted titanium particles (small white circles) and some porosity (black circles). In the titanium silver system, some un-mixed silver was observed in the lower third of the build and the defects decreased with layer height, indicating additional parameter development or process design could eliminate them. For example, hatches could be offset by a half of the hatch distance between layers to eliminate the interpass/interlayer spacing issues, or preheating the substrate could eliminate the unmelted titanium particles. Nevertheless, some inhomogeneities exist that are a result of the materials used.

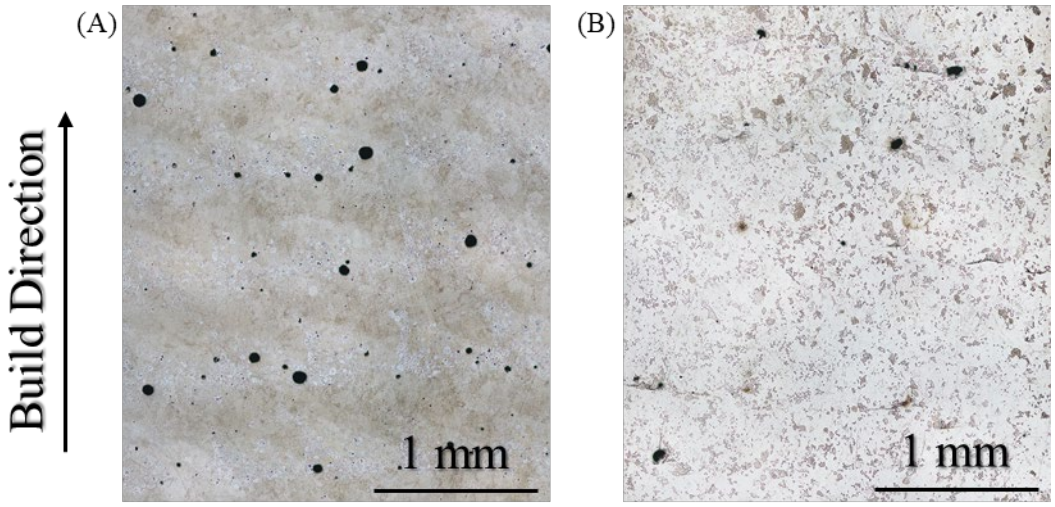

Figure 4.7. Observed build defects for the 15 at.% copper system (A) and the 30 at.% silver system (B) are shown in the as-deposited state. The interpass/interlayer regions are observed with more defects present at those locations. Porosity is shown by the black regions while unmelted titanium is given by small white circles as confirmed with EDS.

Upon completing x-ray computed tomography (CT) scans of the highest alloyed copper and silver builds, it was determined that even with these defects, the lowest density was

approximately 97.8% which was considered reasonable given the limited time spent optimizing processing parameters. Separately, an image area thresholding analysis (see Figure 4.8) was performed on a micrograph and showed that in the 30 at.% silver system, approximately 12% of the build was segregated at the interfaces which is a different defect from the typical porosity. Note that this analysis is looking at the silver and unmelted titanium particles as a whole, observed in the microstructure. In theory, lack of fusion and porosity defects should not affect the bulk CTE measurement, but depending on the arrangement and severity of the defects, it could be altering the results, like in the 30 at.% silver case.

Figure 4.8. A micrograph with image thresholding analysis of the 30 at.% silver sample, showing that while the porosity (from the CT scan) was only around 2.2%, the build inconsistencies or dark regions are around 12%. The dark regions in this image are areas of unmelted titanium particles surrounded by a more silver rich region than elsewhere in the sample. Note that the majority of the defects were eliminated with build height, indicating that further process development could eliminate them.

4.2.5 Effects of Hot Isostatic Pressing

As discussed in Section 3.4, HIP is commonly employed as a post-processing technique for AM components that can heal some of porosity defects in the build as well as alter the microstructure. Differences were observed in the HIPed thermal expansion behavior when compared with the as-deposited state in commercially pure titanium. For these reasons, HIP treatments were performed on the titanium alloy systems at 200 MPa and 790^{o}C for 3 hours. The slightly lower temperature than for pure titanium was selected to not cross the alpha to beta transus in the copper-titanium system. Due to the lower temperature, the cycle time was increased to 3 hours to allow extra time for the material to heal defects. X-ray computed tomography (xCT) showed dense structures in both alloy systems with no resolvable pores with a 16 μm voxel volume and an example for the 5 at.% silver system can be seen in Figure 4.9. This sample was chosen due to the larger number porosity in the build. Note that all the coloration observed in Figure 4.9(A) was determined to be noise, and it was confirmed with the xCT operator that no defects were observed at that voxel resolution as indicated by the zoomed in region shown in Figure 4.9(B) and Figure 4.9(C).

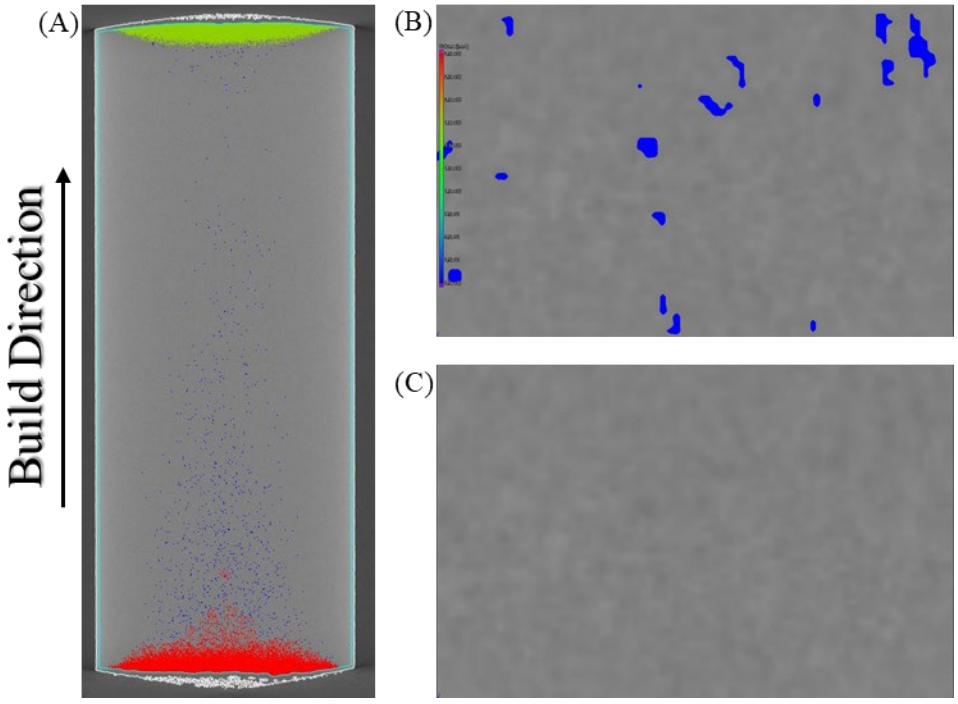

Figure 4.9. (A) xCT image of the HIPed 5 at.% silver system, showing the healing of the porosity in one of the most porous samples. Note that the red, green, and blue coloration was determined to be noise and was confirmed with the xCT operator that no defects were observed at the 16 µm voxel volume resolution. (B) Shows a zoomed in look at the blue defects identified by the analysis software while (C) shows the exact same image without the analysis.

A comparison of the AM titanium-copper system is given in Figure 4.10. As seen in the figure, HIP removed a significant amount of variability between samples and eliminated the change in slope observed around 300°C. As the microstructure coarsens during the HIP process, diffusion occurs, and material trapped in a non-equilibrium state progresses more towards equilibrium. For the 10 at.% and 15 at.% copper samples, the HIP process reduced the CTE by approximately 0.5 ppm/°C at 500°C, while the HIPed 5 at.% copper system had a slight increase in CTE. An updated comparison between the HIPed values for the titanium-copper system and commercially pure titanium is given in Figure 4.11. Now all compositions of titanium-copper increase titanium's CTE, but only a small increase is observed between the 5 at.% and 10 at.% values.

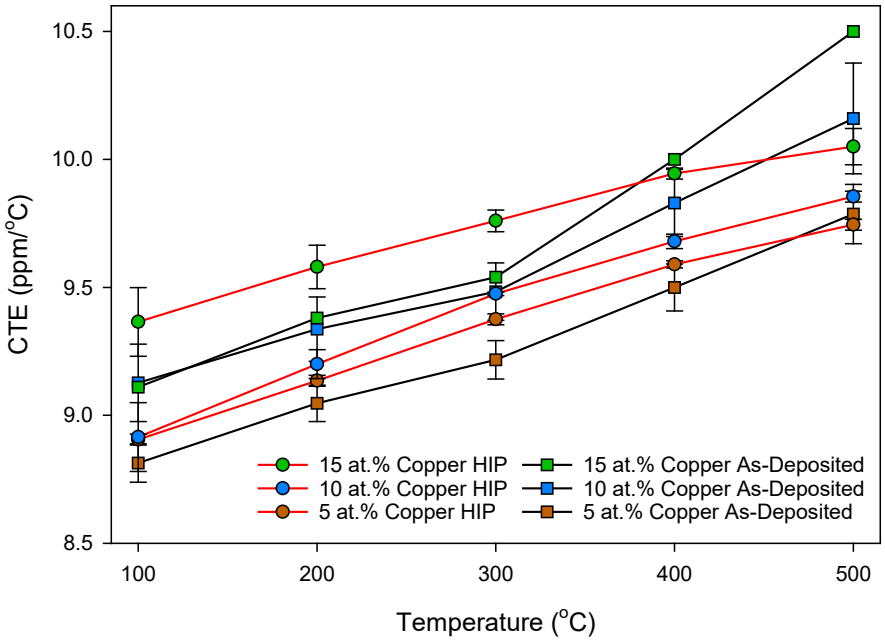

Figure 4.10. The effect of HIP on the titanium-copper system.

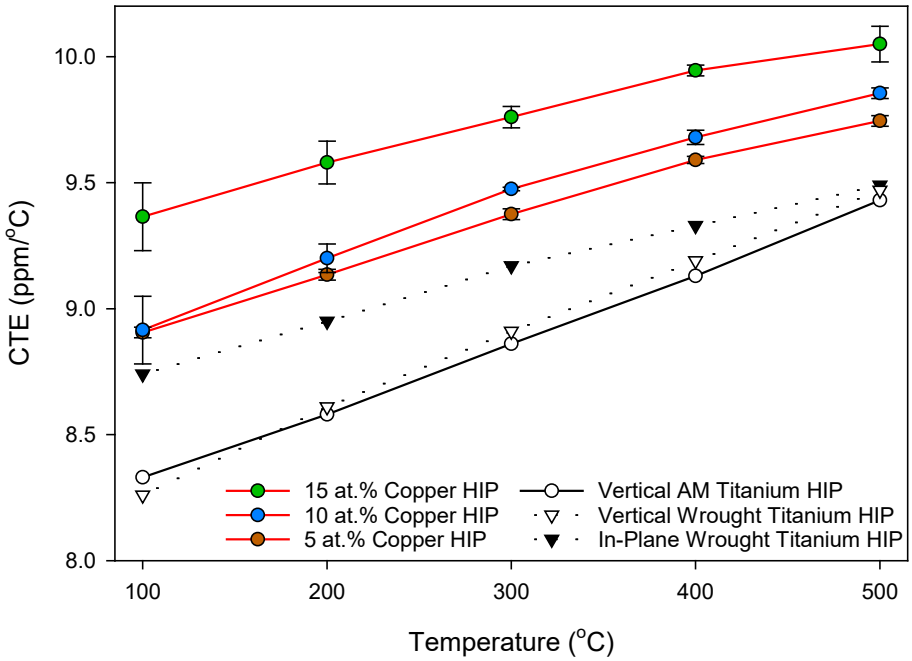

Figure 4.11. An updated comparison on the performance of the titanium-copper system compared to commercially pure titanium.

For the titanium-silver system, a comparison between the as-deposited and HIPed values is shown in Figure 4.12. A substantial decrease of approximately 0.8 ppm/°C is seen for the two higher alloy compositions, while a noticeable increase occurs in the 5 at.% case of 0.5 ppm/°C. An improvement in the sample consistency is observed for this system as well, as the HIP process generates more uniform coarsened microstructures.

An updated comparison between commercially pure and titanium-silver systems is given in Figure 4.13. Due to some build issues identified in the titanium-silver system that would require further process parameter development and the extra cost associated with silver, copper was chosen as the candidate element to proceed with for the remainder of this research effort.

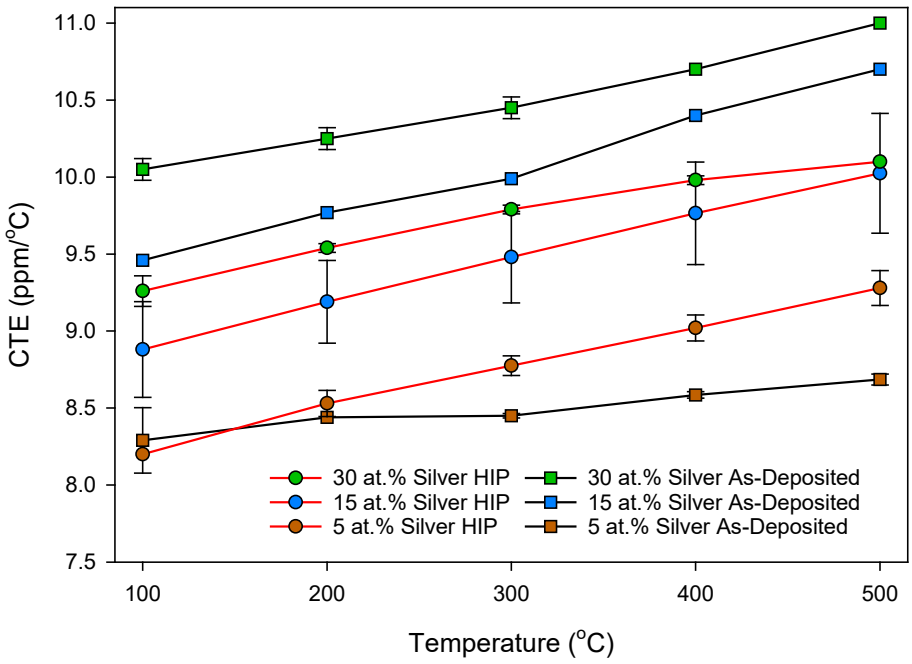

Figure 4.12. The effect of HIP on the titanium-silver system.

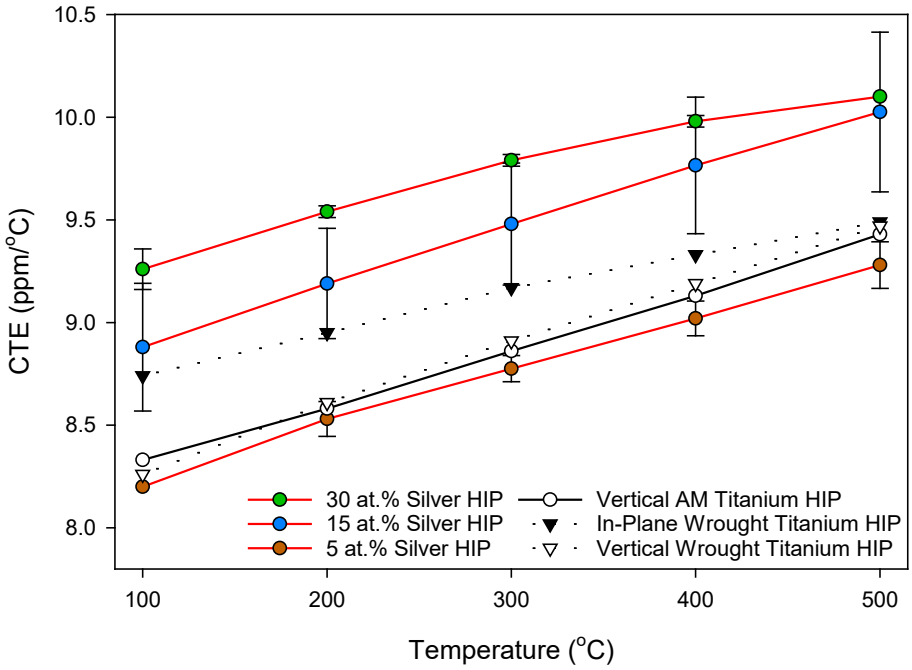

Figure 4.13. An updated comparison between the titanium-silver compared with commercially pure titanium.

4.3 Summary

A new method was proposed and demonstrated to design FGMs using elemental blending. Using the proposed method, the key elements of silver and copper were chosen as candidate alloying elements to modify the CTE of titanium. A second method was introduced to guide feasibility testing of the candidate alloy selected from the FGM design method. Both silver and copper candidate elements were blended with titanium and vetted. Compositionally, the prepared samples matched that of the desired mixtures and vaporization of alloying elements was not a factor. Both material systems showed that the method was an effective tool to select elemental blends and that the CTE of AM titanium was increased beyond the wrought values when blended with each of the alloying elements.

The final step in the feasibility testing method is to re-evaluate the governing mechanism. This is addressed in Chapter 6 after learning more about additional microstructural effects of intermetallic phases and anisotropy in Chapter 5. From these initial feasibility tests, silver clearly provides a larger increase at the same alloy content of 15 at.%. Microstructurally, both systems had some lack of fusion defects at the inter-passes and some unmelted titanium particles. Future depositions required higher laser power to eliminate these issues.

Additive manufacturing defects can adversely impact the CTE of a material but can be recovered with HIP. The inconsistencies due to the non-equilibrium nature of AM and the rapid solidification event during processing can alter the CTE and only can be partially improved due to diffusion limitations and heat treatment tradeoffs. Hot isostatic pressing (HIP) is one of the leading techniques used to eliminate build defects and homogenize the microstructure of the material after processing. HIP was run at 790^{o}C and 200 MPa for 3 hours, and subsequent x-ray CT scans showed that the HIP process closed the porosity defects. Some of the compositional variation at the interpasses were still present after HIP however. For the highest defect compositions, 5 at.% silver and 5 at.% copper, the pre-HIP and post-HIP dilatometry showed a recovery of CTE indicating that build defects can have an impact on the bulk CTE measurement.

Now that the thermal expansion of titanium can be raised through elemental blending, a thorough understanding of the mechanism is required to be able to accurately predict the CTE in order to tailor it. The next chapter examines the impact of the microstructure on CTE in detail to understand the observed anisotropy and the effect of phase fractions. Using the knowledge gained, Chapter 6 introduces a novel approach to predict and tailor the CTE for AM metals.

Chapter 5

IMPACT OF KEY MICROSTRUCTURAL FEATURES ON THE THERMAL EXPANSION BEHAVIOR

Now that elemental alloying has been confirmed as a viable way to increase the CTE, understanding key aspects of the microstructure enables the ability to control CTE. This chapter investigates the challenges associated with additive manufacturing elemental blends and the process effect on CTE and focuses on the titanium-copper system. Microstructurally, the intermetallic phase content and crystal anisotropy is explored.

5.1 Additive Manufacturing Challenges of Elemental Blends

The layer-by-layer nature of the AM process and the cyclic heating experienced by the material inherently creates complex microstructures. As a refresher, the titanium-copper phase diagram is presented again in Figure 5.1, and it is important to note that at 15 at.% copper the microstructure is roughly 50 wt.% $CuTi_2$ intermetallic. The as-deposited 15 at.% copper sample shows a good example of these complexities at extremely high magnifications in Figure 5.2. In the figure, higher atomic number phases containing more copper show up as a lighter color on the image due to atomic number contrast. As such, this micrograph shows the interior of one grain with a copper-rich boundary. A mixture of an extremely fine eutectoid microstructure comprised of pure titanium and the CuTi2 intermetallic layers are mixed with a portion titanium-copper Widmanstätten structure. The laser-based DED process used to additively manufacture these samples consists of rapid melting and solidification, which is subsequently thermally cycled,

creating a complex microstructure trapped in a non-equilibrium state that is non-uniform. This microstructure makes evaluation of the mechanisms controlling CTE difficult.

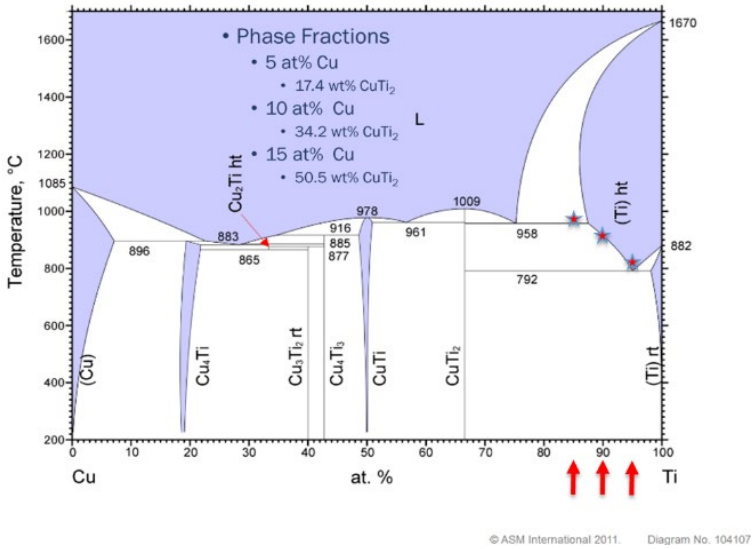

Figure 5.1. The phase diagrams titanium copper. The arrows and stars indicate compositions chosen for feasibility testing and the phase fractions for those compositions are listed. Adapted from [95].

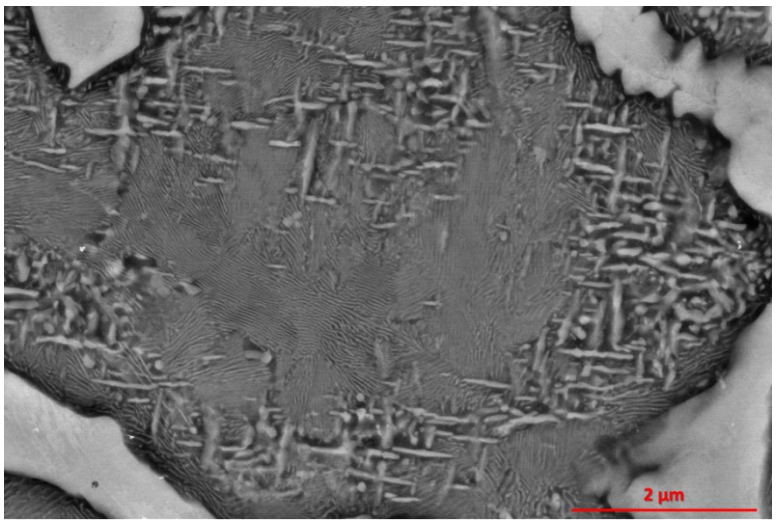

Figure 5.2. Complex microstructure within a grain due to the composition and the additive manufacturing process in the 15 at.% copper system. Note the lighter areas contain more copper than the darker areas. A higher copper content material is on the grain boundary while a eutectoid microstructure of an alpha titanium copper solid solution and CuTi2 layers is mixed with Widmanstätten structured higher copper content material.

Since the compositions were elementally blended, there was a concern that the deposited material would be heavily segregated. While some of the inhomogeneities discussed in Chapter 4 were observed at the interpass/interlayer spacings, Figure 5.3 provides the SEM energy dispersive x-ray spectroscopy (EDS) images, showing an overall thorough mixing throughout each distinct track in the titanium-copper build. At the 5 and 10 at.% copper, the material appears homogeneous with small precipitates; however, at 15 at.% copper, the solid solution was exceeded, and a portion of the copper is pushed out to the grain boundaries as the second phase, intermetallic $CuTi_2$.

The formation of the second phase occurs due to the system driving toward the equilibrium state given by the phase diagram, Figure 5.1. In this material system, faster cooling rates could theoretically limit the conversion from copper in solid solution with beta titanium to the two phase region; however, subsequent layers and post-process heat treatments would effectively eliminate any rapid cooling rate effects and bring the material closer to equilibrium. Future experiments are needed to investigate the effect of cooling rate on phase fractions. The observed good mixing within a track (see Figure 5.3) confirms that the elemental blending procedure provided a reasonably consistent composition throughout the build and is reasonable for creating FGMs. While elemental analysis and EDS can provide compositional information, it does not provide information on the phase fractions.

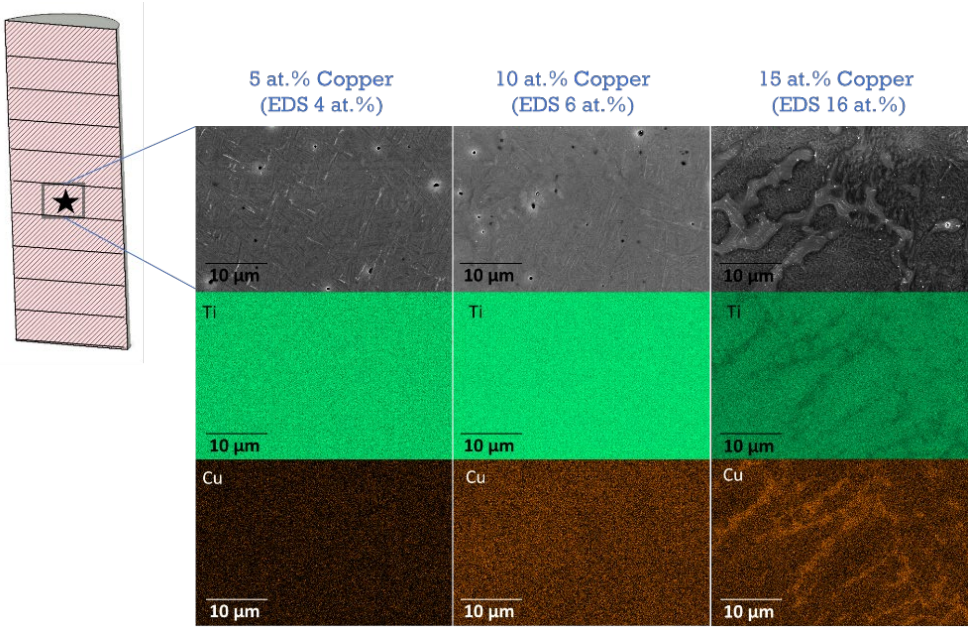

Figure 5.3. SEM micrographs with corresponding EDS maps for each composition examining a single track of a middle layer within the build. The titanium-copper system showed good mixing with a needle like structure at lower compositions. Beyond the solid solubility limit, additional copper resides at the grain boundaries as seen in the 15 at. % copper composition.

5.2 Phase Fractions

Since the depositions are reasonably mixed and of the desired compositions, all of the prediction methods are based on the volume of the phase fractions present. Based on the phase diagram shown in Figure 5.1 the 15 at.% copper alloy has 50.5 wt.% of the $CuTi_2$ intermetallic phase. An x-ray diffraction (XRD) analysis was performed to determine the phase fractions present in the material. In the as-deposited condition, the 15 at.% copper only had approximately 42 wt.% of the $CuTi_2$ intermetallic, which is 8.5% less than what is expected. Even repeated tests of the same titanium-copper sample resulted in different thermal expansion measurements, and the change can be seen in the dynamic CTE curves of the as-deposited material in Figure 4.5.

For the 15 at.% samples, the intermetallic phase fraction increased by approximately 3 wt.% to 45 wt.% $CuTi_2$ after progressing through the CTE experimental measurement on the

dilatometer. This increase is due to the significantly higher diffusion rate of copper in alpha titanium than other metals in alpha titanium with a D_0 value of 3.8 x 10^{-5} m^2/s [96]. An as-deposited sample that was subjected to HIP showed an intermetallic phase fraction of approximately 44 wt.%.

Heat treatments like HIP can provide benefits and losses with respect to thermal expansion. The relief of internal stresses should aid in increasing a material's thermal expansion, and the reduction of build defects is important for material performance. However, since the material is in a non-equilibrium state, any heat treatment or elevated service temperatures will also alter the phase fractions present. Therefore, a heat treatment is important to equilibrate the material prior to use to provide the most consistent thermal expansion performance. Coarsening of the microstructure is observed after the HIP treatment and can be seen in Figure 5.4. From an EDS analysis, the lighter colored material is the intermetallic $CuTi_2$, while the darker material is mainly alpha titanium. In the HIP condition, the $CuTi_2$ intermetallic phase is more evenly distributed. An ImageJ area analysis shows an increase in the $CuTi_2$ intermetallic of approximately 3.2%. Although not investigated here, future work should investigate the impact of the intermetallic content on the mechanical performance.

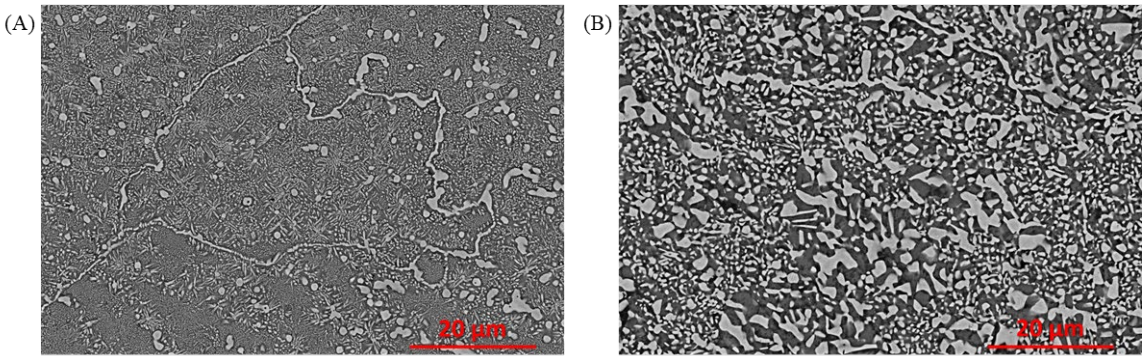

Figure 5.4. SEM images showing the change in microstructure between the as deposited (A) and HIPed (B) samples for the 15 at. % copper alloy system. Using EDS, it was determined that the lighter colored material is the intermetallic $CuTi_2$, while the darker material is the alpha titanium copper solid solution.

While the focus is now on the copper system, it is important to note that the 30 at.% silver composition should have had 92.4 wt.% of the $AgTi_2$ intermetallic and was comprised a much lower value, with a majority of the sample being comprised of a solid solution of titanium with silver and the AgTi intermetallic with the remainder being a mixture of pure silver and $AgTi_2$ intermetallic. In this case, the CALPHAD methods were not close to predicting the as deposited phases due to the nature of solidification of additive manufacturing. The difference between systems is most likely due to the diffusion rates, with copper not only being classified as a fast diffuser (see Section 5.2), but having a faster diffusion rate in titanium than silver. Overall, the rapid solidification event created during AM processing generates phase fractions different from the predictions. These results further corroborate that AM is a non-equilibrium process that produces materials that are not in equilibrium.

5.3 Intermetallic Impact on Thermal Expansion

Clearly the role of intermetallic phases are going to drive the CTE response of a material when a significant phase fraction of the intermetallic exists. If the material was completely a solid solution, then it would be easier to predict thermal expansion behavior [42]. For many systems, the thermal expansion coefficient of an intermetallic phase is unknown. As mentioned in Chapter 2, typical alloys have a more dilute solute content, making the effect of intermetallic CTE less important until now, when complex alloying is being investigated for use in AM FGMs. In this study, neither the $CuTi_2$ or $AgTi_2$ intermetallics had data available, nor any other intermetallics in these systems.

In order to understand how the intermetallic phase alters the CTE behavior of the system, a vacuum melted and cast bar of $CuTi_2$ was procured from an outside vendor. This bar was re-melted and re-formed three times to ensure compositional compliance and material homogeneity.

Both EBSD and XRD confirmed the composition to be $CuTi_2$ as seen in Figure 5.5. Eight samples were extracted from the bar, six vertically and two horizontally, in a 4 mm square cross-section by 10 mm long rectangle using wire EDM (see Figure 5.6). Square cross-sectional geometry was used to ensure flat sides for characterization before and after the CTE experiment. The results can be seen in Figure 5.7, with $CuTi_2$ having an experimentally measured 25-500°C CTE of 10.6 ppm/°C (the reference value is 9.7 ppm/°C for titanium and 18.3 ppm/°C for copper) [79], [97]. A larger variance was observed in the data when compared to other material tests, and it was determined to not be a product of composition, phase fractions, or internal stresses. This variance can be attributed to anisotropy of the thermal expansion of the $CuTi_2$ crystal. The observed anisotropy is discussed next.

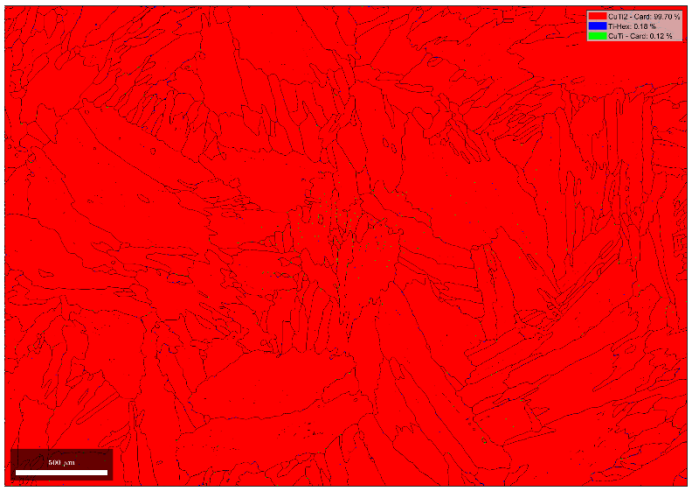

Figure 5.5. An EBSD image of the $CuTi_2$ cast intermetallic bar showing the composition to be 99.7% $CuTi_2$ as represented by the red color.

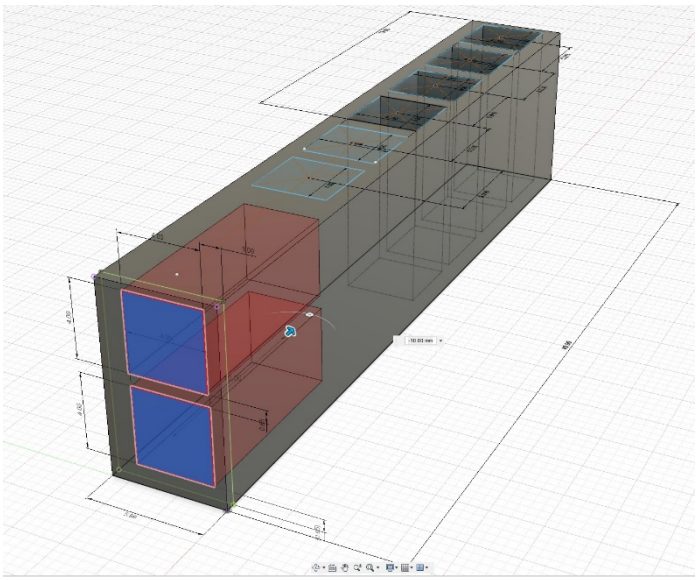

Figure 5.6. A schematic representation of the six vertical and 2 horizontal samples extracted from the cast $CuTi_2$ intermetallic bar.

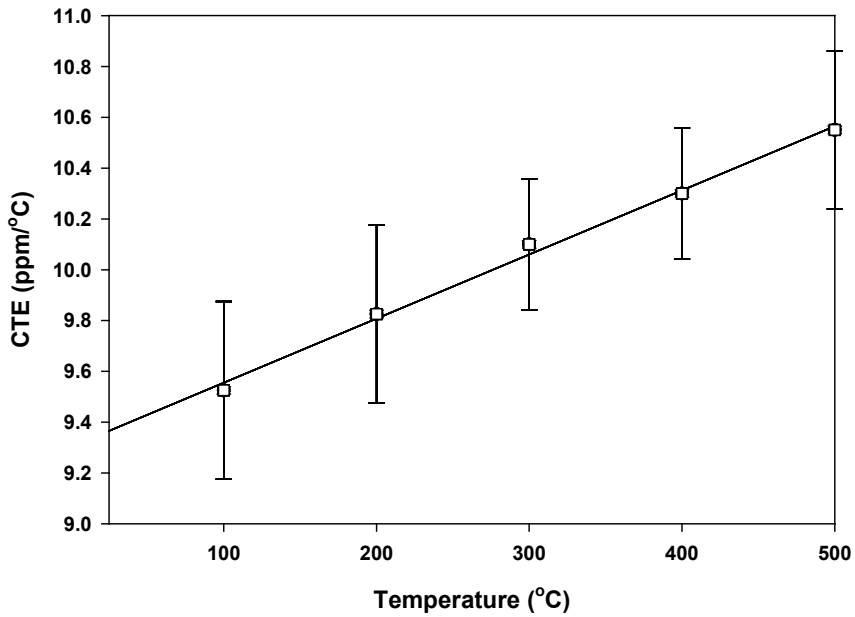

Figure 5.7. The dynamic CTE curve for the $CuTi_2$ intermetallic compound. This provides the data needed to be able to properly predict CTE in the titanium-copper alloy system. Note larger than usual error bars in each measurement are due to the variance across the tested samples. It was determined that this variance was caused by anisotropy in the crystal and not from composition or phase fractions.

5.4 Coefficient of Thermal Expansion Anisotropy

As discussed in Chapter 2, CTE is a second-ranked tensor, having different expansions in different directions based on the crystallography of the microstructure. Table 2.1 shows the number of independent thermal expansion coefficients that are required to fully describe a material, given the symmetry of the crystal system. The general rule of thumb is that the anisotropy is ignored for most materials due to simplicity unless the crystal structure is asymmetric [45]. For metals, many of the crystal systems are cubic, which would only require one coefficient for all directions. In traditional metals, the material is polycrystalline, meaning that it is comprised of many randomly oriented grains. Therefore, if a material is polycrystalline with a truly random crystallographic orientation of grains, then even if the crystal system is anisotropic, the thermal expansion values would average out to a scalar value for any direction due to this randomness. These factors indicate why most engineering reference handbooks only list a scalar value, even for anisotropic crystal system metals. However, the importance of the anisotropic CTE tensor for non-cubic metals, even if they are not additively manufactured is presented next.

5.4.1 Comparison of Additively Manufactured Commercially Pure Titanium to Wrought Titanium

Given the scalar nature of the CTE for most metals and the reference values, the observed anisotropic nature of the CTE for additively manufactured commercially pure grade 1 titanium in Figure 3.6 was surprising to say the least. In order to understand whether this phenomenon was related to the AM process or to the hexagonal titanium crystal system, dilatometry was performed on wrought titanium samples and both the as received and HIPed conditions were tested (see Figure 3.9) The anisotropic nature of the hexagonal crystal system provides an explanation for the

obvious difference for both wrought and AM materials, between the in-plane and vertical orientations.

While this seemed to be a profound discovery, a more thorough literature review uncovered a handful of references indicating the clear anisotropic CTE behavior of non-cubic metals [80], [98]–[100]. Significant discrepancies were identified between the sources and even within the same source on the anisotropic behavior of alpha titanium, which can be seen in Table 5.1. In particular, note the discrepancies between the calculated and reported values from [80]. In [99], the values for 428 K were experimentally found, while the rest of the values were pulled from published results from other authors.

The major discrepancy of this data is that the reported values have the a-axis expanding more than the c-axis, in agreement with one reference, while two others have the c-axis expanding more at the lower temperature range. Upon further reflection on the values in [80], as alpha titanium is being heated, the largest displacement axis swaps from the c-axis to the a-axis between 600 and 700^{o}C. The references in [99] have the exact opposite trend. Both the observed orientation differences in CTE and the literature reported crystal anisotropy lead to the hypothesis that crystallographic texture is driving the CTE difference between the in-plane and vertical orientations.

Table 5.1. Different values for the CTE of alpha titanium in the a and c axis, along with the polycrystalline values. Note the discrepancies between the calculated and listed polycrystalline values from [80] and the tabulated discrepancies from different sources presented by Pawar and Deshpande [99]. One key observation is that between 600 and 700°C, the larger CTE axis swaps.

	a-axis	c-axis	calculated polycrystalline	listed polycrystalline	a-axis	c-axis	polycrystalline
T (°C)	α (ppm/oC)	α (ppm/oC)	α (ppm/oC)	α (ppm/oC)	α (ppm/oC)	α (ppm/oC)	α (ppm/oC)
20	0	0	0	8.6			
127	8.88	9.35	8.97	9.4			
155					9.50	5.6	8.2
225					11.00	8.80	10.30
227	9.23	9.57	9.32	9.9			
327	9.54	9.74	9.61	10.4			
427	9.80	9.93	9.85	10.8			
527	10.04	10.08	10.06	11.1			
600					9.55	10.65	9.92
627	10.26	10.21	10.25	11.3			
700					11.03	13.37	11.81
727	10.47	10.33	10.41	11.5			
	Values from [80]				Values from [99]		

5.4.2 Texture and Crystal Orientation

It has been shown that additively manufactured metals typically have a texture, or preferred crystal orientation [101], [102]. In order to explore the extent of texturing in the commercially pure grade 1 titanium, electron backscattered diffraction (EBSD) analysis was performed. Figure 5.8 shows maps taken from in-plane and vertical CTE samples of the AM commercially pure grade 1 titanium. Note that since the samples are cylindrical, it is difficult to determine which orientation is being examined, other than knowing the direction of the test axis being vertical, or in-plane as described in Figure 3.3. In reality, it is hard to make sense of the additive manufactured titanium map as there is no apparent consistent texture or epitaxial growth of grains. This texturing could explain the anisotropy observed in Figure 3.9. Additionally, since the wrought titanium was hot rolled with the rolling direction in-plane, a rolling texture was

generated, explaining the anisotropy difference in the wrought titanium CTEs, also shown in Figure 3.9.

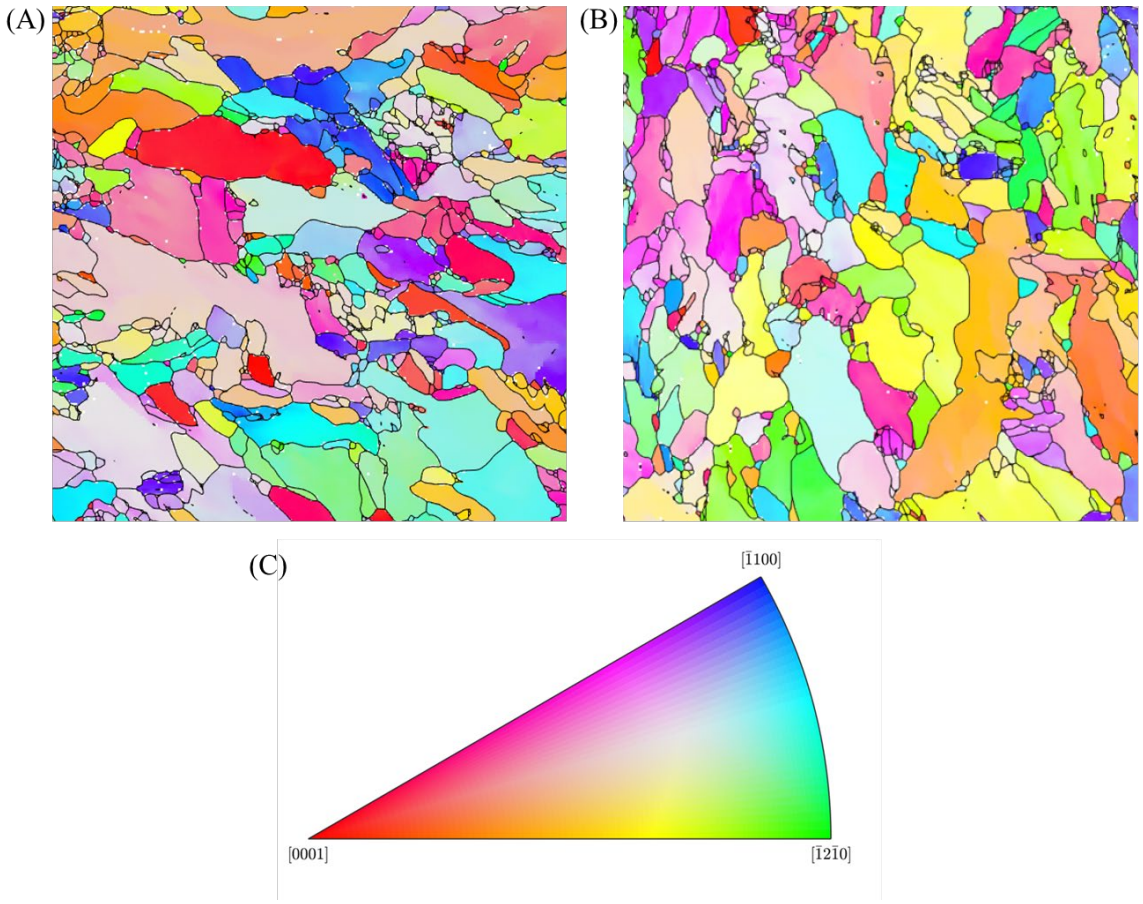

Figure 5.8. EBSD analysis of additively manufactured commercially pure grade 1 titanium, showing an in-plane sample (A) and vertical sample (B) with the orientation legend given in (C).

Given the anisotropy of the wrought titanium CTE experiments, the same EBSD analysis was performed on the wrought titanium plate, and the results are shown in Figure 5.9. In this case, a clear anisotropy was observed between (A) and (B) or (C): (A) has a predominate $[\bar{1}\,1\,0\,0]$ orientation while (B) and (C) have a predominate basal $[0\,0\,0\,1]$ orientation. These results help explain what is causing the anisotropy in the commercially pure single-phase

titanium; however, a further analysis is needed to determine whether if the microstructural orientations can be linked to the macroscopic measurements.

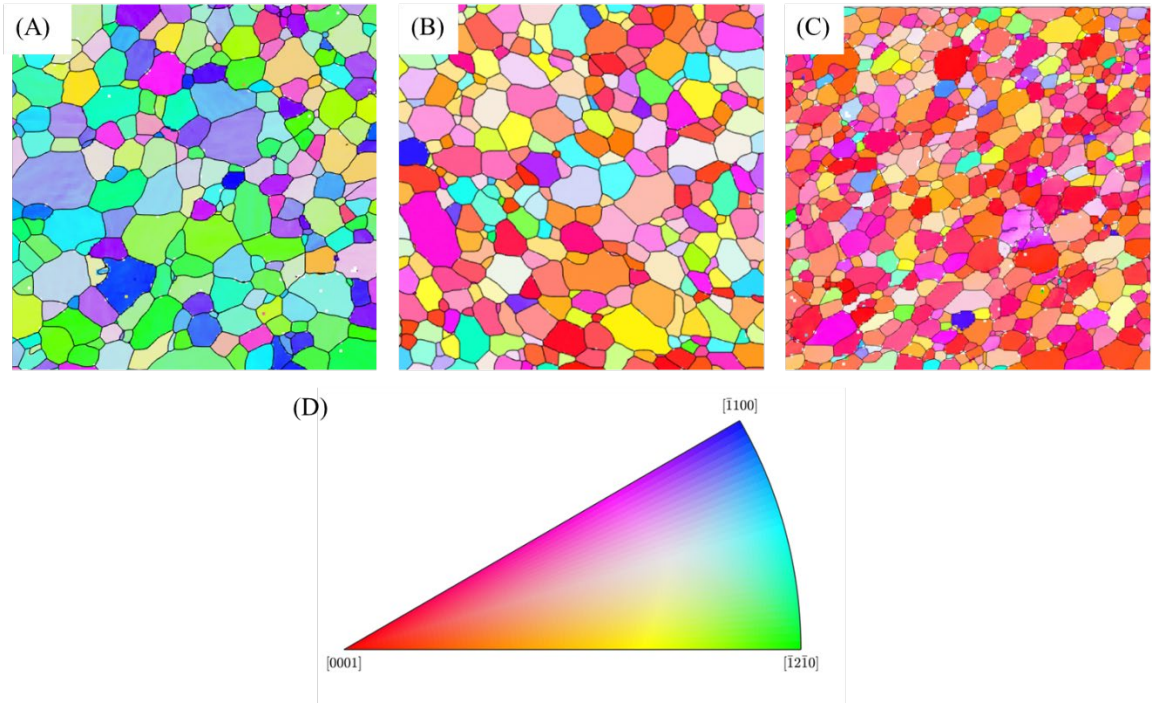

Figure 5.9 EBSD analysis of commercially pure grade 2 hot rolled wrought titanium plate. Note the two maps (B) and (C) that mainly contain the basal plane $[0\ 0\ 0\ 1]$ *and the third map (A) that mainly contains the* $[\bar{1}\ 1\ 0\ 0]$ *orientation. This orientation difference is believed to support the anisotropy observed in the CTE measurement. The orientation legend is given in (D).*

5.4.3 Linking Microscopic Crystal Orientation to Macroscopic Thermal Expansion

Since thermal expansion anisotropy is experimentally observed and could be linked to crystallographic texture (whether obvious or not) in both wrought and AM titanium, methods were explored to investigate the texture based on the bulk CTE measurement. To account for this texture, an average material tensor was used from the open source MATLAB analysis package MTEX [103], [104], which have been shown to work for properties like the stiffness tensor or the CTE tensor [105], [106]. The code was adapted to analyze the thermal expansion tensor by using

the texture information from the orientation density function (ODF) of the EBSD data as an average orientation tensor to the ‘known’ (reference data with discrepancies) input CTE tensor to estimate the average bulk CTE tensor for the whole EBSD map. This was accomplished using the following steps:

1. Calculate the ODF for the desired phase from the EBSD data
2. Define the lattice thermal expansion matrix for the desired phase
3. Define the crystal system for the desired phase
4. Create the CTE tensor using the data from steps 2 and 3
5. Calculate the average texture corrected expansion data using the ODF and the defined CTE tensor which provides the average material tensor for the ODF
6. Sum the columns to gain the expansion in x, y, and z

The MTEX functions utilized in conjunction with the code developed is included in Appendix A. In the first step, a probability distribution function is generated using kernel density estimation with the data segmented into10 degree regions. The second step uses literature or XRD experimental values to define the matrix, while the third step is based on the phase of interest bravais lattice classification. Step 4 combines the data from steps two and three to create the lattice CTE tensor for that phase. Then an average corrected CTE tensor for the material is computed through the use of the calcTensor function in MTEX. The averaging details are discussed in the next paragraph. Finally, the resulting tensor provides the x, y, and z contributions based on the x, y, and z directions. The columns are summed to obtain the net expansion in the x, y, and z image directions. Special attention is required when importing the EBSD data to ensure alignment of the image axes to the sample orientation and factoring in the sample orientation from the original material.

For this calculation, a determination had to be made on whether to use the Voigt, Reuss, or Hill average [105], [106]. The Voigt and Hill averages essentially come back to volume-based averages on the crystallographic scale, which is similar to how the ROM was derived [71]. Once computed for a material set, it was determined that the difference between the Voigt and Reuss

averages was less than 0.03 ppm/K with a standard deviation of 0.004 ppm/K. Given these results, the Hill value [107], a literal average of the Voigt and Reuss values was selected.

Utilizing the MTEX average material tensor capability and the newly written code, CTE tensors were calculated from the EBSD maps shown in Figure 5.8 and Figure 5.9 using the a-axis and c-axis expansion data from [108], which was tabulated in [99]. Note that the lattice reference data reported an a-axis CTE error of 0.5 ppm/K and c-axis CTE error of 0.7 ppm/K [108] which is fairly large. Nonetheless, the values of the resulting CTE tensor are then summed down each column of the tensor to get the net thermal expansion in that direction, which corresponds to the image direction. For example, in the first column, the first value is the contribution to the x-axis thermal expansion by x, the second value is the contribution to the x-axis thermal expansion by y, and the last value is the contribution to the x-axis thermal expansion by z. The results are summarized in Table 5.2 and the code used is given in Appendix A.

Table 5.2 Texture corrected mean 20-500°C CTE values for wrought and additively manufactured titanium. Note values are averaged across different EBSD map Hill averages for the same material.

	AM CP Grade 1 Ti		Wrought CP Grade 2 Ti	
	Vertical	In-plane	Vertical	In-plane
Average CTE	9.84	9.99	9.65	9.98
Standard Deviation	0.015	0.038	0.009	0.115

Between the EBSD maps of the same material, if the axes are similarly aligned, then the difference between images is, at most, 0.24 ppm/K with a standard deviation of 0.029 ppm/K. While these results show similar trends to what was observed experimentally, the calculated CTE tensor for the vertically orientated samples is higher than the experimental values in both cases. Future measurements require extreme attention to detail in tracking exactly what orientation the sample is removed from the specimen and which way it is being measured.

The use of cylinder samples is a poor choice as it limits the direction information. Each face needs to be correlated, e.g., the x direction on a vertical build specimen becomes the z direction on the face of a longitudinal sample during testing. Ultimately, the validity of this CTE tensor is only as good as the a-axis and c-axis CTE reference data that it is given and how well the orientation is tracked to the test axis. Since the lattice axis CTE reference values had a reported error of 0.5 ppm/K or more, these calculated orientation results clearly fall within the reported bulk reference values, but better reference data is needed for more accurate calculations. This is an opportunity for future work that is not addressed in this dissertation. Meanwhile, it is important to note that with the texture correction obtained using the EBSD maps, the observed material discrepancy between wrought and AM titanium (with AM being less than wrought) was eliminated as the AM titanium vertical measurement falls between the spread for the vertical and in-plane wrought values, confirming that orientation is the significant factor; this is a novel and significant finding from this research.

5.4.4 Anisotropy in the $CuTi_2$ Cast Intermetallic Bar

Given the texture present in the AM samples, an investigation into the anisotropic nature of the $CuTi_2$ intermetallic CTE was desired as it is a significant portion of the microstructure at higher copper content compositions. In order to determine the nature of the anisotropy lattice parameter, thermal expansion measurements were performed using in-situ XRD heating on the cast $CuTi_2$ intermetallic bar. A few difficulties were experienced when trying to appropriately measure the lattice parameters. Foremost, this typically would be a powder diffraction experiment, performed with pure materials, to obtain the most accurate results, but this sample is neither. Second, pure titanium and the 50 at.% intermetallic CuTi, both have many overlapping peaks with the $CuTi_2$ intermetallic making the $CuTi_2$ difficult to isolate. Additionally, the

intermetallic cast bar has a preferential orientation on the (103) plane, creating less intensity on other peaks, which increases measurement error. Finally, the bar is heated in atmospheric conditions; therefore, some oxidation occurred on the surface, further altering the results.

Given these difficulties, the Cohen's least-square regression method was initially chosen to calculate the lattice parameters as it tries to optimize across all planes [52]. In order to get a reasonable fit, many shared peaks had to be used, and different peaks were selected from the samples to eliminate the large residuals in the fitted regression model. Additionally, the UnitCell program [109] used to compute the regression did not allow for altering the initial guess; thus, the influence of impurities is greater with the use of more peaks.

A more basic approach of directly employing Bragg's law [52] (given in Equation 2.4) was chosen as a potentially better method. From the EBSD micrographs of multiple samples, the cast bar had more than 99.5% $CuTi_2$ with the remainder being comprised of 0.38% CuTi intermetallic and 0.1% pure titanium. With this additional information, greater confidence was given to $CuTi_2$ peaks that overlapped with CuTi peaks.

The $CuTi_2$ intermetallic has the tetragonal crystal system and the (2 0 0) and (3 1 0) planes were initially chosen as they did not have an 'l' value. From both of these peaks, the a-axis lattice parameter was calculated by solving Equation 5.1 [52] for tetragonal crystals, where d is the plane spacing, (h k l) are the plane miller indices, and a and c are the lattice parameters:

$$\frac{1}{d^2} = \frac{h^2+k^2}{a^2} + \frac{l^2}{c^2} \tag{5.1}$$

Then the a-axis lattice parameter value from each peak was averaged together to obtain the a-axis parameter. Using the averaged a-axis lattice parameter and the (1 0 3), (2 1 3), (2 0 6), and (3 1 6) planes, the c-axis lattice parameter could be determined. These four c-axis lattice parameter values were then averaged together to obtain the c-axis lattice parameter. The same peaks were able to be used for the room temperature and 500°C runs with this method, ultimately tracking the

change in peak spacing. The resulting lattice parameters are summarized in Table 5.3, and due to the intricacies and difficulty of this measurement these values should only be used as a rough estimate.

Table 5.3 The calculated lattice parameters from the XRD measurement of the $CuTi_2$ intermetallic cast bar at room and elevated temperature

Temperature	Lattice Parameter	
°C	a-axis	c-axis
25	2.94053	10.79355
500	2.96104	10.80975

From the estimated lattice parameters, an a-axis, c-axis, and volumetric CTE can be computed using Equations 2.2 and 2.3 respectively. A bulk average CTE was calculated from the volumetric CTE by dividing it by three [42], [98]. The results for the lattice parameters and thermal expansion coefficients are given in Table 5.4. Note the exceptionally large anisotropic nature of the $CuTi_2$ tetragonal unit cell thermal expansion, keeping in mind that there could be a large error associated with these measurements.

Table 5.4. Calculated thermal expansion data from the lattice parameter XRD measurements of the $CuTi_2$ intermetallic.

	Temperature	Lattice Parameter		Volumetric CTE	Bulk CTE
	°C	a-axis	c-axis	2*a + c	(2*a + c) / 3
Alpha ppm/°C	25-500	14.7	3.16		
Beta ppm/°C	25-500			32.5	
Average ppm/°C	25-500				10.8

Comparing this value to the dilatometry data (see Figure 5.7) for the $CuTi_2$ cast intermetallic bar, it was found that the XRD computed bulk average CTE was 10.8 ppm/°C, which is in good agreement with the 10.6 ppm/°C experimental average (a difference of 1.89%).

Additionally, EBSD maps of the $CuTi_2$ intermetallic showed large grains between 100-400 μm, which would further explain the larger than usual variance in the bulk measurement given the anisotropy between the a-axis and c-axis. While this analysis further presents the importance of orientation, the ability to currently control the phase orientation in multiphase materials is limited; therefore, the information gained gives insight into understanding the material behavior not controlling it.

5.5 Summary

Microstructural investigation provides key insights into thermal expansion behavior in multiphase alloys. AM of elemental alloy blends creates challenges in linking the microstructure to the macroscopic properties due to the inherently complex microstructures generated during processing. At lower alloy contents SEM/EDS analysis showed that good compositional mixing occurred within the tracks and elemental segregation was only observed at the interpass/interlayer spacings. With increased solute content in the alloy to achieve desired material properties, the excess copper solute content formed the intermetallic phase $CuTi_2$ and was observed on the grain boundaries and within the grains.

In metal alloys, the formation of multiphase regions containing intermetallics changes the CTE value with increasing significance as the weight fraction of the additional phase is increased based on the composition. XRD analysis was run to determine the phase fractions and investigate changes due to HIP. As the additive manufacturing process is non-equilibrium by nature and has a rapid solidification event, heat treatments like HIP altered the phase fractions, thus changing the CTE. For many alloy systems, this phase change is linked to intermetallic formation. Unfortunately, thermal expansion data is nonexistent for many intermetallic compounds. Since the primary intermetallic for the titanium-copper system, $CuTi_2$, was unknown, samples were cast

and the 25-500 ºC CTE was determined to be 10.6 ppm/ºC. In addition to changing the phase fractions, heat treatments also reduce internal stresses and coarsen the microstructure. In single phase materials, like commercially pure titanium, HIP significantly altered the CTE response, indicating another microstructural factor was involved, crystalline anisotropy.

The processing of titanium created a microstructure with a different texture depending on how it was processed. In the hot rolled titanium plate, a clear orientation difference was observed in the EBSD maps. Due to this texture, the material no longer has randomly-oriented grains, and anisotropy in the thermal expansion measurement is observed for the wrought grade 2 titanium plate. The AM material has comparable thermal expansion performance to wrought titanium.

Literature was discovered that discussed this anisotropy, but major discrepancies existed between the lattice parameter thermal expansion coefficients. Even with these discrepancies, what was consistently observed was a reversal of the larger expanding axis somewhere between 600-700ºC. Selecting the reference values that seemed consistent with the anisotropy observed in the experimentally determined bulk measurements, an average material tensor technique was adapted to adjust the bulk thermal expansion tensor based upon the texture data from the EBSD maps.

The resulting corrected CTEs were now in closer agreement between the processing methods, but an overestimation of the vertical CTE still existed. This is believed to be due to the error associated with the referenced a-axis and c-axis orientation CTE data which showed to have clear discrepancies between different sources. Even with this error, the ability to link the crystallographic microstructure to the bulk thermal expansion measurement, reducing the observed differences in CTE is a significant contribution since it demonstrates that crystal orientation is a primary contributing factor to the experimentally observed orientation differences in titanium.

Since the $CuTi_2$ intermetallic comprises approximately 50 wt.% of the microstructure at 15 at.% copper, an investigation into the potential anisotropy of that phase was performed. Using

XRD and the bulk polycrystalline cast $CuTi_2$ intermetallic bar, in situ heating lattice thermal expansion experiments were performed. It was determined that the a-axis thermal expansion was 14.7 ppm/^{o}C, while the c-axis expansion was 3.16 ppm/^{o}C although some difficulties of this experiment potentially provide a large source of error. Even with these difficulties, it was determined that the polycrystalline bulk average to be 10.8 ppm/^{o}C which is within 2% of the bulk measurement of 10.6 ppm/^{o}C. As the $CuTi_2$ intermetallic is significantly anisotropic, the texture of that phase could significantly impact the final CTE. Additionally, the larger than usual variance in the bulk CTE measurement of the $CuTi_2$ intermetallic cast bar can be explained due to the large grain size, grain texture, and associated anisotropy.

It appears that the institutional knowledge of anisotropic metallic thermal expansion was lost for current material design given the lack of new process development over the past several decades. This is not surprising as it is not a significant factor for other material systems fabricated with traditional processing methods depending on the crystal system and the crystallographic texture of the grain structure; however, now that novel complex materials can be developed through AM, the anisotropic nature of the thermal expansion coefficient needs to be considered more closely. The microstructural CTE was linked to the bulk CTE through a combination of the crystallographic grain orientations and the XRD lattice parameter measurements. A summary of the key values is presented in Table 5.5. Now that that the effect of the key microstructural elements of intermetallics and anisotropy in the titanium-copper system is better understood, prediction methods can be developed and evaluated as discussed in the next chapter to tailor CTE.

Table 5.5. A summary of key 20-500 °C CTE values from microscopic measurements compared to bulk macroscopic measurements. Values with an '' are taken from [99] and are to 600°C, but were used in the EBSD CTE correction..*

	20-500 °C CTE (ppm/°C)							
As Processed	a-axis	c-axis	Volumetric	Bulk Avg	EBSD Corrected Bulk Ave (in-plane)	EBSD Corrected Bulk Ave (vertical)	Bulk Experimental (in-plane)	Bulk Experimental (vertical)
Wrought Titanium	9.55*	10.7*	29.8	9.93	9.98	9.65	9.72	9.48
AM Titanium	-	-	-	-	9.99	9.84	9.36	9.16
$CuTi_2$	14.7	3.16	32.5	10.8	-	10.8	10.4	10.6

Chapter 6

TAILORING THERMAL EXPANSION

Now that the key effects of the microstructure on CTE are better understood, an evaluation of existing thermal expansion models is required so that a functional gradient in the thermal expansion can be designed. For some thermal expansion reference data, the primary prediction technique is empirical, where many data points are collected and linear regression is performed to achieve a best fit linear relationship for the CTE. The disadvantage of empirical methods is the required data needed to make the prediction, which necessitates that many compositions be built and tested. This can be costly and time-consuming, and it may not be feasible to build and test every composition when designing functional gradients as they may not even provide the desired results. Therefore, theoretical prediction models that were developed for multicomponent material design are explored in this chapter.

In Chapter 2, the Rule of Mixtures (ROM), Turner, Kerner, Thomas, and the Hashin-Shtrikman models were presented as the most commonly employed models for CTE estimation with the Kerner model [65] being touted as the most accurate. The ROM is supposed to be the upper bound [65], while the Turner model [65] is the lower bound. The Thomas model [73], [74] was a semi-empirical variant of the ROM that had been shown to accurately predict the CTE of austenitic stainless steel welds containing different levels of ferrite. Additionally, the Hashin-Shtrikman model [75], [76] was also considered as it is supposed to be able to handle dual phase compositions. Once a valid prediction method is determined, the thermal expansion coefficient can be tailored, allowing the design of an additively manufactured functionally graded thermal expansion materials.

In this chapter the initial prediction of CTE for the binary phase alloy will be discussed as the initial knowledge needed to correctly apply the ROM was unknown. Since the $CuTi_2$ intermetallic was tested for the system of interest, a proper ROM is calculated and an evaluation of other CTE estimation models is performed. An alternative way to determine the CTE of unknown intermetallics is presented and compared with experimental results. Then, using the new intermetallic prediction method in combination with the chosen CTE multiphase model an example functionally graded thermal expansion material is determined.

6.1 Initial CTE Prediction

In Chapter 4, a novel method was presented in Figure 4.1 to provide a framework for selecting candidate alloying elements when designing FGMs. The second step was to determine a governing mechanism that could be used to design the tailored gradient, which was initially selected as the ROM to grade the CTE. This CTE estimation technique for multiphase materials was chosen based on the simplicity of the model and the unknown response of an AM binary phase alloy. The ROM sums up the CTE of the constituents (phases) in the system multiplied by their volume as seen in Equation 2.6. A 500^{o}C target temperature was selected, and since CTE values were unavailable for intermetallic phases, only the pure elemental CTE values and volumes could be used for a starting calculation which is referred to here as an elemental ROM_E, with the E subscript indicating that elements were used and not the phase fractions. Metal alloys are more complicated than well-characterized composites as there are both multiphase regions and solid solutions.

For the titanium-copper system, the only known CTE values from the potential phases in the phase diagram, shown in Figure 5.1, were for pure titanium and pure copper. Additionally, the pure titanium, pure copper, and $CuTi_2$ intermetallic phases all have different crystal systems,

affecting the arrangement of atoms and bond strengths. As discussed in Chapter 2, this impacts the thermal expansion behavior of metals. The alpha titanium crystal system is hexagonal close packed, the copper crystal system is face centered cubic, and the $CuTi_2$ intermetallic is tetragonal as shown in Figure 6.1.

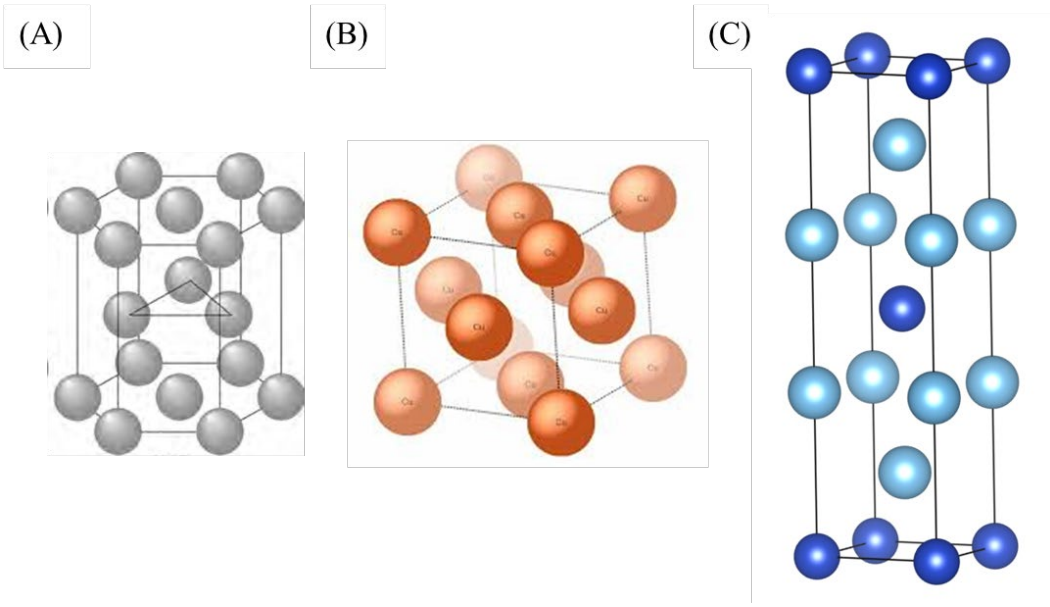

Figure 6.1. The unit cells in the titanium-copper alloy system, with (A) titanium hexagonal close packed [110], (B) copper face centered cubic [111], and (C) the $CuTi_2$ intermetallic on the right (generated using data from [112]).

Unfortunately, combining these elements together creates an issue in properly employing the ROM (which is phase based), as now the thermal expansion of expected phases in the system were initially unknown. While they could be neglected, at 5 at.% copper the microstructure is approximately 17 wt.% $CuTi_2$ intermetallic. Based on available literature data, that phase had an unknown CTE; therefore, only an 'elemental' ROM_E could only be performed—as it currently exists—by using just the pure elemental values, even though for all three initial compositions a two-phase mixture of almost pure titanium and the $CuTi_2$ intermetallic existed simultaneously. Given this caveat to using the ROM_E, the predicted CTEs were calculated by converting the atomic percent mixture of titanium and copper to a weight percent, dividing that number by the

density for each element to get an elemental volume, and then multiplying the volume fraction by the 500°C thermal expansion from [79]. The results are summarized in Table 6.1.

Table 6.1. The elemental ROM_E prediction of the CTE given the pure elemental CTEs for each initial composition.

Mixture	**5 at. % Copper**		**10 at. % Copper**		**15 at. % Copper**	
Element	Copper	Titanium	Copper	Ttianium	Copper	Titanium
Atomic Percent Copper	5	95	10	90	15	85
Weight Percent Copper	6.53	93.47	12.85	87.15	18.98	81.02
Volume of Copper	0.73	20.72	1.43	19.32	2.12	17.96
Volume Fraction	0.03	0.97	0.07	0.93	0.11	0.89
ROM CTE	**9.99**		**10.3**		**10.6**	

After the deposition of each composition was performed and evaluated as described in Chapter 4, an evaluation of the ROM_E could be performed, which is important as the intermetallic data was unavailable at that time. Figure 6.2 shows the CTE results with the ROM_E prediction indicated by the 'x' and the green line representing the reference value for pure titanium. With the exception of the 15 at.% copper case, the ROM_E model consistently over-predicted the CTE by approximately 0.3 ppm/°C (~3% over-prediction) for the as-deposited case and around 0.5 ppm/°C (~5% over-prediction) for the HIPed condition case, which is surprisingly good agreement considering the elemental application of the ROM_E.

Given the relatively decent agreement with the experimental results, the ROM_E was used to predict the thermal expansion for the 33.33 at.% copper composition, which is the $CuTi_2$ intermetallic, and it was calculated to be 11.9 ppm/°C. While it consistently over-predicted before within reason, it became evident that the elemental application of the ROM breaks down as the alloy content is increased and the intermetallic phase fraction becomes a more substantial portion of the microstructure, which is consistent with prior observations. The average CTE of the intermetallic was experimentally measured to be 10.6 ppm/°C at 500 °C, which is 1.3 ppm/°C

lower (~12.2% decrease) than predicted by the ROM_E. As discussed in Chapter 5, the microstructure changes between the as-deposited and HIP, converting more of the alloy to the intermetallic phase, which partially explains the lower value for the HIPed condition.

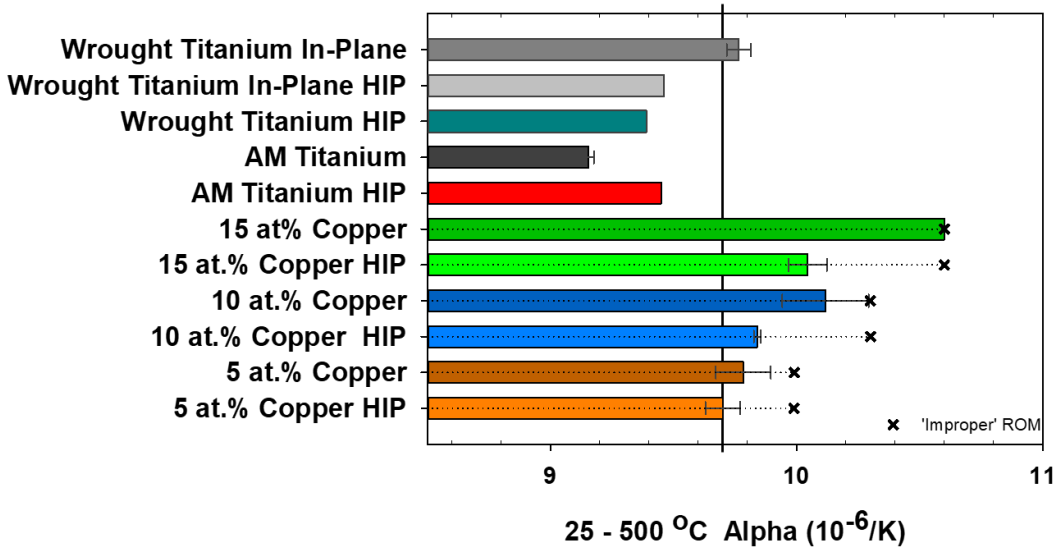

Figure 6.2. The initial thermal expansion results showing where the ROM_E prediction, indicated by the 'x', falls with respect to the experimental measurements. It can be seen that the elemental application of the ROM_E consistently overpredicts the CTE, due to the true CTE value of the intermetallic phase, which is approximately 1.3 ppm/°C lower than what would be predicted by ROM_E.

6.2 Evaluation of Prediction Models

From the literature review, the Rule of Mixtures (ROM), Turner, Kerner, Thomas, and Hashin-Shtrikman models were selected to be considered for predicting the CTE of the blended alloy system as discussed in Chapter 2. While it appears the elemental application of the ROM_E may provide a rough estimate for low solute alloy content mixtures, the predicted CTE could be drastically different depending on the actual value of the intermetallic phase CTE. In thermal barrier coatings, a CTE difference of only 1 ppm/°C can cause failure, indicating the importance of getting as accurate of a multiphase prediction as possible [78]. Since the CTE of the cast $CuTi_2$

intermetallic was determined experimentally in Chapter 4, proper prediction models can be run using $CuTi_2$ intermetallic and the phase volume fractions. However, for the other multiphase CTE prediction models, a similar issue exists where the Kerner, Turner, and Hashin-Shtrikman models require more data, like bulk and shear moduli, for the intermetallic phase, which currently does not exist. Therefore, only the phase-based ROM and Thomas model could be properly evaluated.

By using the experimentally found 25-500ºC value for the $CuTi_2$ intermetallic, the results from the phase-based application of the ROM (see Equation 2.6) and Thomas models are given in Table 6.2 and shown graphically in Figure 6.3. By using the phase fraction volumes and associated CTEs, both the ROM and Thomas model provide excellent predictions of the AM titanium-copper system CTE in the HIPed condition, only deviating by approximately 0.1 ppm/ºC and is within the experimental error of the CTE measurement.

The agreement with the HIPed condition is not surprising as this condition provides closer to equilibrium microstructure, and the equilibrium phase fractions are used since this is a prediction method. Similarly, the discrepancy in the as-deposited 15 at.% case is due to the material being in a non-equilibrium state with excess pure copper trapped in the microstructure that converts to the $CuTi_2$ intermetallic upon any heat treatment. Given the overall consistency between predictions, the phase-based, properly applied ROM proves to be the easiest and equally valid prediction method for estimating multiphase alloy CTEs when CTE values of the intermetallic compounds are known. The ROM has now been shown to be an accurate prediction model for multiphase AM elemental alloys with high alloy content, given the single phase CTEs are known.

Table 6.2. CTE model predictions compared with the experimental values. Both the ROM and Thomas model provide excellent agreement with the experimental HIP results. Given the nearly equivalent values, the phase-based ROM proved to be the simplest and most accurate prediction method if the intermetallic CTE values are known.

(ppm/oC)	Experimental		Prediction	
Sample	As Deposited	HIP	ROM	Thomas
Ti-5Cu	9.78	9.70	9.81	9.80
Ti-10Cu	10.1	9.84	9.94	9.93
Ti-15Cu	10.6	10.0	10.1	10.0

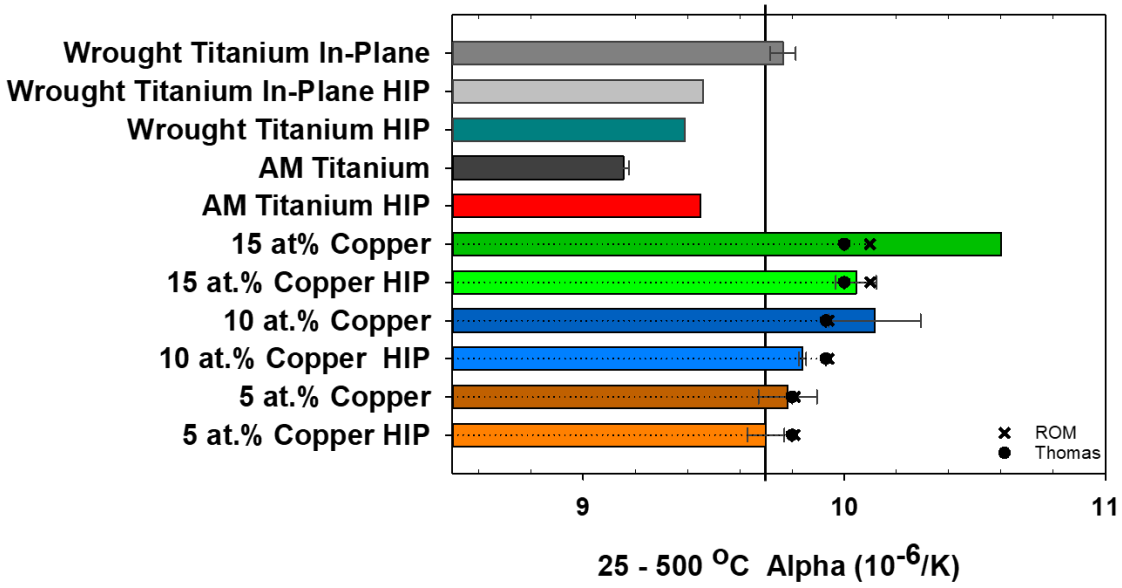

Figure 6.3. Both the ROM and Thomas model CTE predictions indicated by 'x' and '.' respectively are compared with the experimental dilatometry values. Both the ROM and Thomas model provide excellent agreement with the experimental HIP results due to the material being closer to the equilibrium state as the phase fractions were used for the calculation.

6.3 Intermetallic Thermal Expansion[1]

Now that the phase-based ROM has demonstrated a much better prediction of the CTE for a multiphase alloy than the ROM_E, the need arises to estimate the intermetallic values for

[1] Section 6.3 was adapted from a working paper titled 'Tailoring the CTE of Additively Manufactured Titanium' authored by S.R. Hilburn and W. Chen

broader applications. For example, if the value for the titanium-copper system CTE needed to exceed the $CuTi_2$ value of 10.6 ppm/ ^oC, then the composition would have to increase into the next two-phase field consisting of the CuTi and $CuTi_2$ intermetallics. For that new two-phase field, the CuTi intermetallic CTE is unknown; therefore, the ability to estimate the CTE of that intermetallic compound is necessary to avoid additional experimentation. Beyond the titanium-copper system, there are many other alloy systems where the material properties, like the CTE, for the intermetallics are unknown. Since the CTE is an intrinsic material property that is based on atomic bonding, computational materials science tools were investigated as a potential route to model the unit cell atomically and estimate the CTE for a given intermetallic.

6.3.1 Computational Materials Science

Classic molecular dynamics (MD) [113], ab-initio MD [113], and density functional theory (DFT) [113] were considered as potential routes to explore the intermetallics on an atomistic level. After an initial investigation, DFT simulations were chosen as they are not as computational expensive as ab-initio MD, and are considerably more accurate than classic MD. DFT is robust electronic structure calculations and is self-consistent [114], which explains the popularity of its use. Moreover, free energies and their derivatives are calculated self-consistently in DFT simulations, giving rise to remarkably accurate predictions of intrinsic materials properties. In recent years, the calculations of vibrational properties of crystals by first-principles simulations have become feasible within reasonable computational cost [115].

For example, thermal expansion coefficients of semiconductors and metals can be easily calculated from first-principles calculations, achieving reasonable agreement to experimental measurement [116], [117]. It has been shown previously that thermal expansion coefficients can be obtained from classical MD simulations, with the caveat that the prediction accuracy is limited

by the quality of the interatomic potential, which has to be known in advance and often lacks transferability between different phases or systems [118]. Therefore, first-principle DFT simulations are developed and employed to determine the anisotropic linear thermal expansion coefficients of the intermetallic compounds $CuTi_2$ and CuTi. More on the DFT theory, background, and computational details are given in Appendix B.

6.3.2 DFT Results

The computation of the thermal expansion coefficients, as well as the corresponding vibrational properties of CuTi and $CuTi_2$ compounds, are presented in this section. The crystal structures of the $CuTi_2$ and CuTi compounds considered in this work are presented in Figure 6.4.

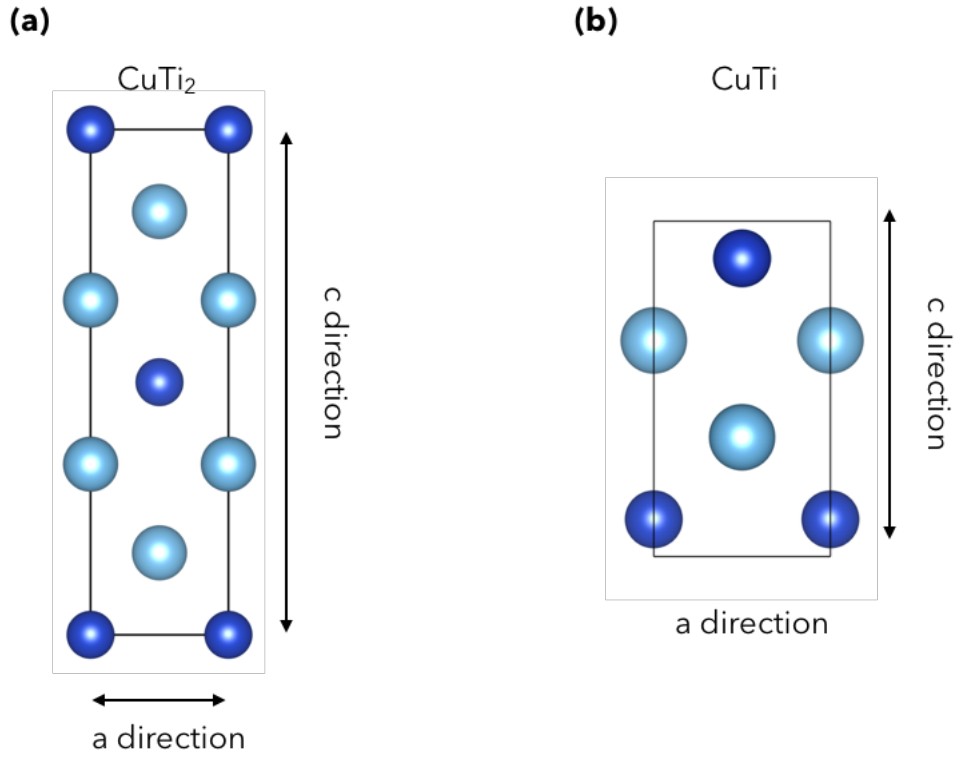

Figure 6.4. 2D crystal structure representation of $CuTi_2$ and CuTi unit cells used in the DFT calculations. The space groups of $CuTi_2$ considered in this work is I4/mmm, and the space group of CuTi is P4/nmm, each having unique a-axis and c-axis CTEs.

The DFT calculated elastic stiffness and compliance matrix of these two intermetallic compounds are reported in Table 6.3 and Table 6.4 in a compact representation of non-zero cells in a symmetric six by six tensor. The values achieved are in correspondence with previous reported first-principle values from the Materials Project [112].

Table 6.3. Elastic compliance and stiffness tensor of CuTi2 compound.

ij	11	12	13	33	14	16
C_{ij} (GPa)	180.5	60.1	96.9	157.1	82.5	44.6
S_{ij} (10^{-12} Pa^{-1})	8.2	-0.01	-5.1	12.6	12.1	22.3

Table 6.4. Elastic compliance and stiffness tensor of CuTi compound.

ij	11	12	13	33	14	16
C_{ij} (GPa)	181.2	104.9	106.1	188.1	87.3	87.8
S_{ij} (10^{-12} Pa^{-1})	9.5	-3.5	-3.4	9.1	11.4	11.4

The most fundamental vibrational properties of compounds considered in this work are the vibrational spectrums. In Figure 6.5, the phonon dispersion curves of $CuTi_2$ and CuTi are plotted along high symmetry directions of the Brillouin zone (reciprocal lattice space) [119]. No imaginary phonon frequencies are observed, implying that the two systems are the most stable phases predicted by the first-principle simulations without a strong anharmonic effect.

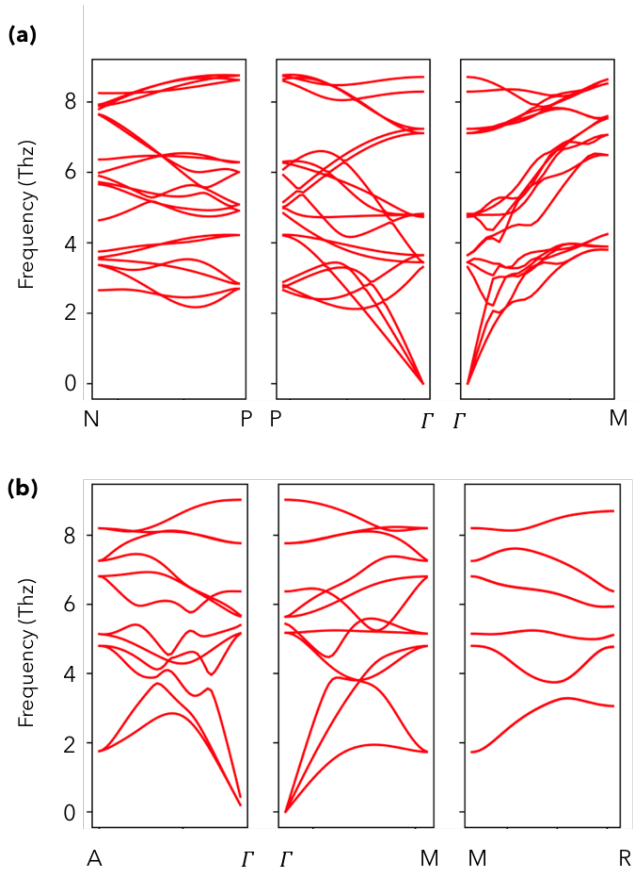

Figure 6.5. Phonon dispersion relations of (a) CuTi2 and (b) CuTi compound from their conventional unit cells.

To calculate the linear thermal expansion coefficients, the unit cell crystals are strained along a and c directions by ± 0.03 angstroms, and the Grüneisen parameters (relating change in frequency to change in volume) are computed for each condition [43]. Based on the force constant matrices of deformed crystals, the resulting mode Grüneisen parameters are extrapolated on a $60 \times 60 \times 60$ q-point mesh grid. These results are summarized in Figure 6.6, presenting the phonon modes due to the volume change.

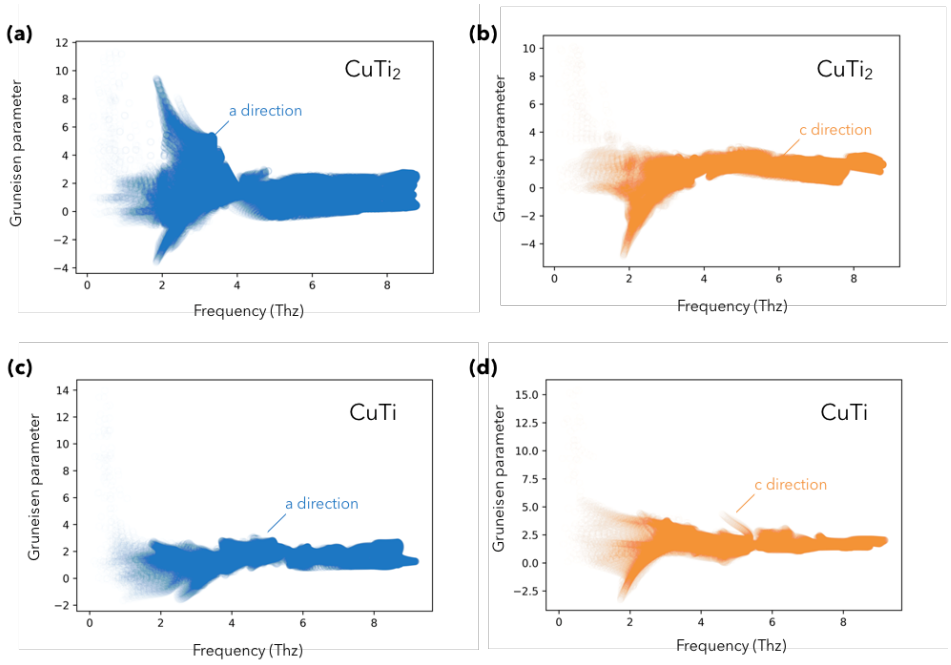

Figure 6.6 Mode Grüneisen parameters of $CuTi_2$ and CuTi along two crystal directions.

Finally, based on the DFT simulations, the linear thermal expansion coefficients of the $CuTi_2$ and CuTi intermetallic compounds can be calculated. The results are presented in Table 6.5 and plotted in Figure 6.7. It is noted that in $CuTi_2$ compound, the linear thermal expansion coefficient along the 'a' direction is significantly larger than that of 'c' direction, showing a high degree of anisotropy. DFT simulated CTE values for $CuTi_2$ fall within reasonable limits of the XRD lattice parameter estimate of the $CuTi_2$ intermetallic reported in Chapter 5 as 14.7 ppm/^{o}C in 'a', 3.2 ppm/^{o}C in 'c', and a β of 32.7 ppm/^{o}C, translating into a 10.9 ppm/^{o}C bulk average. When comparing the bulk average CTE, the DFT results deviate approximately 4.6% from the lattice parameter experimental value, and 7.5% from the bulk dilatometry value. While the $CuTi_2$ intermetallic shows a high degree of anisotropy between the 'a' and 'c' thermal expansions, it is not observed in the CuTi compound. By using the volumetric CTE converted into a bulk average CTE, the values can be used in the ROM prediction model of the CTE for the required next two-phase region. This technique can then be used to tailor the CTE in a FGM and is discussed next.

Table 6.5. The thermal expansion results for the intermetallic compounds $CuTi_2$ and CuTi from DFT calculations.

	Temperature	a-axis CTE	c-axis CTE	Volumetric CTE	Bulk CTE Average
Intermetallic	°C	ppm/°C	ppm/°C	ppm/°C	ppm/°C
$CuTi_2$	20	14.8	2.30	32.0	10.7
	500	15.5	3.25	34.2	11.4
CuTi	20	10.1	12.3	32.5	10.8
	500	10.8	13.1	34.8	11.6

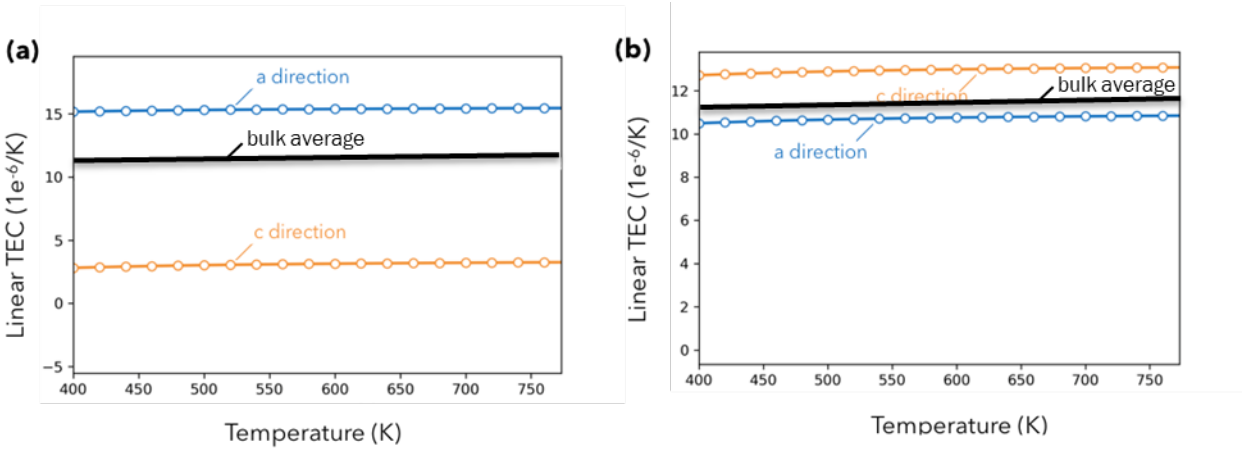

Figure 6.7. Anisotropic linear thermal expansion coefficients of (a) CuTi2 and (b) CuTi compounds calculated from DFT first-principles calculations.

6.4 Tailoring Thermal Expansion

By estimating the unknown CTE for intermetallic compounds with DFT, the thermal expansion can now be tailored in an FGM compositional alloy. First, the desired CTE gradient should be defined, then once the candidate alloy systems are selected from the method in Figure 4.1 the intermetallic CTEs can be estimated by using the average bulk CTE calculated from the volumetric CTE predicted from DFT. With this value, a reverse ROM can be performed where the phase volumes are computed from the desired CTE value, which can then be converted into an elemental composition. Given the significance of a 1 ppm/ºC mismatch in CTE as discussed in

Section 2.6, a target grading value of 0.5 ppm/ºC was selected to minimize the stresses between target compositions while providing a gradual change in CTE.

A summary of the key thermal expansion data for designing the final FGM is summarized in Table 6.6. Given the DFT predicted 20-500ºC bulk average CTE for the 50 at.% intermetaillic is 11.6 ppm/ºC an example FGM is designed from this value down to AM titanium with an approximate ~0.5 ppm/oC step between compositions. Equilibrium phase fractions are used since it was determined that the post-HIP material only deviated from equilibrium by ~5% and the ROM estimates were reasonably accurate using the equilibrium phase fractions. Grade 1 AM titanium (composition 1) has an experimentally measured CTE of 9.45. Therefore five total layers are required to grade the CTE to the CuTi value of 11.6 ppm/ºC as shown in Figure 6.8 and Table 6.7.

Table 6.6. A summary of the key thermal expansion data for designing the final FGM structure. The reference data '' was taken from [79], the AM titanium value was experimentally obtained in the HIPed condition, $CuTi_2$ was obtained from experiments on the cast bar, and CuTi was predicted from DFT.*

Material	20 - 500°C CTE
Reference Ti	9.7*
Reference Cu	18.3*
AM Titanium	9.45
$CuTi_2$	10.6
CuTi	11.6

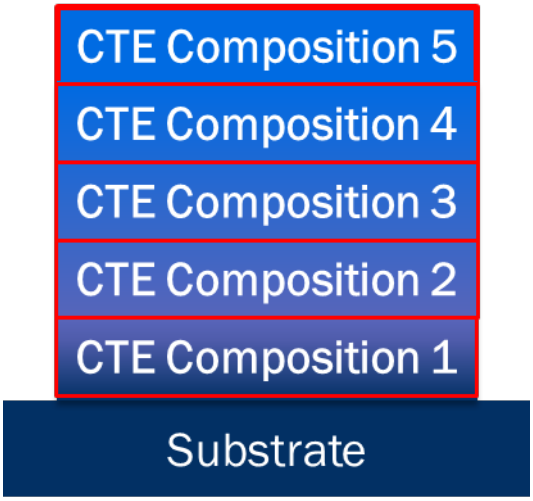

Figure 6.8. The final graded CTE compositional structure needed to make a linear functional gradient in CTE.

Table 6.7. The final designed gradient in ~0.5 ppm/oC increments from HIPed AM titanium (composition 1) to the CuTi intermetallic (composition 5). Each composition in-between was solved for using the ROM and the lever rule.

Composition	CTE	wt.% Copper
1	9.45	0.00
2	10.0	22.3
3	10.5	38.5
4	11.0	42.4
5	11.6	57.0

For composition 4 the desired CTE value higher than the experimental value for the $CuTi_2$ intermetallic of 10.6 ppm/^{o}C, then the next two-phase region, between the $CuTi_2$ and CuTi intermetallics, will contain the required composition. A two-term Rule of Mixtures is setup with those two phases, and a solver can be used to find the phase volumes needed to achieve the desired value of 11.0 ppm/^{o}C. Once converted into a weight percent, the *lever rule* [120] can be solved to determine the needed composition, which was calculated to be 42.4 wt.% copper in this example. Then the final composition (composition 5) of 57.0 wt.% copper was needed to achieve the 50 at.% CuTi intermetallic value of 11.6 ppm/^{o}C. This method shows the ability to tailor the thermal expansion once the intermetallic estimates are known.

Fabricating the newly designed FGM created to tailor the thermal expansion performance is the last major challenge. Given the layer-by-layer nature of AM, it is feasible to change the composition as needed between layers; however, as discussed in Section 1.4 a diffusion grading effect occurs between layers of different compositions and further diffusion will occur during HIP. In order to compensate for the dilution at the layer interface, multiple layers will be deposited of each composition. It is proposed that 3 layers should be sufficient to allow for a significant portion of each desired composition to be present (see Figure 6.9). The part of the top and bottom layer that is diluted should create a linear compositional gradient between the two compositions which could have an impact on the final CTE design as a linear CTE gradient is created by a nonlinear composition gradient (shown in Table 6.7). Future work is needed to investigate and address the complications at the layer interfaces where the composition is changed.

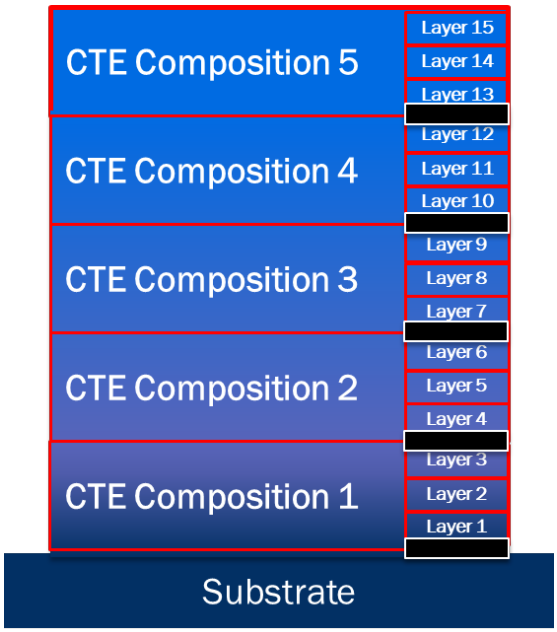

Figure 6.9. Three layers of each composition are used to accommodate the dilution at the interfaces (shown in black). Depending on the substrate material potentially only two layers are needed and for the final composition only two layers are needed although 3 are shown.

6.5 Summary

It has been demonstrated that if the CTEs are known for each phase encountered in the alloy system, then the CTE can be tailored using proper application of the Rule of Mixtures. If phase CTEs are not known for dilute alloy mixtures, an elemental application of the ROM_E using pure elemental compositions appears to provide a rough estimation of the system. When designing FGMs that utilize multiphase materials, a small difference in the CTE could lead to build failures, requiring better prediction methods. While other multicomponent material models are potentially more accurate, they cannot be utilized for phases with unknown material properties. Using the experimentally measured CTE of the $CuTi_2$ intermetallic, the ROM and Thomas models could be evaluated. Both models provided equivalent results with the simplest model being the ROM, which was selected as the best prediction tool given the known material properties.

Since the CTE for the intermetallic phases is one of the intrinsic material properties that is unknown across many alloy systems, it was demonstrated that DFT can provide an estimate for the CTE of the intermetallic phase, which offers a better prediction than using the pure elements and applying the elemental ROM_E model. The DFT estimates for the $CuTi_2$ intermetallic align with both bulk and lattice experiments. These CTE estimates now allow for the prediction of the multiphase alloy CTE using a phase-based ROM and subsequently the ability to determine the volume fractions required to achieve a desired CTE.

With ability to tailor the CTE, novel FGM designs can be generated where the CTE is functional graded by changing the composition in an alloy system. An example was given where the CTE of titanium was able to be increased incrementally by ~0.5 ppm/^{o}C through compositional grading with copper, from the AM titanium value of 9.45 ppm/^{o}C to 11.6 ppm/^{o}C with the ability to add more intermediate layers as desired. This example FGM linearly grades the

CTE through a non-linear change in composition. Additionally, the opportunity now exists to fix build issues arising from CTE mismatch in FGMs by tailoring the CTE. These and other contributions from the research are discussed in the next chapter along with future work.

Chapter 7

CONCLUSIONS, CONTRIBUTIONS, AND FUTURE WORK

A synopsis of the research performed is presented in this chapter. The research summary is reviewed first, detailing what was done. Then contributions from the research are discussed, focusing on both practice and theory. Finally, limitations of this research effort are given and ideas into future work are considered.

7.1 Summary of the Research

Many engineering systems require the assembly or joining of dissimilar materials to achieve desired system performance. Since these dissimilar metals have different thermal expansion coefficients, the metals will expand or contract at different rates with temperature changes, creating stress at their interface. The internal stress generated can either cause distortion of the component or failure at the joint, and strategies for mitigating the CTE mismatch in these systems is needed. With the emergence of additive manufacturing (AM) enabling novel material design, it was proposed that a functional graded material (FGM) could be designed to minimize the thermal expansion mismatch between two dissimilar metals by grading the material's CTE through compositional changes.

Additively manufactured compositional FGMs have their own set challenges that can lead to failure of the resulting graded structure. Three key failure mechanisms were identified from the available literature: (1) solidification cracking, (2) chemical incompatibilities, and (3) CTE mismatch. Solidification cracking occurs in material systems with a large solidification range, where the metal contracts upon solidification, and a shortage of the liquid occurs, leading

to microcracks within the material during additive manufacturing. Chemical incompatibilities like immiscibility can prevent good mixing of the alloy and the formation of intermetallic phases, which are typically avoided as their brittle nature can cause build failure. Finally, a thermal expansion mismatch can cause cracking in the build. This is the same issue that was presented on an aerospace application macroscopic scale, now on a microscopic level. If CTE mismatch can be addressed at the interfaces microscopically, then the larger macroscopic issue can be solved at the macroscopic level using a functional gradient.

Currently, the primary way to design FGMs employs CALPHAD methods, generating phase diagrams to avoid deleterious phases, and running Scheil partitioning calculations to examine the solidification range. However, the major challenge with this approach is that thermodynamic data is only readily available for commonly used alloys and is limited for many elemental combinations, especially at high solute alloy content. Moreover, the common ‘rule of thumb’ to avoid brittle intermetallics is difficult to assess as there are not currently any available techniques to evaluate the ductility of the intermetallic phases without experimentation, which leads to researchers attempting to avoid intermetallic phases altogether.

A review of thermal expansion explored the microscopic and macroscopic intricacies of the CTE while revealing issues with how thermal expansion data is catalogued. Reference books present thermal expansion values that are currently used for engineering designs without expressing the error or variance of that measurement. Furthermore, since the CTE is a second-ranked tensor, the thermal expansion for non-cubic crystal system metals are anisotropic, with no indication of this anisotropy in most references.

While anisotropy can be ignored in polycrystalline metals that have randomly oriented crystals and homogenous distribution of grains, processing techniques for most metals provide microstructures that do not completely satisfy these requirements. It was determined from both hot rolled wrought grade 2 titanium plate and from an AM grade 1 titanium block that not only

does anisotropy clearly exist based on the sample orientation, but also both processing methods produced crystal orientations that led to a lower value in the vertical direction. Ultimately, the crystallographic texture, or the tendency for one orientation to be preferentially produced when processing the material, generates the observed anisotropy in the system. In this work, the anisotropy was observed to be between the in-plane and vertical samples.

Contrary to the popular FGM design method of attempting to get from Alloy A with some desired property to Alloy B with a different desired property, elemental blending was employed to design the FGM. A novel method was created to guide the elemental FGM design process and was refined through attempting to increase the thermal expansion of titanium. Copper and silver were chosen as candidate alloying elements for titanium and different alloy compositions were deposited. An investigation into the key microstructural elements of intermetallic formation and anisotropy was performed to determine what features provided the most significant impact on the CTE. Utilizing the knowledge gained from these assessments a new framework for functionally grading the CTE using composition was developed. An example FGM was presented increasing the CTE of titanium linearly from 9.45 ppm/^{o}C to 11.6 ppm/^{o}C in approximate 0.5 ppm/^{o}C increments.

7.2 Contributions from the Research

7.2.1 In-Practice

- Anisotropy was observed in the CTE measurements between vertical and in-plane samples for both wrought and AM titanium. The texture created during processing and the anisotropic nature of the alpha titanium hexagonal close packed (HCP) crystal led to the observed orientation difference in CTE.

- A ROM was initially selected as the governing mechanism for the CTE, but due to the lack of data for intermetallic phases, only an elemental ROM_E could be used. Silver and copper were chosen as candidate alloying elements to add to pure titanium in an attempt to raise the alloy system's CTE. Other than binary phase diagrams, CALPHAD data was unavailable to preform additional analysis. Both alloy systems were successfully deposited without cracking.
- Initial alloying experiments showed that by adding 5 at.% copper to titanium, the vertical orientation CTE could be increased up to that of the in-plane wrought values. The vertical orientation was the focus of measurements in this investigation as the designed gradient is intended to be generated in the vertical direction. Adding additional copper content further increased the thermal expansion beyond that of wrought commercially pure titanium, proving the validity of elemental blending as a viable method to generate FGMs with AM.
- From the as-deposited results, it was determined that the material was microstructurally changing at during the 500°C test, indicating the non-equilibrium nature of deposited material. The AM process, specifically laser-based directed energy deposition (DED), creates complex fine-featured microstructures containing multiple phases, complicating the ability to isolate which features have the greatest effect on the CTE. Build inhomogeneities due to density differences, partitioning, and poor parameter development, can potentially impact the CTE. Post-HIP CTE evaluation showed a recovery of the CTE in the 5 at.% silver composition, indicating that a loss of CTE due to build defects can be recovered with HIP.
- The phase fractions in the as-deposited material were different than what was expected from the equilibrium phase diagrams. For the titanium-copper system,

XRD analysis indicated that roughly 6 wt.% of the microstructure converted to the intermetallic $CuTi_2$ after the initial 500ºC CTE test, explaining the lower thermal expansion values observed after heat treatment. Due to the strong influence of the intermetallic phase on the CTE, an investigation into the unknown value for the $CuTi_2$ intermetallic was performed, and the average value was determined to be 10.6 ppm/ºC.

- In this work, multiple intermetallics created in both the silver and copper alloyed titanium were not brittle in nature and did not cause build failure.
- The elemental ROM_E systematically over-predicted the CTE for the HIPed material, but it could be employed as a rough estimate for as-deposited structures or in dilute alloy content systems. It was demonstrated that this ROM_E approach breaks down with increasing composition, as the second phase with an unknown CTE becomes a significant portion of the microstructure.

7.2.2 Theory

- Due to the observed anisotropy in the pure titanium measurements, an additional literature review revealed that this was a well-documented phenomenon that seems to have been institutionally lost over the last 40 years. Furthermore, significant disparities existed between the reference data for the individual lattice expansions in the a-axis and c-axis, not only on the CTE values, but also on which axis expands more at elevated temperatures. While the XRD evaluation of the lattice parameters can be a difficult test to perform accurately, this is a significant gap in the literature. The crystallographic texture created by the

material processing directly impacted the bulk CTE values due to the anisotropic behavior of both titanium and the $CuTi_2$ intermetallic.

- A code was created using MATLAB and MTEX EBSD analysis software that allows for the calculation of the expected thermal expansion in a given direction, given the input of the reference CTE tensor and EBSD orientation data. The results accounted for the difference between wrought and AM titanium. While this technique can determine the CTE based on the observed microstructure, it is unable to aid in the prediction of unknown microstructures. Nevertheless, the ability to link the microstructure to the observed bulk performance is critical in understanding process-structure-property relationships.
- In order to tailor the CTE, an accurate prediction of the CTE is required and subsequent prediction of the intermetallics encountered are required. Multiple prediction models were considered, but only the ROM and the Thomas model could be applied properly given the lack of material property data for the intermetallic phases. Both models provided excellent agreement with experimental results, only differing in the prediction by approximately 0.1 ppm/^{o}C (1%) at the highest composition. Given their equivalence, the standard ROM was chosen as the best model due to its simplicity. These models are only accurate if the CTE data is known for each phase in the microstructure.
- Realistically, physical experiments cannot be run on every candidate material system's intermetallics, which prompted an investigation into potential prediction methods for a given intermetallic CTE. Due to the CTE being an intrinsic material property based on the bond energy well and phonon motion in the system, computational materials science had potential to provide a CTE prediction. Specifically, DFT was chosen as the appropriate computational

method, and the $CuTi_2$ system was simulated to compare with experimental results that had already been completed. From the DFT calculation, it was determined that the average bulk CTE was 11.4 ppm/^{o}C which was 0.8 ppm/^{o}C (7.5%) higher than the experimental average. While this technique provided a reasonable CTE prediction, experiments are required to be able to design a final gradient with 0.5 ppm/^{o}C steps.

- DFT determined the unknown CuTi intermetallic to be 11.6 ppm/^{o}C, which was only slightly higher than the $CuTi_2$ intermetallic estimation of 11.4 6 ppm/^{o}C. Using the DFT prediction for the CTE of CuTi and experimental results for the CTE of $CuTi_2$, an example tailored FGM was calculated with the ROM starting with AM titanium at 9.45 ppm/^{o}C by ~ 0.5 ppm/^{o}C up to 11.6 ppm/^{o}C. The final compositional gradient required non-linear scaling to achieve the designed linear CTE gradient. The theorized five-layer final composition was presented.
- Ultimately, a novel landscape was presented using fundamental material science to tailor the CTE for both FGMs and multicomponent systems. The most significant challenge is predicting the unknown CTE for an intermetallic compound to a higher degree of accuracy due to the anharmonic contributions that are hard to model. Once the CTEs are known for the phases in the system a simple ROM provides an excellent prediction of the CTE providing the ability to tailor the CTE and design FGMs.

7.3 Limitations and Future Work

A few key limitations exist in this research effort with the most obvious one being the lack of intermetallic data for a proper phase-based ROM calculation. While it was shown that

DFT can predict these values, a set of DFT simulations take approximately a week to complete and the results may not be quite accurate enough to perform the final graded structure without experimentation. However, the ability to survey multiple intermetallics through DFT provides a significant step forward. Another limitation is the inconsistencies found for the anisotropic CTE tensor of titanium, with different sources contradicting each other. A final key limitation is the ability to develop quality processing parameter sets to build structures with minimal defects across a graded alloy. The time required to perform the process development for each composition will decrease with more experience, but the need still exists to generate individual parameter sets for multiple compositions in a FGM.

In the future, higher copper concentrations of the titanium-copper system should be investigated to determine the agreement with the DFT predicted 50 at. % intermetallic. Another alloy system should also be investigated to ensure the robustness of this method across multiple alloy systems. Finally, the designed FGM should be built, verifying the ROM predictions of different compositions and the success of the combined gradient. Separately, a more thorough XRD investigation of the pure titanium lattice parameters is needed at multiple temperatures to correct and augment the published literature.

References

[1] E. Sideridis and G. C. Papanicolaou, “A theoretical model for the prediction of thermal expansion behaviour of particulate composites,” *Rheologica Acta*, vol. 27, no. 6, pp. 608–616, Nov. 1988, doi: 10.1007/BF01337456.

[2] V. Nandivada, “ADHESIVES: The Importance of CTE for Assembly Reliability,” *Medical Design Briefs*, Oct. 01, 2017. https://www.medicaldesignbriefs.com/component/content/article/mdb/features/articles/27726 (accessed Jul. 04, 2019).

[3] M. B. Uday, M. N. Ahmad-Fauzi, A. M. Noor, and S. Rajoo, “Current Issues and Problems in the Joining of Ceramic to Metal,” in *Joining Technologies*, M. Ishak, Ed. InTech, 2016.

[4] S. S. Milward, H. Swygart, L. Eccles, S. G. R. Brown, and N. P. Lavery, “Controlling Thermal Expansion with Lattice Structures Using Laser Powder Bed Fusion,” Aug. 2017, pp. 2139–2147, Accessed: Dec. 07, 2017. [Online]. Available: http://sffsymposium.engr.utexas.edu/sites/default/files/2017/Manuscripts/ControllingThermalExpansionwithLatticeStructu.pdf.

[5] D. M. Jacobson and G. Humpston, *Principles of Brazing*. ASM International, 2005.

[6] P. Kah, R. Suoranta, J. Martikainen, and C. Magnus, “TECHNIQUES FOR JOINING DISSIMILAR MATERIALS: METALS AND POLYMERS,” p. 13.

[7] T. Nishino, M. Kotera, and Y. Sugiura, “Residual stress of particulate polymer composites with reduced thermal expansion,” *Journal of Physics: Conference Series*, vol. 184, p. 012026, Aug. 2009, doi: 10.1088/1742-6596/184/1/012026.

[8] S-Bond Technologies, “Dissimilar-Materials-Joining.pdf,” *S-Bond Technologies, LLC*, May 14, 2013. https://www.s-bond.com/assets/Documents/Dissimilar-Materials-Joining.pdf (accessed Jul. 04, 2019).

[9] S. Jin and H. Mavoori, “Low-thermal-expansion copper composites via negative CTE metallic elements,” *JOM*, vol. 50, no. 6, pp. 70–72, Jun. 1998, doi: 10.1007/s11837-998-0133-9.

[10] Altair Technologies, “Thermal Expansion and Brazing,” 2017. http://www.altairusa.com/thermal-expansion-and-brazing/ (accessed Jul. 04, 2019).

[11] A. Levy, “Thermal Residual Stresses in Ceramic-to-Metal Brazed Joints,” *Journal of the American Ceramic Society*, vol. 74, no. 9, pp. 2141–2147, Sep. 1991, doi: 10.1111/j.1151-2916.1991.tb08273.x.

[12] T. Newswander and R. A. Paquin, “3 Materials for Optical Systems,” in *Handbook of Optomechanical Engineering*, CRC Press, 2017, p. 39.

[13] G. F. Abdelal, N. Abuelfoutouh, and A. H. Gad, *Finite element analysis for satellite structures*. London: Springer, 2013.

[14] M. M. Finckenor, “6. Materials for Spacecraft,” in *Aerospace Materials and Applications*, B. N. Bhat, Ed. Reston ,VA: American Institute of Aeronautics and Astronautics, Inc., 2018.

[15] E. A. Brandes, G. B. Brook, and C. J. Smithells, Eds., *Smithells metals reference book*, 7th ed / edited by E.A. Brandes and G.B. Brook. Oxford ; Boston: Butterworth-Heinemann, 1998.

[16] Vicky Hamilton, “The OSIRIS-REx Thermal Emission Spectrometer (OTES) – Our Heat Sensor and Mineral Mapper,” *Life on the Asteroid Frontier*, May 18, 2014.

https://dslauretta.com/2014/05/18/the-osiris-rex-thermal-emission-spectrometer-otes-our-heat-sensor-and-mineral-mapper/ (accessed Jul. 04, 2019).

[17] P. R. Yoder, "Chapter 37 MOUNTING OPTICAL COMPONENTS," in *Handbook of Optics*, Second Edition., vol. I Fundametnals, Techniques, and Design, McGraw-Hill, 1995, p. 26.

[18] M. S. Domack and J. M. Baughman, "Development of nickel-titanium graded composition components," *Rapid Prototyping Journal*, vol. 11, no. 1, pp. 41–51, Feb. 2005, doi: 10.1108/13552540510573383.

[19] L. D. Bobbio *et al.*, "Additive manufacturing of a functionally graded material from Ti-6Al-4V to Invar: Experimental characterization and thermodynamic calculations," *Acta Materialia*, vol. 127, pp. 133–142, Apr. 2017, doi: 10.1016/j.actamat.2016.12.070.

[20] B. E. Carroll *et al.*, "Functionally graded material of 304L stainless steel and inconel 625 fabricated by directed energy deposition: Characterization and thermodynamic modeling," *Acta Materialia*, vol. 108, pp. 46–54, Apr. 2016, doi: 10.1016/j.actamat.2016.02.019.

[21] T. DebRoy *et al.*, "Additive manufacturing of metallic components – Process, structure and properties," *Progress in Materials Science*, vol. 92, pp. 112–224, Mar. 2018, doi: 10.1016/j.pmatsci.2017.10.001.

[22] D. C. Hofmann *et al.*, "Developing Gradient Metal Alloys through Radial Deposition Additive Manufacturing," *Scientific Reports*, vol. 4, no. 1, May 2015, doi: 10.1038/srep05357.

[23] D. C. Hofmann *et al.*, "Compositionally graded metals: A new frontier of additive manufacturing," *Journal of Materials Research*, vol. 29, no. 17, pp. 1899–1910, Sep. 2014, doi: 10.1557/jmr.2014.208.

[24] R. M. Mahamood and E. T. Akinlabi, "Laser metal deposition of functionally graded Ti6Al4V/TiC," *Materials & Design*, vol. 84, pp. 402–410, Nov. 2015, doi: 10.1016/j.matdes.2015.06.135.

[25] A. Reichardt, "Additive Manufacturing of Metal-based Functionally Graded Materials," UC Berkeley, Dissertation, 2017.

[26] M. Soodi, S. H. Masood, and M. Brandt, "Tensile strength of functionally graded and wafer layered structures produced by direct metal deposition," *Rapid Prototyping Journal*, vol. 20, no. 5, pp. 360–368, Aug. 2014, doi: 10.1108/RPJ-02-2013-0014.

[27] N. Sridharan *et al.*, "Design, Fabrication, and Characterization of Graded Transition Joints," *WELDING JOURNAL*, vol. 96, no. 8, pp. 295S–306S, 2017.

[28] C. H. Zhang, H. Zhang, C. L. Wu, S. Zhang, Z. L. Sun, and S. Y. Dong, "Multi-layer functional graded stainless steel fabricated by laser melting deposition," *Vacuum*, vol. 141, pp. 181–187, Jul. 2017, doi: 10.1016/j.vacuum.2017.04.020.

[29] J. S. Zuback, T. A. Palmer, and T. DebRoy, "Additive manufacturing of functionally graded transition joints between ferritic and austenitic alloys," *Journal of Alloys and Compounds*, vol. 770, pp. 995–1003, Jan. 2019, doi: 10.1016/j.jallcom.2018.08.197.

[30] P. C. Collins, R. Banerjee, S. Banerjee, and H. L. Fraser, "Laser deposition of compositionally graded titanium–vanadium and titanium–molybdenum alloys," *Materials Science and Engineering: A*, vol. 352, no. 1–2, pp. 118–128, Jul. 2003, doi: 10.1016/S0921-5093(02)00909-7.

[31] C. Shen, Z. Pan, D. Cuiuri, J. Roberts, and H. Li, "Fabrication of Fe-FeAl Functionally Graded Material Using the Wire-Arc Additive Manufacturing Process," *Metallurgical and Materials Transactions B*, vol. 47, no. 1, pp. 763–772, Feb. 2016, doi: 10.1007/s11663-015-0509-5.

[32] U. Savitha, G. Jagan Reddy, A. Venkataramana, A. Sambasiva Rao, A. A. Gokhale, and M. Sundararaman, "Chemical analysis, structure and mechanical properties of discrete and

compositionally graded SS316–IN625 dual materials," *Materials Science and Engineering: A*, vol. 647, pp. 344–352, Oct. 2015, doi: 10.1016/j.msea.2015.09.001.
[33] P. Muller, P. Mognol, and J.-Y. Hascoet, "Modeling and control of a direct laser powder deposition process for Functionally Graded Materials (FGM) parts manufacturing," *Journal of Materials Processing Technology*, vol. 213, no. 5, pp. 685–692, May 2013, doi: 10.1016/j.jmatprotec.2012.11.020.
[34] L. E. Murr *et al.*, "Characterization of titanium aluminide alloy components fabricated by additive manufacturing using electron beam melting," *Acta Materialia*, vol. 58, no. 5, pp. 1887–1894, Mar. 2010, doi: 10.1016/j.actamat.2009.11.032.
[35] S. Kou, *Welding metallurgy*, 2nd ed. Hoboken, N.J: Wiley-Interscience, 2003.
[36] B. E. Carroll *et al.*, "Functionally graded material of 304L stainless steel and inconel 625 fabricated by directed energy deposition: Characterization and thermodynamic modeling," *Acta Materialia*, vol. 108, pp. 46–54, Apr. 2016, doi: 10.1016/j.actamat.2016.02.019.
[37] D. A. Akinlade, W. F. Caley, N. L. Richards, and M. C. Chaturvedi, "Microstructural and thermal processing effects on adding 1 and 3 w/o Ti to a powder metallurgy processed quaternary Ni–Cr–Fe–Al alloy," *Materials Science and Engineering: A*, vol. 528, no. 3, pp. 996–1002, Jan. 2011, doi: 10.1016/j.msea.2010.10.044.
[38] D. A. Akinlade, W. F. Caley, N. L. Richards, and M. C. Chaturvedi, "Microstructural response of an Al-modified Ni–Cr–Fe ternary alloy during thermal processing," *Materials Science and Engineering: A*, vol. 486, no. 1–2, pp. 626–633, Jul. 2008, doi: 10.1016/j.msea.2007.10.076.
[39] Y.-J. Liang, X.-J. Tian, Y.-Y. Zhu, J. Li, and H.-M. Wang, "Compositional variation and microstructural evolution in laser additive manufactured Ti/Ti–6Al–2Zr–1Mo–1V graded structural material," *Materials Science and Engineering: A*, vol. 599, pp. 242–246, Apr. 2014, doi: 10.1016/j.msea.2014.01.092.
[40] M. M. Atabaki, M. Nikodinovski, P. Chenier, J. Ma, M. Harooni, and R. Kovacevic, "Welding of Aluminum Alloys to Steels: An Overview," *Journal for Manufacturing Science and Production*, vol. 14, no. 2, Jan. 2014, doi: 10.1515/jmsp-2014-0007.
[41] Q. Yang, S. Meng, W. Xie, H. Jin, C. Xu, and S. Du, "Effective mitigation of the thermal short and expansion mismatch effects of an integrated thermal protection system through topology optimization," *Composites Part B: Engineering*, vol. 118, pp. 149–157, Jun. 2017, doi: 10.1016/j.compositesb.2017.03.038.
[42] C. Y. Ho and R. E. Taylor, Eds., *Thermal expansion of solids*. Materials Park, OH: ASM International, 1998.
[43] R. S. Krishnan, R. Srinivasan, and S. Devanarayanan, *Thermal expansion of crystals*. Oxford [Eng.] ; New York: Pergamon Press, 1979.
[44] G. Béranger, F. Duffaut, J. Morlet, and J.-F. Tiers, Eds., *The Iron-Nickel Alloys: A Hundred Years after the Discovery of Invar*. Andover: Intercept Ltd., 1996.
[45] S. Trolier-McKinstry and R. E. Newnham, *Materials engineering: bonding, structure, and structure-property relationships*. Cambridge, United Kingdom ; New York, NY, USA: Cambridge University Press, 2017.
[46] G. B. Benedek and F. Villars, *Physics, with illustrative examples from medicine and biology*, 2nd ed. New York: AIP Press, 2000.
[47] S. Tosto, "Reappraising 1907 Einstein's Model of Specific Heat," *OJPC*, vol. 06, no. 04, pp. 109–128, 2016, doi: 10.4236/ojpc.2016.64011.
[48] C. Kittel, *Introduction to solid state physics*, 8th ed. Hoboken, NJ: Wiley, 2005.
[49] R. F. Barron and B. R. Barron, *Design for thermal stresses*. Hoboken, N.J: Wiley, 2012.
[50] S. A. Holgate, *Understanding Solid State Physics*. CRC Press, 2009.

[51] S. Arajs, “Ferromagnetic Curie Temperatures of Iron Solid Solutions with Germanium, Silicon, Molybdenum, and Manganese,” *phys. stat. sol. (b)*, vol. 11, no. 1, pp. 121–126, 1965, doi: 10.1002/pssb.19650110110.
[52] B. D. Cullity, *Elements of x-ray diffraction*, 2d ed. Reading, Mass: Addison-Wesley Pub. Co, 1978.
[53] B. D. Cullity, *Elements of X-ray diffraction*, 3. print. Reading, Mass: Addison-Wesley, 1956.
[54] H. Czichos, T. Saito, and L. Smith, Eds., *Springer handbook of materials measurement methods*. Berlin: Springer, 2006.
[55] R. Sharma and U. Reisgen, “Comparative study of phase transformation temperatures in high strength steel weld metals,” *MP*, vol. 59, no. 4, pp. 344–347, Apr. 2017, doi: 10.3139/120.111003.
[56] “High-Resolution Coefficient of Thermal Expansion | PMIC.” https://pmiclab.com/testing-services/thermal-expansion/ (accessed Jun. 23, 2020).
[57] P. Hariharan, *Basics of interferometry*, 2nd ed. Amsterdam ; Boston: Elsevier Academic Press, 2007.
[58] W. D. Drotning, “Design of a high precision dilatometer using laser interferometry,” SAND-78-1796, 6424043, Dec. 1978. doi: 10.2172/6424043.
[59] J. S. Keist and T. A. Palmer, “Development of strength-hardness relationships in additively manufactured titanium alloys,” *Materials Science and Engineering: A*, vol. 693, pp. 214–224, May 2017, doi: 10.1016/j.msea.2017.03.102.
[60] A. M. Abyzov, S. V. Kidalov, and F. M. Shakhov, “High thermal conductivity composite of diamond particles with tungsten coating in a copper matrix for heat sink application,” *Applied Thermal Engineering*, vol. 48, pp. 72–80, Dec. 2012, doi: 10.1016/j.applthermaleng.2012.04.063.
[61] M.-I. Baraton and I. Uvarova, Eds., *Functional Gradient Materials and Surface Layers Prepared by Fine Particles Technology*. Dordrecht: Springer Netherlands, 2001.
[62] H. A. Bruck and B. H. Rabin, “Evaluation of Rule-of-Mixtures Predictions of Thermal Expansion in Powder-Processed Ni-Al2O3 Composites,” *Journal of the American Ceramic Society*, vol. 82, no. 10, pp. 2927–2930, Dec. 2004, doi: 10.1111/j.1151-2916.1999.tb02182.x.
[63] N. Chawla and K. K. Chawla, *Metal Matrix Composites*, Second. New York, NY: Springer, 2013.
[64] R. Danzer, T. Lube, R. Morrell, and P. Supancic, “Mechanical Properties of Ceramics,” in *Handbook of Advanced Ceramics*, Elsevier, 2013, pp. 609–632.
[65] Y. Miyamoto, W. A. Kaysser, B. H. Rabin, A. Kawasaki, and R. G. Ford, Eds., *Functionally Graded Materials*, vol. 5. Boston, MA: Springer US, 1999.
[66] B. Girish, Basawaraj, B. Satish, and P. Jain, “Tungsten carbide reinforced copper composites for thermal management applications,” *Proceedings of the Institution of Mechanical Engineers, Part L: Journal of Materials: Design and Applications*, vol. 226, no. 4, pp. 316–321, Oct. 2012, doi: 10.1177/1464420712445545.
[67] R. U. Vaidya and K. K. Chawla, “Thermal expansion of metal-matrix composites,” *Composites Science and Technology*, vol. 50, no. 1, pp. 13–22, 1994, doi: https://doi.org/10.1016/0266-3538(94)90122-8.
[68] S. Tompkins and G. Dries, “Thermal Expansion Measurements of Metal Matrix Composites,” in *Testing Technology of Metal Matrix Composites*, N. Adsit and P. DiGiovanni, Eds. 100 Barr Harbor Drive, PO Box C700, West Conshohocken, PA 19428-2959: ASTM International, 1988, pp. 248-248–11.

[69] B. Feng, Y. Xin, Z. Sun, H. Yu, J. Wang, and Q. Liu, “On the rule of mixtures for bimetal composites,” *Materials Science and Engineering: A*, vol. 704, pp. 173–180, Sep. 2017, doi: 10.1016/j.msea.2017.08.005.

[70] S. K. Thakur and M. Gupta, “Use of interconnected reinforcement in magnesium for stiffness critical applications,” *Materials Science and Technology*, vol. 24, no. 2, pp. 213–220, Feb. 2008, doi: 10.1179/174328407X240972.

[71] C. Karch, “Micromechanical Analysis of Thermal Expansion Coefficients,” *Modeling and Numerical Simulation of Material Science*, vol. 04, no. 03, pp. 104–118, 2014, doi: 10.4236/mnsms.2014.43012.

[72] H. A. Bruck and B. H. Rabin, “Evaluation of Rule-of-Mixtures Predictions of Thermal Expansion in Powder-Processed Ni–Al2O3 Composites,” *Journal of the American Ceramic Society*, vol. 82, no. 10, pp. 2927–2930, 1999.

[73] J. V. Elmer, D. L. Olson, and D. K. Matlock, “The Thermal Expansion Characteristics of Stainless Steel Weld Metal,” *Welding Research Supplement*, p. 9, 1982.

[74] J. P. Thomas, “EFFECT OF INORGANIC FILLERS ON COEFFICIENT OF THERMAL EXPANSION OF POLYMERIC MATERIALS,” GENERAL DYNAMICS, FORT WORTH TEXAS, Defense Technical Information Center AD0287826, Dec. 1960.

[75] G. Grimvall, “Bounds on transport, elastic and thermal expansion parameters in eutectic two-phase materials,” *J. Phys. C: Solid State Phys.*, vol. 17, no. 20, pp. 3545–3549, Jul. 1984, doi: 10.1088/0022-3719/17/20/007.

[76] Z. Hashin and S. Shtrikman, “A Variational Approach to the Theory of the Effective Magnetic Permeability of Multiphase Materials,” *Journal of Applied Physics*, vol. 33, no. 10, pp. 3125–3131, Oct. 1962, doi: 10.1063/1.1728579.

[77] K. S. Ravichandran, “Thermal residual stresses in a functionally graded material system,” *Materials Science and Engineering: A*, vol. 201, no. 1, pp. 269–276, 1995, doi: https://doi.org/10.1016/0921-5093(95)09773-2.

[78] T. M. Pollock, D. M. Lipkin, and K. J. Hemker, “Multifunctional coating interlayers for thermal-barrier systems,” *MRS Bulletin*, vol. 37, no. 10, pp. 923–931, Oct. 2012, doi: 10.1557/mrs.2012.238.

[79] F. Cverna and ASM International, Eds., *ASM ready reference. Thermal properties of metals*. Materials Park, Ohio: ASM International, 2002.

[80] Y. S. Touloukian, R. K. Kirby, R. E. Taylor, and P. D. Desai, “Thermophysical Properties of Matter - the TPRC Data Series. Volume 12. Thermal Expansion Metallic Elements and Alloys,” Purdue University, Thermophysical Properties Research Center, Data Book A129115, 1975.

[81] F. H. Froes, Ed., *Titanium: physical metallurgy processing and applications*. Materials Park, Ohio: ASM International, 2015.

[82] E37 Committee, “Test Method for Linear Thermal Expansion of Solid Materials With a Push-Rod Dilatometer,” ASTM International, 2017. doi: 10.1520/E0228-17.

[83] J. S. Keist, S. Nayir, and T. A. Palmer, “Impact of hot isostatic pressing on the mechanical and microstructural properties of additively manufactured Ti–6Al–4V fabricated using directed energy deposition,” *Materials Science and Engineering: A*, vol. 787, p. 139454, Jun. 2020, doi: 10.1016/j.msea.2020.139454.

[84] R. E. Dickerson, H. B. Gray, and G. P. Haight, “Chapter 18: Equilibria Involving Liquids and Solids,” in *Chemical principles*, 3d ed., Menlo Park, Calif: Benjamin/Cummings Pub. Co, 1979.

[85] “The elements of the periodic table sorted by electronegativity.” https://www.lenntech.com/periodic-chart-elements/electronegativity.htm (accessed Jul. 15, 2019).

[86] "Shear Modulus for all the elements in the Periodic Table." https://periodictable.com/Properties/A/ShearModulus.html (accessed Jul. 15, 2019).
[87] J. Andrieux, O. Dezellus, F. Bosselet, and J. C. Viala, "Low-Temperature Interface Reaction Between Titanium and the Eutectic Silver-Copper Brazing Alloy," *Journal of Phase Equilibria and Diffusion*, vol. 30, no. 1, p. 40, Nov. 2008, doi: 10.1007/s11669-008-9424-7.
[88] A. Elrefaey and W. Tillmann, "Interface Characteristics and Mechanical Properties of the Vacuum-Brazed Joint of Titanium-Steel Having a Silver-Based Brazing Alloy," *Metallurgical and Materials Transactions A*, vol. 38, no. 12, pp. 2956–2962, Nov. 2007, doi: 10.1007/s11661-007-9357-5.
[89] A. Laik, A. A. Shirzadi, G. Sharma, R. Tewari, T. Jayakumar, and G. K. Dey, "Microstructure and Interfacial Reactions During Vacuum Brazing of Stainless Steel to Titanium Using Ag-28 pct Cu Alloy," *Metallurgical and Materials Transactions A*, vol. 46, no. 2, pp. 771–782, Feb. 2015, doi: 10.1007/s11661-014-2671-9.
[90] J. Andrieux *et al.*, "Details on the Formation of Ti2Cu3 in the Ag-Cu-Ti System in the Temperature Range 790 to 860 °C," *Journal of Phase Equilibria and Diffusion*, vol. 29, no. 2, pp. 156–162, Apr. 2008, doi: 10.1007/s11669-008-9247-6.
[91] A. Shafiei, P. Abachi, K. Dehghani, and K. Pourazarang, "On the Formation of Intermetallics during the Furnace Brazing of Pure Titanium to 304 Stainless Steel Using Ag (30–50%)–Cu Filler Metals," *Materials and Manufacturing Processes*, vol. 25, no. 11, pp. 1333–1340, Dec. 2010, doi: 10.1080/10426914.2010.523911.
[92] A. H. M. E. Rahman and M. N. Cavalli, "Strength and microstructure of diffusion bonded titanium using silver and copper interlayers," *Materials Science and Engineering: A*, vol. 527, no. 20, pp. 5189–5193, Jul. 2010, doi: 10.1016/j.msea.2010.04.065.
[93] A. H. M. E. Rahman and M. N. Cavalli, "Strength and Fracture Behavior of Diffusion Bonded Joints," in *Experimental and Applied Mechanics, Volume 6*, T. Proulx, Ed. New York, NY: Springer New York, 2011, pp. 677–682.
[94] M. Li, C. Li, F. Wang, and W. Zhang, "Silver-Titanium Binary Phase Diagram," in *ASM Alloy Phase Diagrams Database*, H. Okamoto and K. Cenzual, Eds. Materials Park, OH: ASM International, 2016.
[95] M. A. Turchanin, P. G. Agraval, and A. R. Abdulov, "Copper-Titanium Binary Phase Diagram," in *ASM Alloy Phase Diagrams Database*, H. Okamoto and K. Cenzual, Eds. Materials Park, OH: ASM International, 2016.
[96] O. Taguchi and Y. Iijima, "Diffusion of copper, silver and gold in α-titanium," *Philosophical Magazine A*, vol. 72, no. 6, pp. 1649–1655, Dec. 1995, doi: 10.1080/01418619508243935.
[97] F. C. Nix and D. MacNair, "The Thermal Expansion of Pure Metals: Copper, Gold, Aluminum, Nickel, and Iron," *Phys. Rev.*, vol. 60, no. 8, pp. 597–605, Oct. 1941, doi: 10.1103/PhysRev.60.597.
[98] P. Hidnert, "Thermal expansion of monocrystalline and polycrystalline antimony," *J. RES. NATL. BUR. STAN.*, vol. 14, no. 5, p. 523, May 1935, doi: 10.6028/jres.014.028.
[99] R. R. Pawar and V. T. Deshpande, "The Anisotropy of the Thermal Expansion of a-Titanium," p. 2.
[100] A. M. Russell and B. A. Cook, "Coefficient of thermal expansion anisotropy and texture effects in ultra-thin titanium sheet," *Scripta Materialia*, vol. 37, no. 10, pp. 1461–1467, Nov. 1997, doi: 10.1016/S1359-6462(97)00312-6.
[101] Z. Sun, X. Tan, S. B. Tor, and C. K. Chua, "Simultaneously enhanced strength and ductility for 3D-printed stainless steel 316L by selective laser melting," *NPG Asia Materials*, vol. 10, no. 4, pp. 127–136, Apr. 2018, doi: 10.1038/s41427-018-0018-5.

[102] O. Zinovieva, A. Zinoviev, and V. Ploshikhin, "Three-dimensional modeling of the microstructure evolution during metal additive manufacturing," *Computational Materials Science*, vol. 141, pp. 207–220, Jan. 2018, doi: 10.1016/j.commatsci.2017.09.018.
[103] "MTEX Toolbox | MTEX." https://mtex-toolbox.github.io/index.html (accessed Jun. 14, 2020).
[104] F. Bachmann, R. Hielscher, and H. Schaeben, "Texture Analysis with MTEX – Free and Open Source Software Toolbox," *SSP*, vol. 160, pp. 63–68, Feb. 2010, doi: 10.4028/www.scientific.net/SSP.160.63.
[105] D. Mainprice, R. Hielscher, and H. Schaeben, "Calculating anisotropic physical properties from texture data using the MTEX open-source package," *Geological Society, London, Special Publications*, vol. 360, no. 1, pp. 175–192, 2011, doi: 10.1144/SP360.10.
[106] "Tensor Averages | MTEX." https://mtex-toolbox.github.io/TensorAverage.html (accessed Jun. 14, 2020).
[107] D. Mainprice, F. Bachmann, R. Hielscher, H. Schaeben, and G. E. Lloyd, "Calculating anisotropic piezoelectric properties from texture data using the MTEX open source package," *Geological Society, London, Special Publications*, vol. 409, no. 1, pp. 223–249, 2015, doi: 10.1144/SP409.2.
[108] J. Spreadborough and J. W. Christian, "The Measurement of the Lattice Expansions and Debye Temperatures of Titanium and Silver by X-ray Methods," *Proc. Phys. Soc.*, vol. 74, no. 5, pp. 609–615, Nov. 1959, doi: 10.1088/0370-1328/74/5/314.
[109] T. J. B. Holland and S. A. T. Redfern, "Unit cell refinement from powder diffraction data; the use of regression diagnostics," *Mineralogical Magazine*, vol. 61, no. 1, pp. 65–77, 1997.
[110] M. Niinomi, "Metallic biomaterials," *J Artif Organs*, vol. 11, no. 3, pp. 105–110, Sep. 2008, doi: 10.1007/s10047-008-0422-7.
[111] L. Goncharova, "Chapter 3: The Structure of Crystalline Solids," presented at the Physics 2800: Intorduction to Materials Science Part 1, The Department of Physics and Astronomy, The University of Western Ontario, Canada, 2008, [Online]. Available: http://www.physics.uwo.ca/~lgonchar/courses/p2800/Chapter3_Crystal_Handouts.pdf.
[112] K. Persson, "Materials Data on Ti2Cu (SG:139) by Materials Project." LBNL Materials Project; Lawrence Berkeley National Laboratory (LBNL), Berkeley, CA (United States), 2016, doi: 10.17188/1287957.
[113] D. Raabe, *Computational materials science: the simulation of materials microstructures and properties*. Weinheim ; New York: Wiley-VCH, 1998.
[114] W. Kohn and L. J. Sham, "Self-Consistent Equations Including Exchange and Correlation Effects," *Phys. Rev.*, vol. 140, no. 4A, pp. A1133–A1138, Nov. 1965, doi: 10.1103/PhysRev.140.A1133.
[115] S. Baroni, P. Giannozzi, and A. Testa, "Green's-function approach to linear response in solids," *Phys. Rev. Lett.*, vol. 58, no. 18, pp. 1861–1864, May 1987, doi: 10.1103/PhysRevLett.58.1861.
[116] G. Liu, J. Zhou, and H. Wang, "Anisotropic thermal expansion of SnSe from first-principles calculations based on Grüneisen's theory," *Phys. Chem. Chem. Phys.*, vol. 19, no. 23, pp. 15187–15193, 2017, doi: 10.1039/C7CP00815E.
[117] N. A. Pike and O. M. Løvvik, "Calculation of the anisotropic coefficients of thermal expansion: A first-principles approach," *Computational Materials Science*, vol. 167, pp. 257–263, Sep. 2019, doi: 10.1016/j.commatsci.2019.05.045.
[118] C. Wei, D. Srivastava, and K. Cho, "Thermal Expansion and Diffusion Coefficients of Carbon Nanotube-Polymer Composites," *Nano Lett.*, vol. 2, no. 6, p. 4, 2002.
[119] M. G. Jurado-Taracena, "On brillouin zones and related constructions," p. 6, 2011.

[120] R. E. Reed-Hill and R. Abbaschian, *Physical metallurgy principles*, 3rd ed. Boston: PWS-Kent Pub, 1992.
[121] E. Grüneisen, "Zustand des festen Körpers," in *Thermische Eigenschaften der Stoffe*, C. Drucker, E. Grüneisen, Ph. Kohnstamm, F. Körber, K. Scheel, E. Schrödinger, F. Simon, J. D. van der Waals, and F. Henning, Eds. Berlin, Heidelberg: Springer Berlin Heidelberg, 1926, pp. 1–59.
[122] T. H. K. Barron, J. G. Collins, and G. K. White, "Thermal expansion of solids at low temperatures," *Advances in Physics*, vol. 29, no. 4, pp. 609–730, Aug. 1980, doi: 10.1080/00018738000101426.
[123] P. K. Schelling and P. Keblinski, "Thermal expansion of carbon structures," *Phys. Rev. B*, vol. 68, no. 3, p. 035425, Jul. 2003, doi: 10.1103/PhysRevB.68.035425.
[124] P. Giannozzi *et al.*, "QUANTUM ESPRESSO: a modular and open-source software project for quantum simulations of materials," *J. Phys.: Condens. Matter*, vol. 21, no. 39, p. 395502, Sep. 2009, doi: 10.1088/0953-8984/21/39/395502.
[125] J. P. Perdew, K. Burke, and M. Ernzerhof, "Generalized Gradient Approximation Made Simple," *Phys. Rev. Lett.*, vol. 77, no. 18, pp. 3865–3868, Oct. 1996, doi: 10.1103/PhysRevLett.77.3865.
[126] H. J. Monkhorst and J. D. Pack, "Special points for Brillouin-zone integrations," *Phys. Rev. B*, vol. 13, no. 12, pp. 5188–5192, Jun. 1976, doi: 10.1103/PhysRevB.13.5188.
[127] A. Togo and I. Tanaka, "First principles phonon calculations in materials science," *Scripta Materialia*, vol. 108, pp. 1–5, Nov. 2015, doi: 10.1016/j.scriptamat.2015.07.021.

Appendix A

MTEX CODE

The first step is to import the EBSD Map in to MTEX (which is a MATLAB plugin). This is done using the MTEX EBSD import wizard using the .ctf file obtained from EBSD scanning software. The wizard generates a code used to import the data and an example is given below for a $CuTi_2$ sample:

```
%% Import Script for EBSD Data
%
% This script was automatically created by the import wizard. You should
% run the whoole script or parts of it in order to import your data. There
% is no problem in making any changes to this script.

%% Specify Crystal and Specimen Symmetries

% crystal symmetry
CS = {...
  'notIndexed',...
  crystalSymmetry('4/mmm', [3 3 11], 'mineral', 'CuTi2 - Card', 'color', [0.53 0.81
0.98]),...
  crystalSymmetry('6/mmm', [3 3 4.7], 'X||a*', 'Y||b', 'Z||c*', 'mineral', 'Ti-Hex',
'color', [0.56 0.74 0.56]),...
  crystalSymmetry('4/mmm', [3.1 3.1 5.9], 'mineral', 'CuTi - Card', 'color', [0.85 0.65
0.13])};

% plotting convention
setMTEXpref('xAxisDirection','east');
setMTEXpref('zAxisDirection','outOfPlane');

%% Specify File Names

% path to files
pname = 'C:\........[insert your path here]';

% which files to be imported
fname = [pname '\DATA.ctf'];

%% Import the Data

% create an EBSD variable containing the data
ebsd = EBSD.load(fname,CS,'interface','crc',...
  'convertEuler2SpatialReferenceFrame');
```

Now that the EBSD orientation data is loaded a separate code that was developed in this effort was run to calculate the average material tensor, which in this case is the average corrected CTE tensor (selected the Hill average). An example for commercially pure titanium is given here:

```
odfTi = calcDensity(ebsd('Ti-Hex').orientations,'halfwidth',10*degree)
TiMatrix = [9.55,0,0;0,9.55,0;0,0,10.65]
TiSymmetry = crystalSymmetry('6/mmm','mineral','Ti-Hex')
CTE_Ti = tensor(TiMatrix,TiSymmetry)
Corrected_CTE_Hill = calcTensor(odfTi,CTE_Ti,'Hill')
```

The **Corrected_CTE_Hill** tensor will be a 3x3 matrix and an example for commercially pure titanium is given here:

$$\begin{bmatrix} 9.678 & -0.027 & -0.012 \\ -0.027 & 10.033 & 0.001 \\ -0.012 & 0.001 & 10.004 \end{bmatrix}$$

where the first position, x_{11} is the x contribution to the CTE in the x direction, while the value below it, x_{21} is the y contribution to the x direction, and the final value in the column, x_{31}, is the z contribution to the x direction. The other columns follow the same logic for y and z respectively. In order to determine the x direction expansion, a sum of the column is performed, since the texture is having an effect in three dimensions. Therefore, in this case, the x-direction CTE is 9.639 ppm/^{o}C which would correlate to the vertical orientation in the sample.

Appendix B

DFT THEORY AND COMPUTATIONAL DETAILS[2]

This appendix serves to provide additional details to the DFT simulations presented in the text, the thermal expansion coefficients of intermetallic compounds are calculated from first-principles simulations, using Grüneisen's theory [116], [121]–[123]. By definition, the thermal expansion coefficient is a second-rank tensor as discussed in Chapter 2, and the formula has been rewritten with new subscripts here:

$$\alpha_{ab} = \left(\frac{\partial \varepsilon_{ab}}{\partial T}\right)_{\sigma}$$

where $\boldsymbol{\varepsilon}$ is the strain tensor, and T is the temperature. Thermal expansion coefficient $\boldsymbol{\alpha}$ describes the change in dimensions of a materials as a function of changing temperature. Additionally, the generalized Hook's law dictates that

$$\sigma_{de} = \sum_{ab} C_{deab}\, \varepsilon_{ab}$$

$$\varepsilon_{ab} = \sum_{de} S_{deab}\, \sigma_{ab}$$

where $\boldsymbol{C}$ and $\boldsymbol{S}$ are elastic stiffness and compliance tensors, respectively. Building on these useful relations, the thermal expansion coefficients can be decomposed into two parts

$$\alpha_{ab} = -\sum_{de} \left(\frac{\partial \varepsilon_{ab}}{\partial \sigma_{de}}\right)_{T} \times \left(\frac{\partial \sigma_{de}}{\partial T}\right)_{\varepsilon}$$

[2] This appendix was adapted from the same working paper previously noted 'Tailoring the CTE of Additively Manufactured Titanium' authored by S.R. Hilburn and W. Chen

Assuming quasi-harmonic approximation, the energy of the system as a function of strain ε can be written as

$$F(\varepsilon,T) = E(\varepsilon) + (1/N)\sum_{\boldsymbol{q},j}\left\{\left(\frac{\hbar\omega_{\boldsymbol{q},j}(\varepsilon)}{2}\right) + k_B T \ln\left[1 - e^{\left(-\frac{\hbar\omega_{\boldsymbol{q},j}(\varepsilon)}{k_B T}\right)}\right]\right\}$$

where $\hbar$ is the Planck's constant, k_B is the Boltzmann's constant, and $\omega_{\boldsymbol{q},j}$ represents a phonon mode with wavevector $\boldsymbol{q}$ and polarization j. Making use of the fact that $\sigma_{de} = \frac{1}{V_0}\frac{\partial F}{\varepsilon_{ab}}$, the strain tensor can be rewritten as

$$\sigma_{de} = \frac{1}{V_0}\left[\frac{\partial E}{\partial \varepsilon_{de}} - (1/N)\sum_{\boldsymbol{q},j}\gamma^{de}_{\boldsymbol{q},j}\ \hbar\omega_{\boldsymbol{q},j}\left(n_{\boldsymbol{q},j} + \frac{1}{2}\right)\right]$$

where $n_{\boldsymbol{q},j}$ is the equilibrium occupation of phonons, and $\gamma^{de}_{\boldsymbol{q},j}$ is the Gruneisen parameter, which describes the change in phonon frequency induced by a dimensional change

$$\gamma^{de}_{\boldsymbol{qj}} = -\frac{1}{\omega_{\boldsymbol{qj}}}\frac{\partial\omega_{\boldsymbol{qj}}}{\partial\varepsilon_{de}}$$

A macroscopic Gruneisen parameter is often defined to take into account of the temperature dependence

$$G_{de}(T) = \frac{\sum_{\boldsymbol{qj}} C_{\boldsymbol{qj}}\gamma^{de}_{\boldsymbol{qj}}}{\sum_{\boldsymbol{qj}} C_{\boldsymbol{qj}}}$$

Therefore, the second part in Eqn.X becomes

$$\left(\frac{\partial\sigma_{de}}{\partial T}\right)_{\varepsilon} = -\frac{1}{V_0 N}\sum_{\boldsymbol{q},j}\gamma^{de}_{\boldsymbol{qj}}\ C_{\boldsymbol{q},j}$$

Finally, one can write the thermal expansion coefficients as

$$\alpha_l = \frac{1}{V_0 N}\sum_{k} S_{lk}\sum_{\boldsymbol{qj}} C_{\boldsymbol{q}\lambda}\,\gamma^{k}_{\boldsymbol{qj}} = \frac{C_V}{V_0}\sum_{k} S_{lk}\ G_k$$

Where l and k are indexed through three space dimensions.

Computational details

The calculation of thermal expansion coefficients necessitates the computation of vibrational properties, such as the Gruneisen's parameter, phonon dispersion relations, of the intermetallic compound of interest. The harmonic force constants are calculated perturbatively using the PHonon package of the QUANTUM ESPRESSO software. [124] Calculations are done using the Perdew-Burke-Ernzehof approximation, with a kinetic energy cutoff of 60 and 600 Ry. [125] For $CuTi_2$, its Brillouin zone is sampled with 15 × 15 × 9 Monkhorst-Pack grid, and for CuTi, its Brillouin zone is sampled with a 17 × 17 × 9 Monkhorst-Pack grid. [126] The harmonic force constants are calculated on a 3 × 3 × 3 and 5 × 5 × 5 q-point mesh for $CuTi_2$ and CuTi compounds, respectively. The calculation of Gruneisen parameters are done using the PHONOPY package. [127] Taking into consideration of the point group symmetry of the unit cells, for both $CuTi_2$ and CuTi compounds there are two independent linear thermal expansion coefficients: α_a and α_c along a-directions and c-direction of the crystals, respectively.

VITA

Skyler R. Hilburn

EDUCATION

Doctor of Philosophy, Materials Science and Engineering,
The Pennsylvania State University 2020

Master of Science, Materials Science and Engineering,
Air Force Institute of Technology 2014

Bachelor of Science, Chemical and Biomolecular Engineering,
The Georgia Institute of Technology 2009

PUBLICATIONS

B. Perez, **S. Hilburn**, D. Jensen, and K. L. Wood, "Design principle-based stimuli for improving creativity during ideation," Proceedings of the Institution of Mechanical Engineers, Part C: Journal of Mechanical Engineering Science, vol. 233, no. 2, pp. 493–503, Jan. 2019, doi: 10.1177/0954406218809117.

M. Ruggles-Wrenn and **S. Hilburn**, "Creep in Interlaminar Shear of a Nextel TM 720/aluminosilicate Composite at 1100°C in Air and in Steam," Int. J. Appl. Ceram. Technol., vol. 12, no. 2, pp. 473–480, Mar. 2015, doi: 10.1111/ijac.12357.